Phase Contrast Imaging: A Turbulence Diagnostic for the Wendelstein 7-X Stellarator

Thesis submitted for the degree of
Doctor of Philosophy

Department of Physics
Technical University of Denmark

Technical University of Denmark

Lukas-Georg Böttger

Phase Contrast Imaging: A Turbulence Diagnostic for the Wendelstein 7-X Stellarator

Supervisor: Prof. Volker Naulin

Co-supervisors: Prof. Olaf Grulke

Technical University of Denmark

Submitted to the Technical University of Denmark
on 14.03.2019.

Abstract

Classical stellarators suffer from strong neoclassical transport. The advanced stellarator Wendelstein 7-X is the first fully neo-classically optimized device posing the question about the role of turbulence in optimized stellarators. While there has been a growing number of theoretical investigations about turbulence in advanced stellarator geometry over the last two decades, the experimental investigation is a completely new field. The present thesis deals with the phase contrast imaging (PCI) diagnostic implementation on Wendelstein 7-X as a tool to address the lack of experimental research on the evolution of turbulent fluctuations in optimized stellarator geometry. Numerical simulations suggest the occurrence of microturbulence in the spatiotemporal range of ion scales such as the ITG and TEM instabilities. The PCI diagnostic allows for non-invasive measurements of line-of-sight integrated density fluctuations. It incorporates a flexible design to cover spatiotemporal scales from the ion down to the electron scale. The PCI uses a CO_2 laser emitting light at 10.6 μm. At this wavelength the plasma acts as an optical isotropic medium in which density fluctuations present phase objects causing a scattering of the laser. Key element of the PCI diagnostic is the phase plate which allows for a phase shift of the most energetic scattered light components in order to convert the phase modulation into a measurable intensity variation. An excellent alignment onto the phase plate is crucial for the linear diagnostic response on the density fluctuations. An optical beam path length of more than 20 m imposes a challenge on this alignment. As a consequence, remote control capabilities are implemented in order to control and correct any misalignment during operation. Turbulent density fluctuations in the ion scale are analysed on the example of a typical electron cyclotron resonance heated discharge in Wendelstein 7-X for a moderate density and different heating steps. The spectral analysis reveals broadband fluctuations and a spectrum showing typical turbulent properties such as indications for self-similar fluctuations resulting in a power law scaling of energy. The dominant wave number of $k\rho_s \approx 0.3$ lies in the expected range of ion scale turbulence. A constant phase velocity is observed, which indicates a strong Doppler shift due to the plasma $E{\times}B$-rotation. Indeed, measurements of the plasma $E{\times}B$-rotation are in general agreement with the observed phase velocities for both heating steps. In the context of ITG and TEM as paradigmatic instabilities in the ion scale diamagnetic drift velocities are expected to contribute to the

fluctuation propagation. The measurement results are indicative that the observed fluctuation behaviour is predominantly governed by TEM driven turbulence. This interpretation is supported by the observed reduction of turbulence with reduced heating power, which correlates with a reduction of the radial gradient of electron temperature while the density gradient stays almost unchanged.

Keywords: phase contrast imaging, plasma turbulence, stellarator

Resumé

Klassiske stellaratorer er domineret af stærk neoklassisk transport. Den avancerede stellarator Wendelstein 7-X er den første fuldt neoklassisk optimerede maskine, hvori der undersøges turbulens i en optimeret geometri. Mens der de seneste årtier har været et stigende antal teoretiske undersøgelser af turbulens i stellaratorer med avanceret geometri, er dette uudforsket territorium for eksperimentelle undersøgelser. I denne afhandling fremlægges implementeringen af den såkaldte 'phase contrast imaging' (PCI) diagnostik på Wendelstein 7-X som et redskab til at udfylde det tomrum som udgøres af manglen på eksperimentelle undersøgelser af udviklingen af mikroturbulens på ion tids- og længdeskalaer såsom ITG og TEM instabiliteter. PCI diagnostik giver ikke-invasive målinger af line-of-sight integrerede tæthedsfluktuationer. Designet er fleksibelt og tillader undersøgelser på ion, og ned til elektron, tids- og længdeskaler. PCI bruger en CO_2-laser, som udsender lys ved 10.6 μm. Ved denne bølgelængde agerer plasmaet som et optisk isotropt medium i hvilket tæthedsfluktuationer virker som faseobjekter og forårsager en spredning af laserlyset. Et nøgleelement i PCI-diagnostikken er fasepladen, som faseforskyder de mest energirige spredte lyskomponenter, så fasemodulationen kan konverteres til en målbar intensitetsvariation. Det er afgørende at fasepladen er justeret nøjagtigt for at få en lineær diagnostisk respons på tæthedsfluktuationerne. Med en optisk strålevejlængde på mere end 20 m er dette en udfordring. Som resultat heraf er der implementeret mulighed for fjernkontrol, så eventuelle fejljusteringer kan rettes under drift. Turbulente tæthedsfluktuationer på ionskala er analyseret for et typisk elektron cyklotron resonans opvarmet plasma i Wendelstein 7-X med en moderat plasmatæthed og forskellige opvarmningstrin. En spektralanalyse viser et bredbåndet fluktuationsspektrum med typiske turbulente karakteristika såsom indikationer på selvsimilære fluktuationer, som giver en power law skalering for energien. Det dominerende bølgetal på $k\rho_s \approx 0.3$ ligger i det forventede interval for ion-skala turbulens. Der er observeret en konstant fasehastighed, hvilket indikerer en stærk Dopplerforskydning grundet plasmaets $E \times B$-rotation. Målinger af plasmaets $E \times B$-rotation stemmer typisk også overens med de observerede fasehastigheder for begge opvarmningstrin. Med ITG og TEM som paradigmatiske ion-skala instabiliteter forventes den diamagnetiske drift at bidrage til propagationen af fluktuationer. Måleresultaterne indikerer at de observerede fluktuationer primært er reguleret af TEM-dreven turbulens.

Denne fortolkning støttes af den observerede turbulensreduktion ved lavere opvarmningseffekt, som korrelerer med en reduktion af den radiale elektron temperaturgradient, mens tæthedsgradienten forbliver uændret.

Preface

The research presented in this thesis was conducted at the Max-Planck Institute for Plasma Physics (IPP) in Greifswald, Germany and the Plasma Physics and Fusion Energy group in the physics department of the Technical University of Denmark (DTU), Kgs. Lyngby, Denmark. This work has been carried out within the framework of the EUROfusion Consortium and has received funding from the Euratom research and training programme 2014-2018 and 2019-2020 under grant agreement No 633053. The views and opinions expressed herein do not necessarily reflect those of the European Commission. The phase contrast imaging diagnostic used in this work was build in close collaboration with the Plasma Science and Fusion Center at the Massachusetts Institute of Technology (MIT) in Cambridge, Massachussets, USA and has received funding from the U.S. department of energy under grant number DE-SC0014229.

The thesis was supervised by Prof. Volker Naulin and Prof. Olaf Grulke. I would like to express my gratitude to my supervisors for the guidance and support I have received over the last years. This work would not have been possible without the incredible valuable work of and the many fruitful discussions within the PCI group consisting of Olaf Grulke, Eric Edlund, Adrian von Stechow and Zhouji Huang. I would like to thank Miklos Porkolab for making this project possible on the U.S. side and Alexander Simon Thrysøe for aiding with the Danish translation of the abstract.

Contents

Chapter 1

Introduction

1.1 Magnetic Confinement Fusion

Thermonuclear fusion of light nuclei provides roughly ten million times more energy per mass unit than fossil energy sources like coal, oil, gas etc. which makes it very attractive as a primary energy source. The basic physical reason for this difference is the nature of the reaction: chemical processes like burning fossil fuels, take place in the outer electron shell of atoms in which typical binding energies are in the order of a few electron volts. In contrast to this, fusion is a nuclear process invoking the strong nuclear force between nuclei. Typical energies are in the order of a few *mega* electron volts, hence six to seven orders of magnitude above those of chemical reactions. The most promising nuclear fusion reaction for a thermo nucelar fusion power plant on earth is the fusion of deuterium an tritium into a helium atom and one neutron [1]

$$\mathrm{D} + \mathrm{T} \rightarrow {}^4\mathrm{He}\,(3.5\,\mathrm{MeV}) + \mathrm{n}\,(14.1\,\mathrm{MeV}). \tag{1.1}$$

However, a gas of deuterium and tritium has to be sufficiently hot – it becomes a plasma – in order to overcome the repelling coulomb barrier. In magnetic confinement fusion this hot plasma is confined by a magnetic field. From (1.1) we see that only 20% of the total energy, which is carried by the helium atom, can be used to heat the plasma. The remaining energy from the neutron leaves the confinement volume since it is not affected by the magnetic field. A plasma has therefore to be sufficiently hot, dense (enough

reactions have to take place) and well confined in order to yield a positive energy balance. This limit is quantified by the fusion triple product [1]

$$nT\tau_{\mathrm{E}} \geq 3 \times 10^{21}\,\mathrm{keVsm}^{-3}\,, \tag{1.2}$$

where n is the plasma density, T the plasma temperature and τ_{E} the energy confinement time – a measure for the energy confinement quality. It becomes clear, that a good confinement, and therefore the transport of energy and particles, plays a crucial role for the feasibility of thermo nuclear fusion on earth. Two major concepts exist for magnetically confined plasmas: the

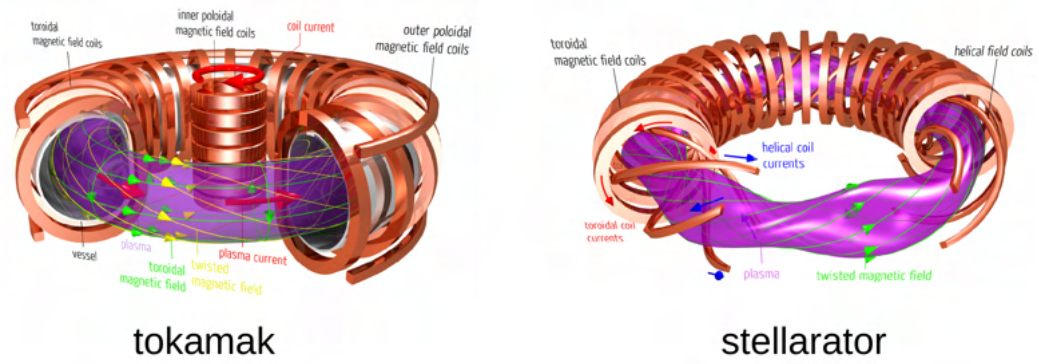

Figure 1.1: Principal sketch of the major magnetic confinement concepts: tokamak (left) and stellarator (right).

tokamak and the stellarator concept (cf. Fig. 1.1). In the tokamak, toroidal magnetic field coils create a strong (a few Tesla) toroidal magnetic field. A central solenoid induces a strong toroidal current (MA range) in the plasma which creates a poloidal magnetic field superimposed on the toroidal field. The resulting twist of the magnetic field lines is necessary for a good confinement [1]. In contrast to a tokamak, the stellarator creates the necessary magnetic field entirely by external coils and is therefore independent of the plasma itself [2]. One major drawback of the tokamak concept is the necessity for the inductive toroidal current drive, thus leading to an intrinsically pulsed operation. Furthermore, the strong current presents a source of free energy for plasma instabilities, exacerbating plasma control. In contrast, a stellarator is intrinsically capable of steady state operation without the need of any net plasma currents. However, the three dimensional geometry and required precision of the stellarator magnetic field complicates the theoretical treatment and technical design. Thus, although both concepts were developed in the 1950s, the tokamak by Tamm and Sacharov in the ex-Soviet Union and the stellarator by Spitzer in the USA, nowadays the leading concept is the

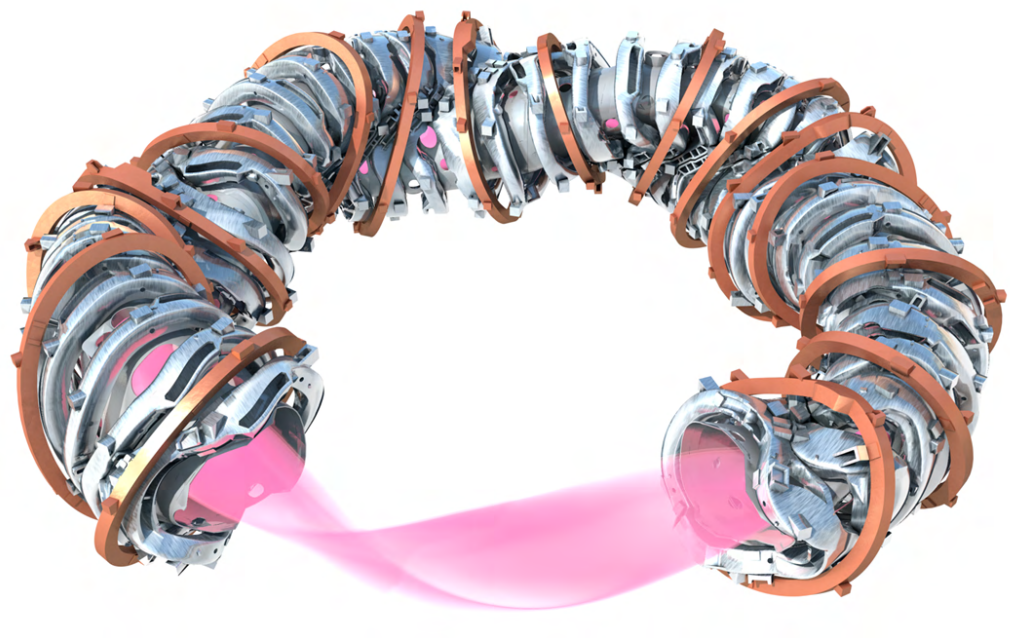

Figure 1.2: Sketch of the Wendelstein 7-X Stellarator. Visible is the plasma, the plasma vessel and the different superconducting magnetic field coils: in silver the 50 non-planar and in copper color the 20 planar coils.

tokamak. The International Thermonuclear Experimental Reactor (ITER) – a tokamak – is the first fusion device aiming to produce net fusion power and is currently under construction in Cadarache, France [3, 4]. However, as computing power increased stellarators could be optimized leading to the advanced stellarators Wendelstein 7-AS (1988 to 2002) [5] and its successor Wendelstein 7-X.

1.2 The Wendelstein 7-X Stellarator

Wendelstein 7-X, the world's biggest and most advanced stellarator, is operated by the Max-Planck Institute for Plasma Physics (IPP) in Greifswald, Germany. Figure 1.2 shows a sketch of the device. Table 1.1 summarizes important physics and engineering parameters. Wendelstein 7-X is optimized with respect to a small bootstrap current, the existence of magnetic surfaces, an magneto-hydrodynamically (MHD) stable plasma, a small shafranov shift,

a good α-particle confinement and technically feasible coils. Wendelstein 7-X was first operated in December 2015 and it turned out, that the relative magnetic field error is less than 10^{-5} – an unprecedented accuracy for a fusion device [6]. The main coil system of Wendelstein 7-X consists of 70 super conducting magnetic field coils, whose Nb-Ti superconductor is cooled by liquid helium down to 3.4 K [7]. The magnetic field has a five fold symmetry. Five different non-planar and two different planar coils create the magnetic field. By varying the coil currents different magnetic field configurations can be realized allowing to change physics relevant parameter such as the inverse safety factor $\iota = 1/q$, the mirror ratio and the absolute magnetic field strength. In addition ten control and five trim coils (both are normal conducting) can impose localized perturbations.

Main heating system is the electron cyclotron resonance heating (ECRH) with a power of up to 7.5 MW provided by ten gyrotrons. As second heating scheme, 3.5 MW heating power from neutral beam injection are available.

Parameter	Range or Value
Plasma volume	30 m^3
Magnetic induction on axis	2.5 T to 3 T
Magnetic field energy	600 MJ
Field periodicity	5
Rotational transform	5/6 to 5/4
ECRH heating power	10 MW (1800 s)
NBI heating power	10 MW (10 s)
ICRH heating power	5 MW (10 s)
Pulse length	1800 s (at 10 MW)
Major radius	5.5 m
Minor radius	0.53 m
Number of non-planar coils	50
Number of planar coils	20
Number of ports	254 of 120 types
Machine height	4.5 m
Outer diameter	16 m
Total mass	750 t
Total cold mass	425 t

Table 1.1: Physics and engineering parameters of the Wendelstein 7-X stellarator [7]. The values for the plasma heating power refer to the second operation phase.

1.3 Thesis Motivation and Outline

Particle and energy transport in magnetic confinement fusion devices can be categorized into three groups: the *classical transport* describes transport only through binary particle collisions. The *neoclassical transport* takes additional drift effects due to magnetic field inhomogeneities into account. The third group, the *turbulent transport* considers transport effects originating from plasma turbulence. Particle and energy transport in modern tokamaks is mostly limited by turbulent transport effects. This is in contrast to classical stellarators which suffer from strong neoclassical transport losses. The discrete coil structure of a stellarator imprints a ripple on the magnetic field, which has severe consequences on the particle confinement in a classical stellarator. Particles, subject to a magnetic drift, can be trapped in these inhomogeneous magnetic field regions and drift outwards leaving the confinement region. This strong neoclassical transport gave rise to stellarator optimization, leading to advanced stellarators such as Wendelstein 7-X. As the neoclassical contribution is expected to be reduced, the role of turbulent transport becomes more important. Since Wendelstein 7-X is the first fully neoclassically optimized stellarator it also presents the first opportunity to experimentally study the role of turbulence in the regulation of radial power and particle losses. The phase contrast imaging diagnostic on Wendelstein 7-X, key part of the present thesis, presents for this purpose a valuable tool, as it is the only fluctuation diagnostic on Wendelstein 7-X which non-invasively measures plasma density fluctuations in the spatiotemporal scales of ion to electron scale in the hot core as well as in the plasma edge.

The present thesis is divided into six parts. Chapter 2, presents a short introduction into important concepts of turbulence, transport mechanisms and instabilities in plasmas as well as an overview about the status of theoretical turbulence investigations in Wendelstein 7-X. Chapter 3 discusses the mechanism of the phase contrast imaging diagnostic, its implementation on Wendelstein 7-X is presented in the following Chapter 4. Chapter 5 discusses turbulence in Wendelstein 7-X on the example of a wave heated plasma. The thesis is finally summarized in Chapter 6.

Chapter 2

Turbulence and Turbulent Transport

The phenomenon of turbulence occurs in many fields of physics – in neutral fluids as well as in plasmas. For example, in figure 2.1 the plume of a candle transits from a well structured, so called laminar flow regime, into a swirled, seemingly irregular regime – the turbulent regime. Turbulence has presented and still presents a research challenge or to quote Richard Feynman:

> "there is a physical problem that is common to many fields, that is very old, and that has not been solved. It is not the problem of finding new fundamental particles, but something left over from a long time ago—over a hundred years. Nobody in physics has really been able to analyze it mathematically satisfactorily in spite of its importance to the sister sciences. It is the analysis of circulating or turbulent fluids."
> – Richard P. Feynman, The Feynman Lectures on Physics Vol 1.

In magnetic confinement fusion it is generally believed that turbulence plays an important role in the transport of energy and particles. Especially, turbulence in tokamaks has been extensively studied over the last decades and it would be way beyond the scope of this thesis to discuss all findings in detail. Instead, this chapter aims for developing a basic understanding of the most relevant concepts and mechanisms. For a more detailed review the interested reader is referred to the given references in the respective sections.

Figure 2.1: The rising plume of a candle in still air. Being initially laminar, the flow develops in a very short transition phase into turbulence in the upper part of the image [8].

2.1 Turbulence in Neutral Fluids

2.1.1 The Reynolds Number

In 1880 Reynolds investigated experientially the transition from laminar to turbulent flows by observing the motion of coloured water flowing through a tube (cf. figure 2.2) [9]. It turned out that the distinction between laminar and turbulent flow regime can be done by the dimensionless Reynolds number

$$R = \frac{LU}{\nu} \tag{2.1}$$

where L and U are the characteristic length and velocity of the flow field, respectively and ν is the kinematic viscosity [9]. If the Reynolds number exceeds a specific threshold $R > R_c$, the flow becomes turbulent. From the definition (2.1) it becomes clear that an increased viscosity stabilizes the flow, whereas an increased velocity destabilizes up to the turbulent regime. To gain a meaningful interpretation of the Reynolds number we consider the

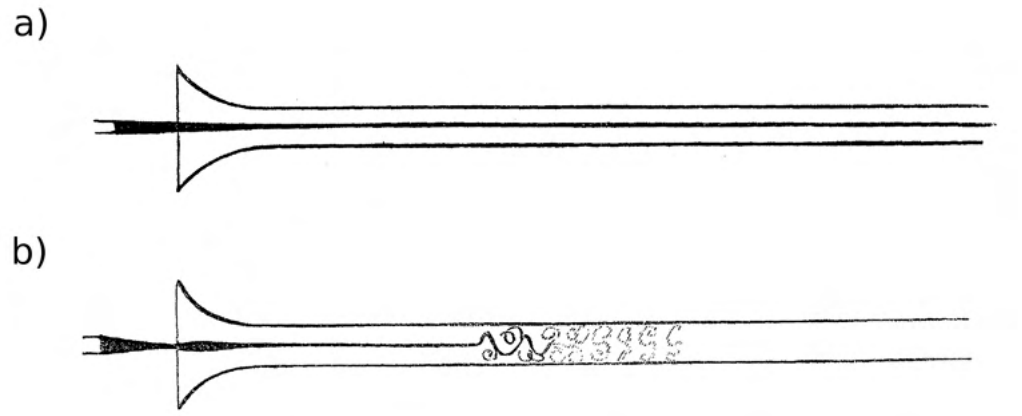

Figure 2.2: Sketch of Reynolds experimental set up for the investigation of the laminar–turbulent flow transition: coloured water is observed while it is flowing through a tube. For sufficiently small Reynolds numbers the flow is laminar (a) whereas it becomes turbulent if the Reynolds number exceeds a critical value (b). Sketches were taken from [9].

Navier-Stokes momentum equation [10]

$$\frac{\partial \vec{u}}{\partial t} + (\vec{u} \cdot \nabla)\, \vec{u} = -\frac{\nabla p}{\rho} + \nu \Delta \vec{u} \tag{2.2}$$

which describes the dynamics of turbulence in an incompressible fluid, where

$$\nabla \cdot \vec{u} = 0\,. \tag{2.3}$$

Here, $\vec{u}(\vec{r}, t)$ is the velocity field, $p(\vec{r}, t)$ the pressure and ρ the mass density. Expanding (2.1) with UL the Reynolds number can be understood as the ratio between the non-linear term and the dissipative term of the Navier-Stokes momentum equation (2.2). With this in mind, an increase of R results in a more dominant role of the non-linear term. An important consequence of this non-linearity is the observed (in principal deterministic) chaotic behaviour and the extreme sensitivity on the initial and boundary conditions. In general fully developed turbulence shows often the following signatures [11]:

- irregularity: the motion of turbulent flows appears to be chaotic, unpredictable and very sensitive to the initial and boundary conditions demanding a statistical description.

- diffusivity: turbulence leads to transport of energy and particles. An example for the turbulence induced transport is the mixing of milk and coffee by stirring. This process is much more efficient than diffusion (as it would be the case without steering).
- rotationality: turbulent flows show often eddies, whirl like structures described by the so-called vorticity.
- dissipation: kinetic energy supplied to the system is dissipated i.e. converted to heat. As a consequence, a permanent energy source is required to drive turbulence.
- scale independence or self similarity: the spatial extent covered by turbulent motion can span several orders of magnitude whereby the characteristic structure of the motion is similar for each length scale. For example, in a hurricane the largest eddy can be on a scale of kilometres whereas the smallest one can be less than a millimetre.

The scale coupling character of turbulence exacerbates extremely the numerical investigation, since the smallest scale defines the step width on the one hand while on the other hand the largest scale sets the global simulation limits.

2.1.2 Energy and Enstrophy in Three Dimensions

A fundamental question in physics is about the role of energy in a system. In the context of turbulence one may ask the question about the energy distribution among the different scales and the energy exchange between them. As mentioned in the previous section, eddies play a fundamental role in turbulent fluids since they define the characteristic structure and hence different scales. In the following section we want to discuss the energy conservation. We follow the derivation in [12], but similar discussions can be also found in e.g. [13, 14]. Mathematical we can measure the rotational character with the vorticity

$$\vec{\Omega} = \nabla \times \vec{u}\,. \tag{2.4}$$

We express the non-linear term in equation (2.2) in terms of the vorticity by using the identity $\nabla(\vec{a}\cdot\vec{b}) = (\vec{a}\cdot\nabla)\vec{b} + (\vec{b}\cdot\nabla)\vec{a} + \vec{a}\times(\nabla\times\vec{b}) + \vec{b}\times(\nabla\times\vec{a})$:

$$(\vec{u}\cdot\nabla)\vec{u} = \frac{1}{2}\nabla u^2 - \vec{u}\times(\nabla\times\vec{u}) = \frac{1}{2}\nabla u^2 - \vec{u}\vec{\Omega}\,. \tag{2.5}$$

We define the kinetic energy density $\mathcal{E} = u^2/2$ and the thermal energy density $\hat{p} = p/\rho$. Inserting these definitions into (2.2) yields

$$\frac{\partial \vec{u}}{\partial t} = -\nabla(\mathcal{E} + \hat{p}) + \vec{u} \times \vec{\Omega} + \nu \Delta \vec{u}\,. \tag{2.6}$$

We get an expression for the time derivative of the kinetic energy density if we multiply $\vec{u}$ from left with (2.2):

$$\vec{u} \cdot \frac{\partial \vec{u}}{\partial t} = \frac{1}{2}\frac{\partial u^2}{\partial t} = \frac{\partial \mathcal{E}}{\partial t} \tag{2.7}$$

and

$$\vec{u} \cdot \nabla(\mathcal{E}\hat{p}) = \nabla(\vec{u}(\mathcal{E} + \hat{p})) \tag{2.8}$$

because

$$\nabla(\vec{u}(\mathcal{E} + \hat{p})) = (\mathcal{E} + \hat{p}) \underbrace{\nabla \cdot \vec{u}}_{=0 \text{ due to } (2.3)} + \vec{u} \cdot \nabla(\mathcal{E} + \hat{p}). \tag{2.9}$$

We can express the viscous term in (2.2) in terms of the vorticity if we use the identity $\nabla \times (\nabla \times \vec{a}) = \nabla(\nabla \cdot \vec{a}) - \Delta \vec{a}$ and (2.3)

$$\Delta \vec{u} = \nabla(\underbrace{\nabla \cdot \vec{u}}_{=0}) - \nabla \times (\nabla \times \vec{u}) = -\nabla \times \vec{\Omega} \tag{2.10}$$

and multiply again with $\vec{u}$ from left:

$$\begin{aligned} \vec{u} \cdot \nu(\Delta \vec{u}) &= -\nu \vec{u} \cdot (\nabla \times \vec{\Omega}) && (2.11)\\ &= -\nu \vec{\Omega} \cdot (\nabla \times \vec{u}) - \nu \nabla \cdot (\vec{u} \times \vec{\Omega}) && (2.12)\\ &= -\nu \Omega^2 - \nu \nabla \cdot (\vec{\Omega} \times \vec{u})\,. && (2.13) \end{aligned}$$

In the second step we used $\nabla \cdot (\vec{a} \times \vec{b}) = -\vec{a} \cdot (\nabla \times \vec{b}) + \vec{b} \cdot (\nabla \times \vec{a})$. With the above given expressions we rewrite (2.2)

$$\begin{aligned} \frac{\partial \mathcal{E}}{\partial t} &= -\nabla \cdot \Big(\vec{u}(\mathcal{E} + \hat{p}) + \nu \vec{\Omega} \times \vec{u}\Big) - \nu \Omega^2 && (2.14)\\ &= -\nabla \cdot \mathcal{T} - \nu \Omega^2\,, && (2.15) \end{aligned}$$

where we have defined an energy transfer term

$$\mathcal{T} = \vec{u}(\mathcal{E} + \hat{p}) + \nu \vec{\Omega} \times \vec{u}\,. \tag{2.16}$$

As we can see from equation (2.15) there is a viscous loss term $\nu\Omega^2$ associated with the energy stored in the vorticity. Energy can be transferred between scales, but the total energy is conserved. This becomes clear by considering the mean energy

$$E = \langle \mathcal{E} \rangle = \frac{1}{V} \int_V \mathcal{E} \mathrm{d}V \,, \tag{2.17}$$

where the integral is taken over the whole volume. With Gauss's theorem and (2.15) we find

$$\frac{\partial E}{\partial t} = \oint_S \mathcal{T} \mathrm{d}S - 2\nu\Omega^* \approx -2\nu\Omega^* \,, \tag{2.18}$$

with the enstrophy

$$\Omega^* = \frac{1}{2} \left\langle \Omega^2 \right\rangle = \frac{1}{2V} \int_V \Omega^2 \mathrm{d}V \,. \tag{2.19}$$

The energy transfer term contributes only at the boundary of the volume, as we can see from the surface integral. If the volume is chosen to be sufficiently large, this contribution can be neglected and the energy loss is due to viscosity. In order to gain insights into the energy distribution over different spatial scales we consider the Fourier components

$$\vec{u}_k(\vec{r}) = \vec{u}_k e^{-\vec{k}\cdot\vec{r}} \tag{2.20}$$

of the velocity field. With this, the spectral energy density is given by

$$E_k = \langle \mathcal{E}_k \rangle = \frac{1}{2} \langle u_k^2 \rangle \,. \tag{2.21}$$

Kolmogorov discussed in his famous K41-theory the properties of E_k in three dimensional, homogeneous turbulence without mean flow [14–18]. The conceptual basis is the Richardson cascade [19], as shown in Fig. 2.3. Turbulent eddies of different size are stacked in decreasing order. The largest structures have size l_0. The n-th subsequent generation has a reduced size $l_n = l_0 r^{-n}$, where $n = 0, 1, 2, ...$ and $0 < r < 1$. The exact value of r has no specific meaning, but a common choice is $r = 1/2$ [14]. Furthermore, the number of eddies per unit volume increases in the n-th generation at a factor r^{3n}. This ensures, that the whole space is filled with turbulent structures. Energy is added to the system at a rate ε at the largest scale – the injection scale. It cascades then downwards with the same rate ε down to the Kolmogorov dissipation scale l_D where it is removed by dissipation. This is called a direct

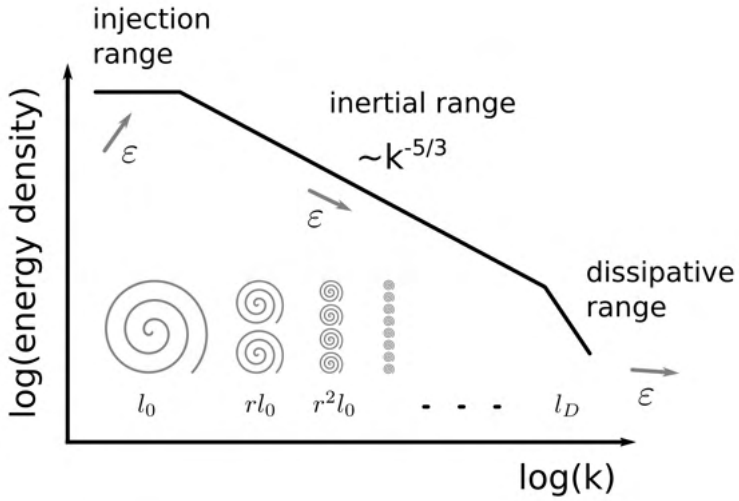

Figure 2.3: Illustration of the direct Richardson energy cascade and the energy distribution according to the K41 theory. Note: depending on the context the spatial scale is given in direct space (l) or Fourier space ($k \propto 1/l$), both are of course equivalent.

energy cascade, whereas in an inverse energy cascade the energy is transferred in the opposite direction, hence from smaller to larger scales. Two important assumptions of the K41-theory become clear from this picture: the turbulent structure is scale-invariant and the interaction is local. Scale invariance can be broken for instance if the eddies are not space filling. This leads to a modification of the energy distributions which will be discussed later 2.1.4. Localeness means that the energy exchange of an eddy of scale l involves predominantly neighbouring scales at rl (smaller) to $r^{-1}l$ (larger).

Under the above given assumptions (3D turbulence, no mean flow, homogeneous, space filling and local interaction) Kolmogorov derived from dimensional analysis the energy distribution in k-space:

$$E_k(k) \propto \varepsilon^{2/3} k^{-5/3} \tag{2.22}$$

and for the characteristic time scale

$$\tau \propto \varepsilon^{-1/3} k^{-2/3} \,. \tag{2.23}$$

Hence, most of the energy is located at large spatial scales and these large scale eddies have also a longer life time. A K41 like spectral scaling has been observed in neutral fluids in experiments as well as in simulations [20–24].

2.1.3 Energy and Enstrophy in Two Dimensions

Magnetized plasmas cannot be considered as being three dimensional isotropic media. The magnetic field leads to an asymmetry of the dynamics parallel and perpendicular to the magnetic field. Furthermore, we will see in 2.3 that the $E \times B$-drift plays a fundamental role for plasma instabilities and imprints an additional two-dimensional character on the turbulence dynamics. Therefore, we want to discuss important properties of two dimensional turbulence. As done in the previous section, we follow the derivation in [12], but similar discussions can be also found in e.g. [13, 14, 25]. In purely two dimensional turbulence with vanishing viscosity the enstrophy is a conserved quantity. In order to show this we take the curl of (2.6) and use (2.4) as well as $\nabla \times (\nabla f) = 0$:

$$\frac{\partial \vec{\Omega}}{\partial t} = \nabla \times (\vec{u} \times \vec{\Omega}) + \nu \nabla \times \Delta \vec{u}\,. \tag{2.24}$$

We can simplify this expression with help of the identity $\nabla \times (\vec{a} \times \vec{b}) = \vec{a}(\nabla \cdot \vec{b}) - \vec{b}(\nabla \cdot \vec{a}) + (\vec{b} \cdot \nabla)\vec{a} - (a \cdot \nabla)\vec{b}$ as well as $\nabla \cdot (\nabla \times \vec{u}) = \nabla \cdot \vec{\Omega} = 0$ and (2.3)

$$\nabla \times (\vec{u} \times \vec{\Omega}) = (\vec{\Omega} \cdot \nabla)\vec{u} - (\vec{u} \cdot \nabla)\vec{\Omega}\,. \tag{2.25}$$

Subsequent use of $\nabla \times (\nabla \times \vec{a}) = \nabla(\nabla \cdot \vec{a}) - \Delta \vec{a}$ yields

$$\nabla \times \Delta \vec{u} = \nabla(\nabla(\underbrace{\nabla \cdot \vec{u}}_{=0})) - \nabla \times (\nabla \times (\nabla \times \vec{u})) \tag{2.26}$$

$$= -\nabla \times \nabla \times \vec{\Omega} \tag{2.27}$$

$$= \Delta \vec{\Omega} \tag{2.28}$$

With these simplifications we can write the vorticity equation

$$\left(\frac{\partial}{\partial t} + \vec{u} \cdot \nabla\right) = (\vec{\Omega} \cdot \nabla)\vec{u} + \nu \Delta \vec{\Omega}\,. \tag{2.29}$$

The first term in (2.29) on the right hand side leads to so called vortex stretching: If the flow has a parallel divergence (c.f. Fig. 2.4) an eddy is stretched along the flow but, due to $\nabla \vec{u} = 0$, also compressed in the perpendicular plane. Due to angular momentum conservation the rotation is increased and so the vorticity.

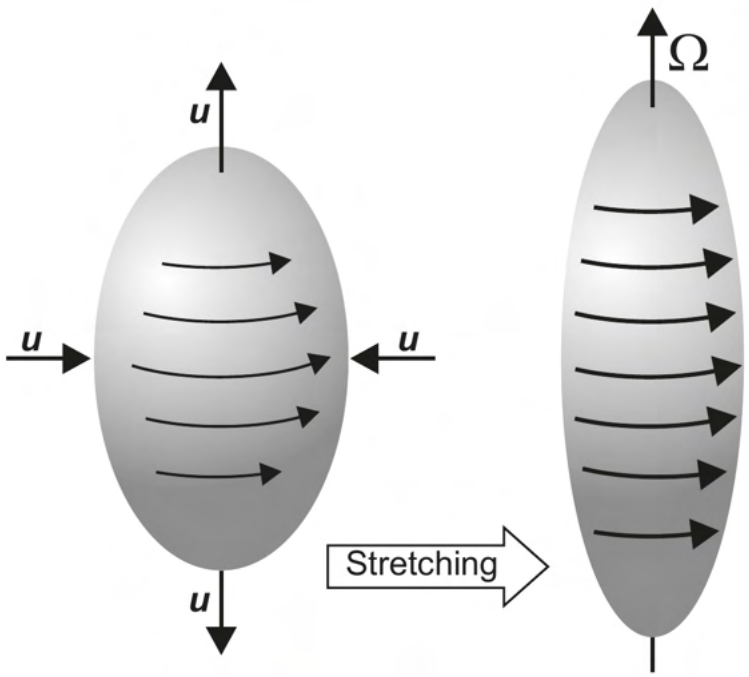

Figure 2.4: The process of vortex stretching: a parallel divergence of the flow leads to a stretching. Figure taken from [12].

In the case of a pure two dimensional motion $\vec{u} = (u_x, u_y, 0)$ the vorticity equation (2.29) can be further simplified. The vorticity becomes

$$\vec{\Omega} = \nabla \times \vec{u} = (\partial_x u_y - \partial_y u_x)\vec{e}_z = \Omega \vec{e}_z \quad \Rightarrow \quad (\Omega \times \vec{\nabla}) \cdot \vec{u} = 0.$$

Hence, the two dimensional vorticity equation is

$$\left(\frac{\partial}{\partial t} + \vec{u} \cdot \nabla\right) \vec{\Omega} = \nu \Delta \vec{\Omega} \tag{2.30}$$

$$\Leftrightarrow \frac{\mathrm{d}}{\mathrm{d}t} \vec{\Omega} = \nu \Delta \vec{\Omega}\,. \tag{2.31}$$

As a consequence, the enstrophy (2.19) and the energy are conserved quantities in two dimensional turbulence if the viscosity vanishes ($\nu = 0$). The absence of vortex stretching and the additional conservation of enstrophy is an important constraint on the turbulent dynamics and changes significantly its properties compared to the three dimensional case. In fact, the conservation of energy *and* enstrophy leads to an inverse energy cascade, where energy is transferred from smaller to larger spatial scales. In k-space the

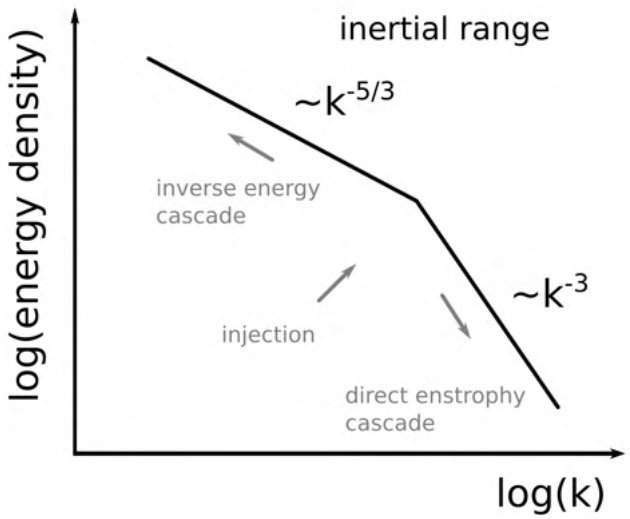

Figure 2.5: Dual cascade of energy and enstrophy in the inertial range of two dimensional turbulence.

conservation of energy and enstrophy reads [25]

$$K_E = \langle \frac{1}{2}\vec{u}^2 \rangle = \int E_{2D}(k)\mathrm{d}k \tag{2.32}$$

$$K_{\Omega^*} = \langle \frac{1}{2}\vec{\Omega}^2 \rangle = \int E_{2D}^{\Omega^*}(k)\mathrm{d}k = \int k^2 E_{2D}(k)\mathrm{d}k\,. \tag{2.33}$$

Now, assume a portion of energy is transferred from smaller to larger k. In this case the enstrophy increases, according to (2.33). Since the total enstrophy is conserved, a larger portion of energy (due to the k^2 dependency of the integrand in (2.33)) has to be transferred to smaller k. Thus, $E_{2D}(k)$ is moved towards smaller wave numbers! Kraichnan first discussed the inverse energy cascade with an intermediate injection scale [26]. A review can be found in e.g. [14,25]. Since the enstrophy contains higher derivatives than the energy, its k-dependence is stronger than for the energy. Thus, we expect the enstrophy to play a dominant role in the high-k range of the inertial range of the energy spectrum – the enstrophy cascade range. From (2.32) and (2.33) we see that the energy E_{2D} scales with the Fourier component of the velocity u_k like $E_{2D} \propto k^{-1}u_k^2$ and thus the $E_{2D}^{\Omega^*} \propto k u_k^2$. In the enstrophy cascade range in k-space the flux of enstrophy $k u_k (k E_{2D}^{\Omega^*}(k))$ should balance the enstrophy dissipation rate ε_{Ω^*}: $k^3 u_k^3 \propto \varepsilon_{\Omega^*}$. With the scaling for E_{2D} we

find for the energy in the enstrophy cascading range:

$$E_{2D}(k) \propto \varepsilon_{\Omega^*}^{2/3} k^{-3} \,. \tag{2.34}$$

As mentioned above, in the low k-range the energy cascading should be dominant. In the equilibrium case the energy flux $ku_k u_k^2$ equals the energy transfer rate ε_{2D}

$$\varepsilon_{2D} \propto k u_k^3 \quad \Rightarrow \quad E_{2D}(k) \propto \varepsilon_{2D}^{2/3} k^{-5/3} \,,$$

which is exactly the scaling (2.22) obtained for the three dimensional case. However, the important difference here is the lack of an energy sink or dissipation range in the two-dimensional case. Energy, which is injected at intermediate scales, cascades in an inverse cascade towards smaller wave numbers where it accumulates until some saturation mechanism is activated. In this sense, ε_{2D} is rather an energy transfer rate than an energy dissipation rate as it is in the three dimensional case.

2.1.4 Experimental Implications

As we have seen in the previous section, the additional conservation of enstrophy in two dimensions in the viscous limit leads to the dual cascade of energy and enstrophy and a modification of the energy spectrum compared to the three dimensional case. The experimentally accessible energy distribution laws (2.22), (2.34) and (2.35) are based on some properties of the underlying physics system, which we had known before. However, in an experiment it is desirable to deduce from the measured data the underlying physics. Thus, it is helpful to know how robust the found relationships are with respect to deviations in the underlying physics model and what kind of requirements experiments have to fulfil in order to make statements.

In the K41 theory, a fundamental assumption is the space filling property of the eddies in the Richardson cascade and a violation of this property leads to a modification of the k-dependence of E_k, which is described by the β-model [14]. Here, in each hierarchy step of the Richardson cascade the volume filled with eddies decreases by a factor $\beta \in [0, 1]$. In this case the modified energy scaling reads [14]:

$$E(k) \propto k^{\frac{5}{3}+\frac{3-D}{3}} \quad \text{with} \quad D = 3 - \frac{\ln \beta}{\ln r} \,. \tag{2.35}$$

For $D = 3$ the Kolmogorov scaling (2.22) is recovered, for smaller values of D (e.g. because β is smaller for fixed r) the energy decay is steeper or equivalently there is relative more energy at smaller k than at larger k. Also the energy dissipation scale changes, hence where dissipative effects start to become relevant

$$l_D \approx l_0 R^{-\frac{3}{1+D}} \quad D > -1\,, \tag{2.36}$$

where $R = l_0 v_0/\nu$ is the integral-scale Reynolds number. Thus smaller values of D, compared to the space filling case, move the dissipation scale to smaller spatial scales. However, not only the violation of the space filling assumption modifies the spectrum. In case of shear turbulence where e.g. a background flow $\vec{u} = (u_x, 0, 0)$ breaks the homogeneity the modified spectrum becomes [25, 27]

$$E(k) \propto \varepsilon^{2/3} k^{-5/3} \left(1 - C_N \,\mathrm{sgn}(\dot{\varepsilon})(k l_N)^{-2/3}\right)\,, \tag{2.37}$$

where C_N is some numerical constant, the length scale $l_N = \varepsilon^2/\dot{\varepsilon}^{3/2}$ characterizes the turbulent energy production and $\mathrm{sgn}(x) = 1$ if $x > 0$ else -1 and $\dot{\varepsilon} \equiv \mathrm{d}\varepsilon/\mathrm{d}t$. In the limit $k \to \infty$ the usual Kolmogorov scaling $E(k) \propto k^{-5/3}$ is recovered from (2.37). However, for small $k \to 0$ we find $E(k) \propto k^{-7/3}$ – a steepening of the energy distribution similar to the β-model. Here, it is simple to study mathematically the asymptotic behaviour. However, in a an experiment it requires to cover a rather large range of spatial scales which is often not possible. For example, the range of scales microturbulence can cover in a fusion experiment like Wendelstein 7-X reaches from the system scale of approximately meters down to the ion larmor radius in the millimetre range, thus covering three orders of magnitude. However, diagnostic resolution over these scale ranges is mostly not possible.

2.2 Transport

2.2.1 Confinement Time

The importance of turbulent phenomena in the context of magnetic confinement fusion arises from the fact, that they can influence significantly the the energy and particle transport in a fusion plasma. As already noted in Sec. 1.1 a good confinement is crucial for the feasibility of a thermo nuclear

power plant. In order to control and predict the transport, it is desirable to understand the underlying mechanisms. A global approach to measure all energy transport mechanisms in a plasma is the energy confinement time τ_E, which is defined over the global conservation of energy. The concept of confinement times is well established and can be found in many textbooks about fusion physics (e.g. [12]). The total plasma energy W can only be changed by plasma heating P_{net} or transport mechanisms which lead to losses on a time scale of τ_E:

$$\frac{\mathrm{d}W}{\mathrm{d}t} = P_{\text{net}} - \frac{W}{\tau_E}\,. \tag{2.38}$$

The total energy content of the plasma has contributions from electrons and ions

$$W = W_e + W_i = \int_V \frac{3}{2}(n_e T_e + n_i T_i)\mathrm{d}V \tag{2.39}$$

and the net heating power P_{net} accounts for all heating sources and sinks. Heating sources can be neutral beam injection (NBI), electron cyclotron resonance- (ECRH) or ion cyclotron resonance heating (ICRH) and - in a tokamak - the ohmic heating by the strong toroidal current. Sinks of energy in the plasma volume are atomic line radiation, bremsstrahlung and, to a small extent, ionisation of neutral atoms and charge exchange reactions of ions with neutrals and need to be accounted for in P_{net} if the confinement time is attributed to energy transport processes.

Similarly, the particle transport is characterized by the particle confinement time τ_p. Particle sources are gas puffing, pellet injection (frozen hydrogen pellets) and recycling as well as particles from the NBI heating. Recycling describes the process of ions which are neutralized at the plasma wall and reenter the plasma again afterwards.

The determination of the confinement times from first principle is still not possible due to the complexity of all involved transport processes. However, the experimental determination is strait forward. In a stationary plasma the time derivative of W vanishes and it is $\tau_E = W/P_{\text{net}}$. The measurement of confinement times allows for setting up databases with measurements from different machines and to follow a statistical approach by deriving scaling laws from fits on this data. These fits can then serve as an engineering help to inter- or extrapolate to new machines. Such an empirical scaling law is given by [28]

$$\tau_{\mathrm{E}}^{\mathrm{ISS95}} = 0.079\, a^{2.21}\, R^{0.65}\, P^{-0.59}\, n_{\mathrm{l}}^{0.51}\, B^{0.83}\, \iota_{2/3}^{0.4}\,, \tag{2.40}$$

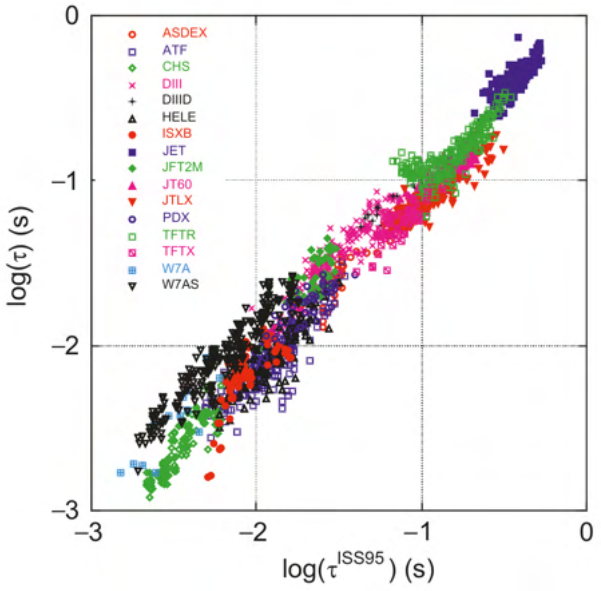

Figure 2.6: Comparison of the measured energy confinement time with the ISS95 scaling. Taken from [28].

where a is the averaged minor plasma radius, R is the major plasma radius, P the heating power (in MW), n_l the line-averaged density (in $10^{19}\,\mathrm{m}^{-3}$), B the magnetic field strength and $\iota_{2/3}$ is the rotational transform taken at 2/3 of the plasma radius. It is remarkable at this point, that the confinement time decreases with increased heating power. As we will see in Sec. 2.3 turbulence is driven by gradients. Although the negative correlation between τ_E and P has not been fully clarified, it seems as increased heating power leads to steeper gradients which then increase the turbulent transport.

2.2.2 Diffusion Coefficients

A scaling law like (2.40) parametrizes certain physics and can be a valuable basis for educated guesses in uncovered areas of parameter space. In addition, it allows to detect changes of the underlying physics if situations appear which significantly deviate from the already known correlation. However, it is very hard to gain any knowledge about the underlying physics mechanisms. Thus, extrapolation entails always the risk of getting into parameter space regions where the previous correlations are not valid anymore because e.g. a threshold is exceeded and non-linear effects become dominant. With this

in mind, it is desirable to develop a microscopic understanding in general and for transport mechanisms in particular. The transport of energy and particles in plasmas has been extensively studied over the last decades. The existing theories are categorized into three different groups: classical, neoclassical and anomalous or turbulent transport. Classical transport considers only binary collisions of particles in homogeneously magnetized plasmas. All effects due to magnetic field gradient through e.g. curvature are described by the neoclassical transport theories. Historical, it has turned out that the observed level of transport could not be satisfactorily described by classical and neoclassical transport and was thus attributed as anomalous transport. Today it is believed, that the transport caused by turbulent phenomena – the turbulent transport – is responsible for this additional contribution.

The fundamental concept is the process of diffusion. We can motivate this by considering a one dimensional random walk with step length l and τ being the time needed for single step. The position is denoted by (x, t), where x is the discrete spatial and t the discrete temporal coordinate. The probability to step to the left or to the right should be equally $1/2$. The state at position (x, t) depends only on the neighbouring positions but should be independent of time. We write thus for the probability P to find the walker at position $(x, t + \tau)$:

$$P(x, t+\tau) = \frac{1}{2}P(x-l, \tau) + \frac{1}{2}P(x+l, \tau) \tag{2.41}$$

$$\Leftrightarrow \tau\frac{P(x, t+\tau) - P(x, \tau)}{\tau} = \frac{l^2}{2}\frac{(P(x-l, \tau) + P(x+l, \tau) - 2P(x, t+\tau)}{l^2}\,. \tag{2.42}$$

In the limit of infinite observation time and vanishing step width the area covered by the random walker will become more dense, so that the finite difference equation becomes a differential equation

$$\tau\frac{\partial P}{\partial t} = \frac{l^2}{2}\frac{\partial^2 P}{\partial x^2} \quad \Leftrightarrow \quad \frac{\partial P}{\partial t} = D^{\mathrm{RW}}\frac{\partial^2 P}{\partial x^2}\,, \tag{2.43}$$

which is a diffusion equation with diffusion coefficient

$$D^{\mathrm{RW}} = \frac{l^2}{2\tau}\,. \tag{2.44}$$

Hence, the diffusivity depends quadratic on the step width and is inversely proportional to the time step. Considering particle transport in plasmas, particularly the transport or diffusion perpendicular to the magnetic field

is of interest. The random walker corresponds to a particle whose guiding center, originally following a field line, leaves this magnetic field due to any transport process e.g. by collisions. As we can see from (2.44), the discussion of transport breaks (often) down to the determination of the characteristic length and time scales for the considered process.

2.2.3 Classical Transport

The classical transport considers only binary collisions between particles. From momentum conservation it follows, that a nett transport happens only if particles of different type collide. If we consider the electron-ion collision, the electron is scattered at the much heavier ion. The characteristic length scale is here the electron Larmor radius ρ_{Le}. The time scale is given by the electron-ion collision time τ_{ei}. With this, the diffusion coefficient reads [12]

$$D_{cl} = \frac{\rho_{Le}^2}{2\tau_{ei}} = \frac{e^2 n_e \ln\Lambda\sqrt{m_e}}{8\sqrt{2}\pi\epsilon_0^2 B^2\sqrt{T_e}}\,, \tag{2.45}$$

where e is the elementary charge, n_e the electron density, Λ the Coulomb logarithm (which is around 18 for a fusion reactor [29]), m_e the electron mass, ϵ_0 the vacuum permittivity, B the magnetic field strength and T_e the electron temperature. It turns out, that the classical diffusion coefficient increases linearly with collision frequency $\nu \propto 1/\tau$. Furthermore, one can show, that the classical transport is intrinsically ambipolar which means that (2.45) ist valid for electrons as well as ions [12]. Assuming a fusion reactor is dominated by classical transport we can estimate its size from (2.44) to be $l_{cl} = \sqrt{2\tau D_{cl}} \propto \tau\sqrt{n_e}/(BT_e^{1/4})$. For unfavourable choice of values $n_e = 2\times10^{20}\,\mathrm{m}^{-3}$, $T_e = 10\,\mathrm{keV}$, $B = 1\,\mathrm{T}$ and a confinement time $\tau = 3\,\mathrm{s}$ we find $l_{cl} \approx 7\,\mathrm{cm}$. This means if the transport in a fusion reactor is only dominated by classical transport its minor radius would be in the order of centimetres! However, in reality fusion devices are much larger. The International Thermonuclear Experimental Reactor (ITER), which is the first fusion device aiming to produce net fusion power, has a minor radius of 2 m [3, 4]. A fundamental reason for this difference is the dominance of neoclassical and turbulent transport over classical transport which will be discussed in the following.

2.2.4 Neoclassical Transport

In toroidal geometry the much more complex particle trajectories lead to a number of new effects. Particles are subject to a charge dependent magnetic drift in vertical direction. Without twisted magnetic field lines, the resulting vertical charge separation would cause an electric field giving rise to an outward directed $E \times B$-drift and unacceptable particle losses. If the magnetic field lines are twisted by adding a small poloidal field, the vertical drifts can averages out. However, the drift leads to a deviation from the underlying flux surface.

Since the magnetic field is stronger on the inboard than on the outboard side, particles which move along the field lines experience a gradient in the magnetic field strength, which forms a magnetic mirror. For some of the particles the parallel velocity is small enough to be trapped – these particles are referred to as trapped particles or banana particles. The latter name comes from the fact, that the projection of trapped particle trajectories on to the poloidal plane has the shape of a banana. In contrast, particles with sufficiently high parallel velocity leave the magnetic mirror, hence they are called passing particles.

Pfirsch-Schlüter Regime

Passing particles lead to an additional correction of (2.45). If the collision time is larger than the transit time (the time a particle needs to complete a poloidal circulation), $\tau_{ei} > \tau_{tr}$ the deviation of the guiding center trajectory from the flux surface is at maximum and the diffusion coefficient is given by [12]

$$D_{\mathrm{ps}} = \frac{1}{\iota^2} D_{\mathrm{kl}} \,. \tag{2.46}$$

For a typical value of $\iota = 1/3$, (2.46) is about a factor 20 larger than the classical diffusion. If $\tau_{ei} < \tau_{tr}$ the deviation of the guiding center decreases with increased collision frequency and the contribution of the Pfirsch-Schlüter transport scales like $1/\nu \propto \tau$.

Banana Regime

Even more transport is caused by banana particles. We consider banana particles, whose effective collision frequency is much smaller than their bounce time, thus they can complete a full banana orbit before they collide. The diffusion coefficient for electrons in this banana regime reads [12]

$$D_{\mathrm{ba}} = \frac{1}{\iota^2 \epsilon^{3/2}} D_{\mathrm{kl}} = \frac{1}{\epsilon^{3/2}} D_{\mathrm{ps}} \,, \tag{2.47}$$

with $\epsilon = a/R$ being the inverse aspect Ration, a the minor – and R the major radius. Trapped particles contribute by a factor $\frac{1}{\epsilon^{3/2}} > 1$ stronger than the passing particles in D_{ps}. For a typical tokamak the contribution from banana particles is about a factor 50 larger than the classical diffusion coefficient, thus requiring larger experiments than expected from classical transport.

Plateau Regime

In this regime, banana particles undergo collisions which prevent them from circulating a full banana orbit – the effective step length is reduced. If the collisions time equals the bounce time i.e $\tau_{ei} = \tau_{tr}$ there are effectively no banana particles anymore. In this regime, the diffusion coefficient is independent of the collision frequency [12]

$$D_{\mathrm{pl}} = \frac{1}{\iota^2} \frac{\rho_L^2}{2\tau_{tr}} \,. \tag{2.48}$$

In figure 2.7 the neo classical diffusion coefficient is shown as function of the collision frequency. At low collision frequency the banana particle trajectories are not perturbed and D scales linearly with ν. With increased collisions, the particles cannot circulate a full banana orbit, thus the characteristic step width reduces and the transport coefficient enters the plateau regime. When banana orbits are completely suppressed, the contribution of passing particles becomes dominant and define the Pfirsch-Schlüter regime.

Modification in Stellarator Geometry

The discrete nature of the stellarator magnetic field coils leads to an important change of the diffusion coefficient for small collision frequencies. The

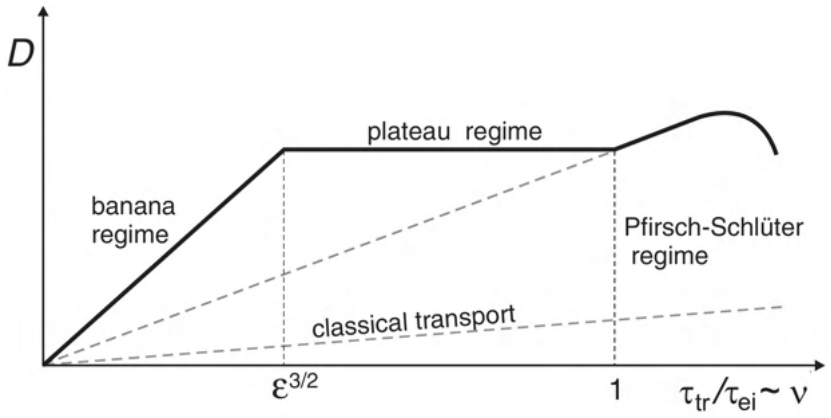

Figure 2.7: Qualitative sketch of the neoclassical diffusion coefficient D for a tokamak as function of the collision frequency for fixed temperature, hence $\nu \propto n$. Modified from [30], p. 234.

magnetic field coils imprint a ripple on the magnetic field in which particles can be trapped if their parallel energy is not sufficiently high. In contrast to the particles being trapped in banana orbits, the magnetic ripple extends all the way to the outer wall and, thus, the trapped particles are rapidly lost from the plasma. The helical trapping causes a localisation of the so called helical trapped particles on one side of the torus. Due to this localisation the magnetic drift v_D does not average out and the particle is lost. This loss is only limited, if the created gap in the distribution function is not filled fast enough by ion-ion or electron-electron collisions. This non diffusive process happens if the helically trapped particles are collisionless. Collisions stabilize this process if the effective collision time τ_{eff} is less than the loss time. In this case we can use again the random walk ansatz. Since the particles drift in between the collisions, the characteristic step width is given by $\delta r = v_D \tau_{\text{eff}}$ and the diffusion coefficient reads in the absence of an electric field [12]

$$D_{1/\nu} = \sqrt{\epsilon_h} \frac{(v_D \tau_{\text{eff}})^2}{2\tau_{\text{eff}}} \propto \tau_{\text{eff}} \propto \frac{1}{\nu} \,. \tag{2.49}$$

The characteristic reduction of $1/\nu$ with increased collision frequency is here eponymous. The quantity ϵ_h quantifies the helical ripple. It can be thought of measuring the difference between maximum and minimum magnetic field the particle sees, but its specific value is in general complex to obtain due to the nontrivial stellarator magnetic field geometry. Expressing (2.49) in terms

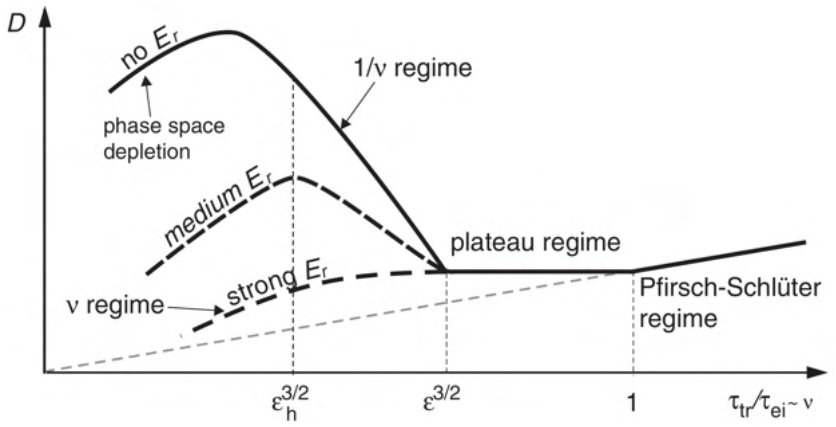

Figure 2.8: Qualitative sketch of the neoclassical diffusion coefficient D for a stellarator as function of the collision frequency for different strenght of the radial electric field and fixed temperature, hence $\nu \propto n$. Taken from [30], p. 239.

of plasma parameter one finds [12]

$$D_{1/\nu} \propto \frac{\epsilon_h^{3/2} T_e^{7/2}}{B^2 n_e} \,. \tag{2.50}$$

The strong temperature dependence is in contrast to tokamaks, where $D_{\text{tok}} \propto 1/\sqrt{T_e}$ (c.f. (2.45)). This has a dramatic consequence for non-optimized stellarators, since future stellarator fusion power plants need to operate at high temperatures. However, it turns out that radial electric fields have a favourable effect on the transport. These fields are generated by the plasma itself because the transport of helical trapped particles is not ambipolar, which means it is different for electrons and ions. If the electrons are primarily heated, it can happen that electrons are in the $1/\nu$ regime whereas colder ions are in the plateau regime. The resulting increased loss of electrons relative to the ions leads to a positive charging of the plasma. This state is called *electron-root confinement*. In the *ion-root* confinement regime, the plasma is charged negatively because of the higher losses of ions.

Radial electric fields bend the trajectory of helical trapped particles in the poloidal direction. If this electric field E_r is sufficiently strong, the diffusion coefficient becomes again dependent on the spatial deviation from the flux surface. The time scale for the time they drift is given by the time $\tau_{E\times B}$ they need for a poloidal circulation due to the $E_r \times B$-drift. Hence, the step width

can be estimated to be $\delta r \approx v_D \tau_{E\times B}$ and the diffusion coefficient is [12]

$$D_\nu \approx \frac{(v_D \tau_{E\times B})^2}{2\tau_e i} \propto \nu \,. \tag{2.51}$$

The temperature dependence is much weaker

$$D_\nu \propto \frac{n_e \sqrt{T_e}}{E_r^2} \tag{2.52}$$

and the electric field reduces the diffusion as expected. Figure 2.8) summarizes the above mentioned findings.

2.2.5 Fluctuation Driven Transport

Fluctuations can cause transport. In contrast to classical or neoclassical diffusion, the transport is convective rather than diffusive since it is induced by the fluctuating eddy velocity. To see this, it is convenient to decompose a fluctuating quantity f as follows

$$f = f_0 + \tilde{f} \,, \tag{2.53}$$

where f_0 describes the constant background value and $\tilde{f}$ the fluctuating part. Such a quantity could be e.g the density n or pressure p. We are interested in the time averaged values of f and denote the average over one period with $\langle\cdot\rangle$. We demand $\langle f_0\rangle = f_0$ since f_0 is constant. Furthermore, it should $\langle\tilde{f}\rangle = 0$ so that $\tilde{f}$ describes purely fluctuations. This is known as Reynolds decomposition [31]. We consider the associated flux

$$F = \langle f u\rangle = \langle (f_0 + \tilde{f})(u_0 + \tilde{u})\rangle = f_0 u_0 + \langle \tilde{f}\tilde{u}\rangle \tag{2.54}$$

where we decomposed f and velocity u. For f being the density F describes the particle flux and for $f = p$ the heat flux. The velocity fluctuation is caused by an $E\times B$-drift due to a potential fluctuation $\tilde{\phi}$

$$\tilde{u} = -\frac{\nabla\tilde{\phi}}{B} \,. \tag{2.55}$$

We want to consider the flux $\tilde{F} = \langle\tilde{f}\tilde{u}\rangle$ caused by the fluctuations and write $\tilde{f}$ and $\tilde{\phi}$ as Fourier modes

$$\tilde{f} = \bar{f}\cos(kx - \omega t) \tag{2.56}$$

$$\tilde{\phi} = \bar{\phi}\cos(kx - \omega t + \varphi) \,, \tag{2.57}$$

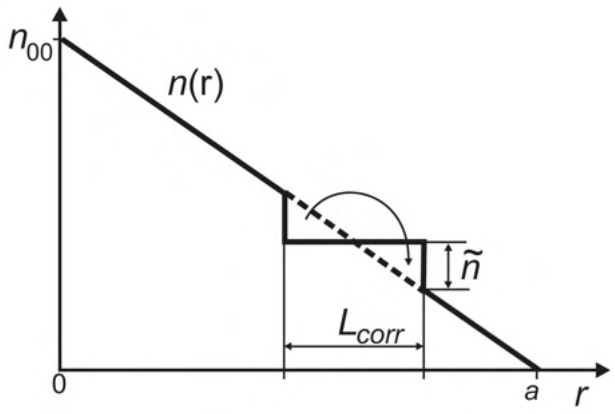

Figure 2.9: Fluctuation amplitude according to the mixing length model. Taken from [12].

with amplitudes $\bar{f}$ and $\bar{\phi}$, wavenumber k, circular frequency ω and phase shift φ between both quantities. The averaged flux from the fluctuations reads then

$$\tilde{F} = \frac{k\bar{f}\bar{\phi}}{LTB}\int_0^T\int_0^L \cos(kx-\omega t)\sin(kx-\omega t+\varphi)\,\mathrm{d}x\,\mathrm{d}t \tag{2.58}$$

$$= \frac{k\bar{f}\bar{\phi}}{2B}\sin(\varphi)\,, \tag{2.59}$$

with the temporal $T = 2\pi/\omega$ and spatial $L = 2\pi/k$ period. It turns out, the flux is at maximum if the phase difference is $\varphi = \pi/2$, whereas for $\varphi = 0$ there is no flux. Furthermore, particle and heat flux can be in principal decoupled if the phase shift is different for density and pressure perturbations. This can be desirable in situations where particle confinement should be reduced e.g. to flush out impurities while the energy confinement should remain high.

The amplitude can be estimated via the mixing-length model (c.f. figure 2.9). An eddy convects density over a characteristic length $L_{\mathrm{corr}} \approx 2\pi/k$ on a background gradient ∇n , which leads to a fluctuation in the density of

$$\tilde{n} = L_{\mathrm{corr}}|\nabla n|\,. \tag{2.60}$$

Note that the convection process is intrinsically ambiploar, which is in contrast to the neoclassical transport. As discussed above, turbulent length scales are coupled and finding the correct value for L_{corr} is a non trivial task. If one takes the wave number as a measure for the correlation length $L_{\mathrm{corr}} \propto 1/k$ we see immediately that the low wavenumber part in the spectrum contributes more strongly to the fluctuation level. An approach to

estimate the characteristic length is to take the (inverse) wave number from the fastest growing mode as an estimate for the spatial scale and the (inverse) growth rate as estimate for the time scale. However, turbulence may form coherent structures through so called Reynolds stress which changes the relevant scales and this approach may give incorrect results (c.f Sec 2.4).

2.3 Drift Waves

2.3.1 The Physical Picture

The topic of drift wave turbulence addresses often a rather wide range of plasma fluctuations and is not always consistently defined. It appears, that it describes plasma fluctuations which are

- low frequent: $\omega \ll \omega_{\mathrm{ci}}$, the fluctuation frequency ω is well below the ion cyclotron frequency ω_{ci}
- gradient driven: gradients in temperature or density result in a pressure gradient which presents an energy source for the instability
- electrostatic: the ambient magnetic field is not disturbed
- and the perpendicular motion is governed by the $E\times B$-drift due to the fluctuating electric potential.

Beside this general categorization, two types of linear instability mechanisms can be identified: the drift wave and the interchange instability. Although they present conceptionally different mechanisms, in reality they appear often both at the same time but their contribution might be different so that the the problem can be simplified by considering only the dominant mechanism.

The drift wave instability is a three dimensional feature of a magnetized plasma as shown in Fig. 2.10. An initial perpendicular perturbation in density at a certain position along the magnetic field imposes a force on the ions and electrons. The much lighter electrons react on a faster time scale than the ions on the force and move along the magnetic field until the created electric field balances the pressure gradient. The ions are subject to a

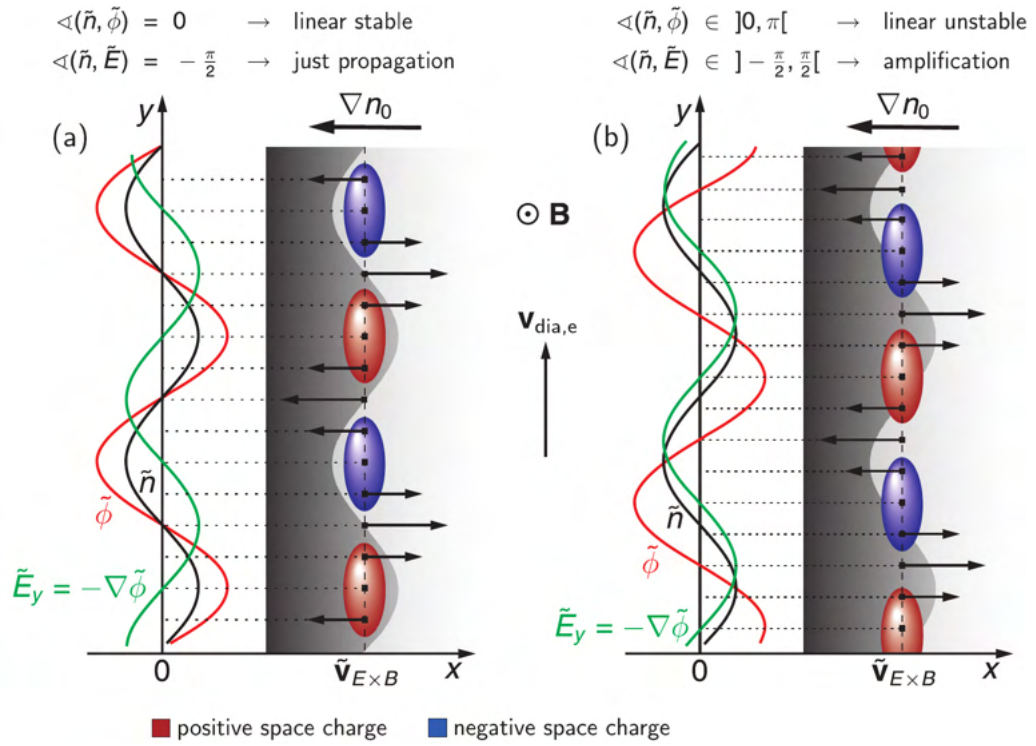

Figure 2.10: Scheme of the drift wave mechanism for the linear stable(a) and linear unstable case (b). Taken from [32], p. 6.

perpendicular polarization drift due to the non-stationary electric field. The high parallel mobility of the electrons leads to an elongated structure where $k_\parallel \ll k_\perp$ but $k_\parallel \neq 0$ (throughout the thesis the subscript $\parallel$ and $\perp$ denotes the parallel respectively perpendicular component of a quantity with respect to the ambient magnetic field). This causes the shown charge distribution and resulting $E \times B$-drifts. If the electrons are *adiabatic* i.e. they react immediately on the perturbation, the potential and density perturbation are in phase (Fig. 2.10 (a)). The perturbation is stable and propagates downwards with electron diamagnetic drift velocity. *Non-adiabatic* electrons do not react immediately on the perturbation because of finite resistivity, induction or Landau damping (Fig. 2.10 (b)). As a consequence, there is a non-zero phase difference between density and potential. The resulting $E \times B$-drift moves upwards in regions where it enhances the perturbation, hence the drift wave becomes unstable.

The interchange instability is a two-dimensional mechanisms which occurs in magnetized plasmas with a perpendicular magnetic field gradient. It can

be seen as the equivalent of the Rayleigh-Taylor instability in neutral fluids. Figure 2.11 shows on the high field and the low field side of a toroidal plasma a pressure perturbation. The pressure gradient causes a diamagnetic current $\vec{j}_{\text{dia}} = -\nabla p \times \vec{B}/B^2$ along the isobar of the perturbation. We consider the situation on the low field/outboard side: Since the magnetic field strength increases, the diamagnetic drift velocity $\propto 1/B$ decreases, charge accumulates and $\vec{j}_{\text{dia}}$ has a finite divergence ($\nabla \cdot \vec{j} = -\partial\rho/\partial t$, with ρ being the charge density). The resulting electric field causes an $E\times B$-drift which destabilizes the perturbation on the low field side and stabilizes on the high field side. Regions in which the perturbation is stabilized are regions of good curvature, whereas destabilization has bad curvature. The type of curvature is defined via

$$\vec{\kappa} \cdot \nabla p \begin{cases} < 0 : \text{good curvature} \\ > 0 : \text{bad curvature} \end{cases} \tag{2.61}$$

where $\vec{\kappa}$ is the curvature vector. It points towards the local curvature center and its magnitude is inversely proportional to the local curvature radius. Mathematically it is defined as

$$\vec{\kappa} = \left(\vec{b} \cdot \nabla\right) \vec{b} \quad \text{with} \quad \vec{b} = \frac{\vec{B}}{B}\,. \tag{2.62}$$

Depending on whether the ion- or electron temperature dominates the pressure gradient the instability is called ion temperature gradient (ITG) or electron temperature gradient (ETG) instability.

2.3.2 Two Fluid Equations

In the following we want to derive two simple models for drift wave turbulence in two and three dimensions in order to study their most important properties. This can be found e.g. in [12]. The plasma dynamic is described within the two-fluid picture, i.e. the following equations:

The continuity equation

$$\frac{\partial n_s}{\partial t} + \nabla \cdot (n_s \vec{u}_s) = 0 \quad \Leftrightarrow \quad \mathrm{d_t}\, n_s + n_s \nabla \cdot \vec{u}_s \tag{2.63}$$

and the momentum equation

$$m_s n_s\, \mathrm{d_t}\, \vec{u}_s = -\nabla p_s + q_s n_s (\vec{E} + \vec{u}_s \times \vec{B}) + \vec{R}_s \tag{2.64}$$

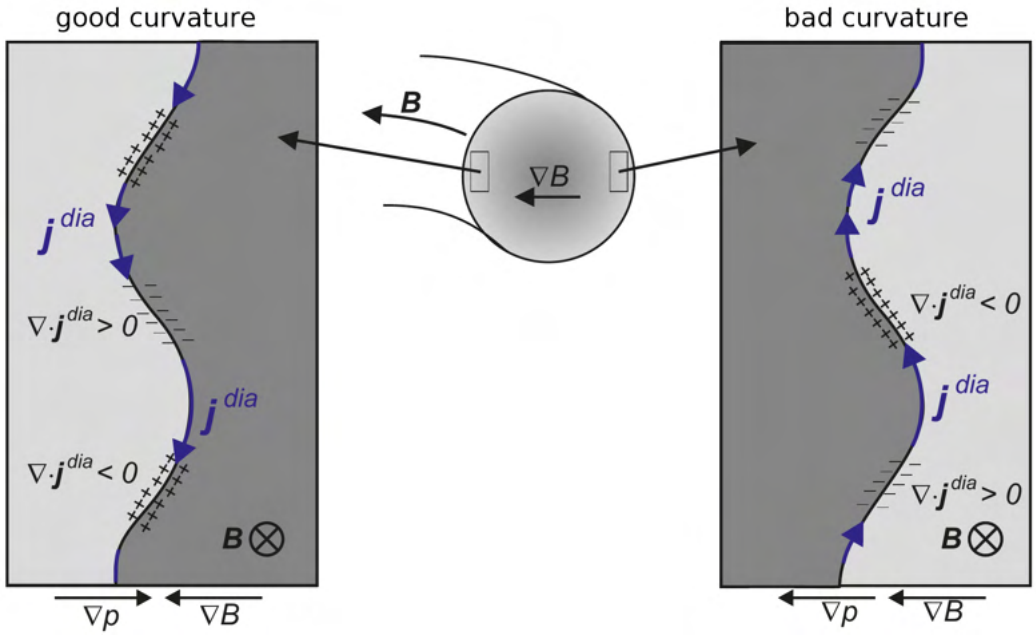

Figure 2.11: Scheme of the interchange mechanism. Modified from [12], p. 119

the subscript $s = e, i$ denotes the species, m_s is the mass, n_s the particle density, p_s the pressure, q_s the charge, $\vec{E}$ the electric and $\vec{B}$ the magnetic field and $\vec{R}_s$ accounts for forces due to electron-ion collisions. The operator $\mathrm{d_t}$ denotes the convective derivative

$$\mathrm{d_t} = \frac{\partial}{\partial t} + \vec{u}_{E\times B} \cdot \nabla \,. \tag{2.65}$$

The quasi neutrality condition $n_e \approx n_i = n$ and the continuity equation (2.63) yields for the total current density $\vec{j} = en(\vec{u}_e - \vec{u}_i)$

$$\nabla \cdot \vec{j} = 0 \,. \tag{2.66}$$

We split the current density into a parallel and perpendicular component $\vec{j} = \vec{j}_\perp + \vec{j}_\parallel$. The quasi neutrality condition couples thus parallel and perpendicular dynamic:

$$\nabla_\perp \vec{j}_\perp = -\nabla_\parallel \vec{j}_\parallel \,. \tag{2.67}$$

Any force in perpendicular direction leads to a drift of the guiding centres, which can be derived from the momentum equation (2.64). We consider the

following contributions [12]

$$E\times B\text{-drift:} \quad \vec{u}^{\perp}_{E\times B} = \frac{\vec{E}\times\vec{B}}{B^2} \tag{2.68}$$

$$\text{diamagnetic drift:} \quad \vec{u}^{\perp}_{\text{dia}} = \frac{\nabla p_s \times B}{q_s n_s B^2} \tag{2.69}$$

$$\text{polarization drift:} \quad \vec{u}^{\perp}_{\text{pol}} = \frac{m_s}{q_s B^2}\,\mathrm{d_t}\,\vec{E}_{\perp}\,. \tag{2.70}$$

In order to find a set of equations we take the continuity equation (2.63) and the quasi neutrality condition (2.67) and find expressions for $\vec{u}$, $\vec{j}_{\perp}$ and $\vec{j}_{\parallel}$.

2.3.3 Hasegawa-Wakatani Model

The Hasegawa-Wakatani model is a self consistent description for drift wave turbulence in a homogeneous magnetic field in three dimensions. It consists of two non-linear partial differential equations for density and potential. In the following section we want to derive the model equations. As mentioned in section 2.3.1 drift waves can occur in arbitrary magnetic field geometry. For simplicity we consider a homogeneous magnetic field $\vec{B} = B\vec{e}_z$, a constant temperature and cold ions i.e. $T_i = 0$. Hence, the pressure gradient is caused by a density gradient with gradient length $L_n = |n_0/\nabla n_0| = |\nabla \ln n_0|^{-1}$. The derivation is done within the validity of the *drift ordering*

$$\frac{\omega}{\omega_{\text{ci}}} \approx \frac{\tilde{n}}{n_0} \approx \frac{e\tilde{\phi}}{T_e} \approx \frac{\rho_s}{L_n} \approx \delta \ll 1\,, \tag{2.71}$$

with $\omega = eB/m_i$ thy ion gyro frequency and $\rho_s = \sqrt{miT_e}/(eB)$ the drift parameter, which is here the characteristic length scale. The first term in (2.71) is the usual low frequency assumption. The second term $\tilde{n}/n_0$ states, that the density fluctuation is small compared to the unperturbed density. This leads to the third term via the Boltzman relation [12]

$$\frac{\tilde{n}}{n_0} = \frac{e\tilde{\phi}}{T_e} \quad \text{if} \quad e\tilde{\phi} \ll T_e\,. \tag{2.72}$$

However, it is important to note that the exact fulfilment of the Boltzman (2.72) relation is equivalent with adiabatic electrons and presents therefore a linearly stable situation. The drift ordering requires only density and potential perturbations to be in the same order ($\approx$) rather than equality ($=$).

From the mixing length model (2.60) we find with $L_{\text{corr}} = \rho_s$

$$\tilde{n} \approx \rho_s \nabla n_0 \Rightarrow \nabla \tilde{n} \approx \frac{\tilde{n}}{\rho_s} \approx \frac{\rho_s \nabla n_0}{\rho_s} = \nabla n_0 \,, \tag{2.73}$$

hence the perpendicular gradients in background and fluctuating density are comparable.

Perpendicular Dynamic

Since the ions are cold, the diamagnetic drift (2.69) can be neglected and the ion dynamic perpendicular is dominated by the $E\times B$(2.68) and polarization drift (2.70) (without resistivity)

$$\vec{u}_{\perp,i} = \frac{\vec{E} \times \vec{B}}{B^2} + \frac{m_i}{eB^2} \,\mathrm{d_t}\, \vec{E}_\perp \,. \tag{2.74}$$

The electrons are much lighter than the ions $m_i/m_e > 1836$ hence the contribution of the polarization drift is very small and we find for the electrons (without resistivity)

$$\vec{u}_{\perp,e} = \frac{E \times \vec{B}}{B^2} + \frac{\nabla p_e \times \vec{B}}{enB} \,. \tag{2.75}$$

The quasi neutrality condition (2.67) reads with (2.74) and (2.75)

$$-\nabla_\parallel \cdot \vec{j}_\parallel = \nabla \cdot \vec{j}_\perp = en \nabla_\perp \cdot (\vec{u}_{\perp,e} - \vec{u}_{\perp,i}) \tag{2.76}$$

$$= -\nabla_\perp \cdot \frac{n m_i}{B^2} \,\mathrm{d_t}\, \vec{E}_\perp \,, \tag{2.77}$$

where we used the Boussinesque approximation and that, due to the homogeneous magnetic field, the divergence of the electron diamagnetic drift term vanishes. The Boussinesque approximation allowed us to neglect derivatives of n and B [12]. With $\vec{E}_\perp = -\nabla\phi$ we find the *vorticity equation*

$$\frac{m_i n}{B^2} \,\mathrm{d_t}\, \nabla_\perp^2 \phi = \nabla_\parallel j_\parallel \,. \tag{2.78}$$

The vorticity occurs in the derivative of the electric potential. A potential perturbation leads to a circular $E\times B$-motion, thus

$$\vec{\Omega} = -\nabla \times u_{E\times B} = -\nabla \times \left(\vec{E} \times \frac{\vec{B}}{B^2} \right) = -(\nabla_\perp \cdot \vec{E}_\perp) \frac{\vec{B}}{B^2} = (\nabla_\perp^2 \phi) \frac{B}{B^2}. \tag{2.79}$$

Note that the vorticity in plasma physics has a different signum than the definition (2.4) for neutral fluids.

Parallel Dynamic

In parallel direction we neglect the motion of the ions completely due to their high inertia. The generalized Ohm's law in the electrostatic limit yields for the parallel current density [12]

$$\vec{j}_\parallel = \frac{e}{m_e \nu} \nabla_\parallel (\tilde{p}_e - e n_0 \tilde{\phi}) \,. \tag{2.80}$$

If we insert the expression for $\vec{j}_\parallel$ into the vorticity equation (2.78) we have one equation for the unknown potential and density. In order to close the system we use the continuity equation (2.63) for electrons. It can be written as

$$\mathrm{d_t}(\bar{n} + \tilde{n}) = \nabla_\parallel \frac{\tilde{j}_\parallel}{e} \tag{2.81}$$

and we differentiate between the mean profile $\bar{n}(x)$ and $n_0 = \bar{n}(x_0)$. The latter is the density at x_0 and it is $n = \bar{n} + \tilde{n}$. Inserting (2.80) into (2.78) and (2.81) we obtain the system

$$\mathrm{d_t}(\bar{n} + \tilde{n}) = \frac{1}{m_e \nu} \nabla_\parallel^2 (\tilde{p}_e - e n_0 \tilde{\phi}) \tag{2.82}$$

$$\frac{m_i n_0}{B^2} \, \mathrm{d_t} \, \nabla_\perp^2 \tilde{\phi} = \frac{e}{m_e \nu} \nabla_\parallel^2 (\tilde{p}_e - e n_0 \tilde{\phi}) \,. \tag{2.83}$$

The parallel current couples density/pressure and potential perturbations via (2.80) and (2.81)due to the resistivity. It highlights the role of collisions to establish a non-adiabatic electron response, which acts on the perpendicular dynamics of the drift wave. The current is balanced by the polarization drift of the ions to ensure quasi neutrality (vorticity equation (2.78)).

In order to simplify the system of equations we normalize the quantities as follows

$$\hat{\phi} = \frac{e\tilde{\phi}}{T_e}; \quad \hat{n} = \frac{\tilde{n}}{n_0}; \quad \hat{p} = \frac{\tilde{p}}{n_0 T_e}; \quad \hat{\nabla} = \rho_s \nabla; \quad \kappa_n = \frac{\rho_s}{L_n}; \quad \hat{t} = t \frac{c_s}{\rho_s} \tag{2.84}$$

with $c_s = \sqrt{T_e / m_i}$ being the ion speed of sound. After some algebra the set of equations can be written as [12]

$$\hat{\mathrm{d}}_\mathrm{t} \left(\frac{\bar{n}}{n_0} + \hat{n} \right) = \hat{\nabla}_\parallel^2 (\hat{n} - \hat{\phi}) / \hat{\nu} \tag{2.85}$$

$$\hat{\mathrm{d}}_\mathrm{t} \hat{\Omega} = \hat{\nabla}_\parallel^2 (\hat{n} - \hat{\phi}) / \hat{\nu} \tag{2.86}$$

where we used the collisionality $\hat{\nu} = \nu/\omega_{\mathrm{ce}}$ and the normalized vorticity $\hat{\Omega} = \hat{\nabla}_\perp^2 \hat{\phi}$ (c.f. (2.79)). These equations are known as the *Hasegawa-Wakatani equations*. We introduce the Poisson-bracket notation

$$\{\hat{\phi}, \hat{n}\} \coloneqq \hat{\partial}_x \hat{\phi} \hat{\partial}_y \hat{n} - \hat{\partial}_y \hat{\phi} \hat{\partial}_x \hat{n} \tag{2.87}$$

which yields a more compact form of the Hasegawa-Wakatani equations

$$\hat{\partial}_n \hat{n} + \{\hat{\phi}, \hat{n}\} + \kappa_n \hat{\partial}_y \hat{\phi} = \hat{\nabla}_\parallel^2 \left(\hat{n} - \hat{\phi}\right)/\hat{\nu} \tag{2.88}$$

$$\hat{\partial}_t \hat{\Omega} + \{\hat{\phi}, \hat{\Omega}\} = \hat{\nabla}_\parallel^2 \left(\hat{n} - \hat{\phi}\right)/\hat{\nu} \tag{2.89}$$

The Hasegawa-Wakatani equations are a simple model for three dimensional, linearly unstable drift wave turbulence. The turbulence is caused by the non-linearities in the Poisson-brackets and is driven by the density gradient in the term with κ_n. The strong anisotropy introduced through the magnetic field motivates to approximate the parallel gradients in (2.88) and (2.89) through a constant given by

$$\hat{\nabla}_\parallel \approx (k_\parallel \rho_s)^2 = \hat{k}_\parallel \tag{2.90}$$

which yields with $C \coloneqq \hat{k}_\parallel/\hat{\nu}$ the *two dimensional Hasegawa-Wakatani* equations

$$\hat{\partial}_t \hat{n} + \{\hat{\phi}, \hat{n}\} + \kappa_n \hat{\partial}_y \hat{\phi} = C\left(\hat{n} - \hat{\phi}\right)/\hat{\nu} \tag{2.91}$$

$$\hat{\partial}_t \hat{\Omega} + \{\hat{\phi}, \hat{\Omega}\} = C\left(\hat{n} - \hat{\phi}\right)/\hat{\nu} \tag{2.92}$$

In order to find the linear dispersion relation we neglect the non-linearities in the Poisson brackets in (2.91) and (2.92) and transform in Fourier space [12]

$$-i\hat{\omega}\hat{n} + i\kappa_n \hat{k}_\perp \hat{\phi} = C\left(\hat{\phi} - \hat{n}\right) \tag{2.93}$$

$$i\hat{\omega}\hat{k}_\perp^2 \hat{\phi} = C\left(\hat{\phi} - \hat{n}\right) \tag{2.94}$$

Solving the second equation for $\hat{n}$ and inserting in the first yields

$$\hat{\omega}^2 \hat{k}_\perp^2 + i\hat{\omega} C\left(1 + \hat{k}_\perp^2\right) - iC\kappa_n \hat{k}_\perp = 0 \tag{2.95}$$

In the limit $C \gg \hat{\omega}$, which is the case for low collisonality, we find with $\hat{\omega} = \omega_{\mathrm{re}} + i\gamma$ for the real part

$$\omega_{\mathrm{re}} = \frac{\omega^*}{1 + \hat{k}_\perp^2} \tag{2.96}$$

and for the growth rate

$$\gamma = \frac{\omega^{*2}\hat{k}_\perp^2}{C(1+\hat{k}_\perp^2)} \tag{2.97}$$

where ω^* is the electron diamagnetic drift frequency

$$\omega^* = \kappa_n k_\perp = \frac{T_e}{eB}\frac{k_y}{L_n}\,. \tag{2.98}$$

From (2.97) it becomes clear, that a finite density gradient is necessary to drive the instability. Furthermore, collisions destabilize. In the collisionless limit $\nu \to 0 \Rightarrow C \to \infty$ or for small frequencies $\hat{\omega}$ the linear term in $\hat{\omega}$ in (2.95) dominates and we find $\hat{\omega} = \omega_{\mathrm{re}}$ and $\gamma = 0$, hence the wave is stable. Numerical simulations based on the Hasegawa-Wakatani model show for large wave numbers a scaling of the energy spectrum like $E_k \propto k^{-3}$ as expected for two dimensional turbulence [33].

In the collisionless limit the equations (2.91) and (2.92) can be further simplified. In this case it is $\hat{n} = \hat{\phi}$ and $\{\hat{\phi}, \hat{n}\} = 0$ and combining (2.91) and (2.92) yields the *Hasegawa-Mima* equation [12, 34]

$$\hat{\partial}_t\left(1 - \hat{\nabla}_\perp^2\right)\hat{\phi} + \kappa_n\hat{\partial}_y\hat{\phi} = \{\hat{\phi}, \hat{\nabla}_\perp^2\hat{\phi}\}\,. \tag{2.99}$$

It has a similar structure as Rossby waves in neutral fluids and shares many properties [35–37]. However, as it is expected for an adiabatic electron response, it is linearly stable.

2.3.4 Ion Temperature Gradient Driven Turbulence

In the foregoing section drift wave turbulence driven by a density gradient and destabilized by finite parallel resistivity was discussed. However, temperature gradients can cause instabilities too. These type of instabilities belong to the group of reactive instabilities which are unstable even without dissipative effects [38]. Their scale is in between the large MHD modes and the smaller scale of usual drift waves. Fusion devices have to be stable against ideal MHD modes, which gives the reactive drift modes a certain relevance since they are the second most dangerous class of modes and possible candidates for explaining the observed transport [38].

In the case of ion temperature gradient (ITG) driven turbulence the instability arises from the heat convection of hot ions in the presence of an ion temperature gradient. In order to illustrate this, we consider a simplified model of the so called slab-ITG i.e. the magnetic field is homogeneous and for simplicity it is $\vec{B} = B\vec{e}_z$ [39]. Now there is an ion temperature gradient $\nabla T_i = \mathrm{d}T_i/\mathrm{d}x\vec{e}_x \neq 0$ along the x-direction but no background density gradient $\nabla N_0 = 0$. We use for the parallel ion dynamics (2.63) and (2.64), but add the the energy equation for the description of the heat convection in the $E\times B$-flow

$$\frac{\partial}{\partial t}(n_i T_i) + \nabla \cdot (n_i T_i \vec{u}_{E\times B}) = 0\,. \tag{2.100}$$

We consider electrostatic fluctuations $\vec{E} = -\nabla\phi$ with small amplitude and $\omega \ll \omega_{\mathrm{ci}}$. By linearising (2.63), (2.64) and 2.100) a reduced set of equations can be written as

$$\frac{\partial \tilde{n}_i}{\partial t} + n_0 \nabla_\parallel u_{\parallel,i} = 0 \tag{2.101}$$

$$m_i \frac{\partial u_{\parallel,i}}{\partial t} = -e\nabla_\parallel \phi - \nabla_\parallel \tilde{T}_i \tag{2.102}$$

$$\frac{\partial \tilde{T}_i}{\partial t} + \vec{u}_{E\times B} \cdot \nabla T_i = 0 \tag{2.103}$$

$$\tilde{n}_i = \tilde{n}_e = n_0 \frac{e\tilde{\phi}}{T_e}\,. \tag{2.104}$$

The last equality comes from the quasi-neutrality condition and the Boltzman relation (2.72). We Fourier transform in time, solve (2.103) for $\tilde{T}_i$, insert the result into (2.102) which we then solve for u_i and insert into (2.101). With the Boltzman relation we find after some algebra a dispersion relation

$$1 - \left(\frac{c_s k_z}{\omega}\right)^2 \left(1 - \frac{\omega_{T_i}}{\omega}\right) = 0 \quad \text{with} \quad \omega_{T_i} = \frac{k_y}{eB}\frac{\mathrm{d}T_i}{\mathrm{d}x} \tag{2.105}$$

and $c_s = \sqrt{T_e/m_i}$. In the case $0 < \omega \ll \omega_{T_i}$ we find

$$\omega^3 + c_s^2 k_z^2 \omega_{T_i} = 0 \tag{2.106}$$

and with $\omega = \omega_{\mathrm{re}} + i\gamma$ the solution reads

$$\omega_{\mathrm{re}} = \frac{1}{2}(\omega_{T_i} c_s^2 k_z^2)^{1/3} \tag{2.107}$$

$$\gamma = \frac{\sqrt{3}}{2}(\omega_{T_i} c_s^2 k_z^2)^{1/3} \propto \left(\frac{\mathrm{d}T_i}{\mathrm{d}x}\right)^{1/3}\,. \tag{2.108}$$

Thus we see, that indeed the ion temperature gradient can destabilizes the mode. A more rigorous treatment allowing for a finite density gradient yields for the dispersion relation [38]

$$\omega^3 + \eta_i \omega_{*i} c_s^2 k_\parallel^2 = 0 \tag{2.109}$$

where $\eta_i = L_n/L_{T_i}$, $L_x = -(x/\nabla x)$ with $x = n, T_i$ and $\omega_{*i} = \vec{k}\cdot\vec{u}_{\mathrm{dia,i}}$. The slab ITG mode was discovered in the 1960's [40]. In general the magnetic drifts cannot be neglected in magnetically confined fusion plasmas like tokmakas [38].An advanced fluid model which takes the magentic drift into account can be found in [38]. With $\omega = \omega_{\mathrm{re}} + i\gamma$ it can be written as

$$\omega_{\mathrm{re}} = \frac{1}{2}\omega_{*e}\left[1 - \left(1 + \frac{10}{3\tau}\right)\varepsilon_n - k^2\rho_s^2\left(1 + \frac{1+\eta_i}{\tau} - \varepsilon_n - \frac{5}{3\tau}\varepsilon_n\right)\right] \tag{2.110}$$

and

$$\gamma = \frac{\omega_{*e}\sqrt{\varepsilon_n/\tau}}{1 + k^2\rho_s^2}\sqrt{\eta_i - \eta_{ith}} \tag{2.111}$$

where $\omega_{*e} = \vec{k}\cdot\vec{u}_{\mathrm{dia,e}}$ is the diamagnetic drift frequency of the electrons, $\tau = T_e/T_i$ the electron to ion temperature ratio and $\varepsilon_n = \omega_D/\omega_*$ the ratio of the magnetic drift to diamagnetic drift frequency. The ITG mode is destabilized if $\eta_i > \eta_{ith}$ where the threshold is given by [38]

$$\begin{aligned}\eta_{ith} = {} & \frac{2}{3} - \frac{\tau}{2} + \varepsilon_n\left(\frac{\tau}{4} + \frac{10}{9\tau}\right) + \frac{\tau}{4\varepsilon_n} - \frac{k^2\rho_s^2}{2\varepsilon_n} \\ & \times\left[\frac{5}{3} - \frac{\tau}{4} + \frac{\tau}{4\varepsilon_n} - \left(\frac{10}{3} + \frac{\tau}{4} - \frac{10}{9\tau}\right)\varepsilon_n + \left(\frac{5}{3} + \frac{\tau}{4} - \frac{10}{9\tau}\right)\varepsilon_n^2\right].\end{aligned} \tag{2.112}$$

From (2.111) we see, that curvature ($\omega_D \propto \kappa$) and inhomogeneities of the magnetic field ($\omega_D \propto \nabla B$) increase the growth rate as well as a reduction of the temperature ratio.

2.3.5 Electron Temperature Gradient Driven Turbulence

Similar to the ion temperature gradient, an electron temperature gradient (ETG) can destabilize the plasma too [38]. The typical spatial scale of ETG turbulence is much smaller $\rho_{L,e} \ll \lambda_{\mathrm{ETG}} \ll \rho_{L,i}$ compared to ITG turbulence.

The ions reach thermal equilibrium by perpendicular motion, which relaxes the upper frequency limit $\omega \ll \omega_{ce}$. In this small scale high frequency regime the ions are unmagnetized and it may be possible to ignore electron parallel motion. It turns out, that the electrons and ions are switched compared to the ITG mode. However, whereas the ITG mode propagates in the ion diagmagnetic drift direction, the ETG mode propagate in the electron diagmagentic drift direction. Since the spatial scales are much smaller, the direct transport of ETG turbulence is little. However, through mode coupling larger modes can be excited which have an increased transport.

2.3.6 Trapped Particle Instability

Beside gradients in temperature and density, also trapped particles can lead to an instability. We consider again tokamak geometry. As already mentioned in (2.2.4) particles which move along the magnetic field lines experience a gradient in the magnetic field strength because the magnetic field is stronger on the inboard than on the outboard side and the twist of the field lines allows the particles to reach both regions. If the parallel velocity is small enough particles are trapped. To be more precise the condition for trapping reads [38]

$$v_{\parallel} < \sqrt{2}\varepsilon v_{\perp}\,, \tag{2.113}$$

where v indicates the single particle velocity and $\varepsilon = r/R < 1$.On the one hand the trapping can impede the parallel electron response on space charges, on the other hand it changes the effective collision frequency. Normally, the collision frequency is defined for a rate under which particles are deflected by 90° (in reality they undergo many small angle collision which are more likely than a large angle deflection). However, already small angle collisions can lead to a detrapping of particles which yields the effective collision frequency $\nu_{\text{eff}} = \nu/\varepsilon$. Furthermore, the trapping of particles deforms the particle distribution function $f(\vec{r}, \vec{v})$ in phase space which measures the probability density to find a particle at location $\vec{r}$ with velocity $\vec{v}$, which requires a kinetic description. In the foregoing sections the plasma was described as fluid, where the implicit assumption was made, that the particle distributions functions is a Maxwellian and we considered only the averaged motion over all particles. We need to relax this restriction and consider particle distribution function which must not be necessarily a Maxwellian. However, we consider again the process for which $\omega \ll \omega_{ci}$, hence the gyro frequency of the ions and electrons

is much faster than any time scale and we average over the gyro motion. In the case in which the bounce frequency of the ions is small i.e. $\omega_{bi} \ll \omega$, a dispersion relation for the trapped electron instability can be found [38]

$$\omega \approx \omega_{*e}\left(1 - \frac{k_\theta^2\rho_s^2 - k_\parallel^2 c_s^2/\omega_{*e}^2}{1-\sqrt{\varepsilon}}\right) + i\frac{\nu_{\text{eff}}\sqrt{\varepsilon}}{\omega_{*e}(1-\sqrt{\varepsilon})}(\omega - \omega_{*e}) \tag{2.114}$$

and with $\omega = \omega_{\text{re}} + i\gamma$ in the limit $\gamma \ll \omega_{\text{re}}$ we find for the growth rate

$$\gamma = \frac{\nu_{eff}\sqrt{\varepsilon}}{(1-\sqrt{\varepsilon})^2}\left(k_\theta^2\rho_s^2 - \frac{k_\parallel^2 c_s^2}{\omega_{*e}}\right). \tag{2.115}$$

The effect of trapping manifests thus in the effective collision frequency and an increase of the growth rate by a factor $\sqrt{\varepsilon}/(1-\sqrt{\varepsilon})^2$ for increased trapped particle fraction. Similarly, trapped ions can lead to an instability if $\omega_{bi} > \omega$ [38]. Furthermore, the presence of an electron temperature gradient can destabilize trapped electron modes [38, 41].

2.4 Turbulence in Tokamaks

Although turbulence in tokamaks has been extensively studied, there is no comprehensive theoretical description yet. As for the turbulence in neutral fluids the non-nonlinear property of the underlying physics model, the coupling of multiple scales, several turbulence drives, non-linear self-regulation and a dependence on the ambient magnetic field and the plasma composition exacerbates extremely its investigation [42]. This section provides a short summary of the most important findings of turbulence in tokamaks. An overview provides e.g. the ITER physics basis about "Plasma confinement and transport" [42]. Typically, the measured energy transport rates exceed those predicted by the classical and neoclassical theory. The remaining transport has traditionally been named anomalous transport, but from theoretical and experimental investigations it become clear that it is caused by turbulent fluctuations. [42].

Figure 2.12 gives an overview of spatial drift wave turbulence scales, turbulence mechanisms, affected transport channels and stabilization mechanisms. As we have seen in Sec. 2.3.4 ITG turbulence is destabilized if the ion temperature gradient exceeds a critical value. Above this critical value

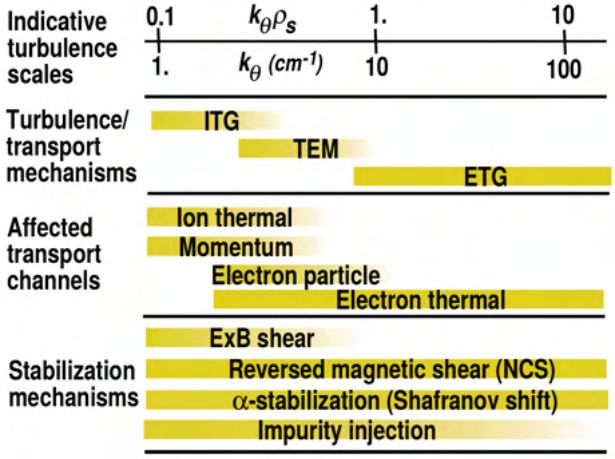

Figure 2.12: Overview of drift wave turbulence scales, turbulence mechanisms, affected transport channels and stabilization mechanisms. The angle θ indicates the poloidal direction. Taken from [43].

the ion thermal transport reaches quickly a value of $\chi_i \sim \rho_i^2 v_{ti}/L_{Ti}$ and stays at this level (with ρ_i being the ion gyro radius and v_{ti} the ion thermal velocity) [42]. This finding is linked to the effect of *profile stiffness*: for typical plasma conditions and moderate ion heating the temperature gradient increases only marginal above the critical value [42]. This observations has been made in various devices (e.g. ASDEX-Upgrade [44,45] or JT-60U [46]). If an instability exists its growth is limited by some kind of saturation mechanism. Self generated zonal $E{\times}B$-flows lead to a shearing of turbulent eddies and present the dominant non-linear saturation mechanism for ITG turbulence (see e.g. [47–54] as denoted in [42]). In some cases it can shift the critical ion temperature gradient [55]. Another large scale structure stabilizing turbulence are *zonal flows* [48,56]. These are non-linearly self generated by the turbulent fluctuations with vanishing poloidal mode number ($k_\theta \approx 0$) and can back react on the turbulence presenting a self regulation mechanism of transport. Large scale simulations of ITG show the formation flows and a reduction of turbulent ion heat flux [42]. The transport reduction depends on the turbulent fluctuation amplitude reduction and the randomization of the coherent structures [42]. Sheared $E \times B$-flows are closely connected to *transport barriers*, small radially extended regions in which the turbulent transport is reduced. The most important transport barrier was observed when the *H-mode* regime of plasma operation was discovered at the ASDEX tokamak [57]. In this regime temperature and density profiles were steep-

ened at the edge forming a *pedestal* [58], the energy confinement time was increased by a factor of two [57] and turbulent fluctuations were reduced [59]. The increased (high) confinement is eponymous for the H-mode, in contrast to the low-confinement *L-mode* plasma regime without transport barrier. Although the H-mode was already discovered in 1982 the exact mechanisms still presents an open research question [60]. The transport barrier accompanying the H-mode regime is located at the edge and therefore also attributed as *edge transport barrier* (ETB) in contrast to *internal transport barriers* (ITB) which have been found later on [61]. Trapped electrons can either destabilize ITG or lead to the intermediate spatial scale TEM turbulence. TEM turbulence is one of the main mechanisms for particle transport [42]. Furthermore trapped electrons can lead to a high turbulent heat flux if either ITG or TEM is unstable [42].

While turbulent transport on the ion scale can be reduced down to the neoclassical limit in ITBs, the electron thermal transport is not much affected. A plausible candidate for the transport below the ion scales is ETG turbulence [42]. From a simple mixing length ansatz the transport of ETG turbulence should be small compared to ITG or TEM turbulence due to its smaller spatial scales. However, simulations have shown the formation of *streamer*, radially extended structures ($k_{\text{radial}} \approx 0$) which can cause transport more than one order of magnitude above the mixing length estimate [62–64].

2.5 Turbulence in Wendelstein 7-X

The field of turbulence research in stellarator geometry is relatively young compared to tokamaks. The optimization of neoclassical transport in Wendelstein 7-X raises the question about the role of turbulence and how it compares to tokamaks. Although there are no experimental investigations so far, there has been an increasing number of theoretical publications over the last two decades. The full three dimensional geometry of a stellarator exacerbates the numerical investigation and appropriate simplifications have to be applied. To give an example, roughly half a million CPU hours are needed for a well resolved microturbulence simulation in flux-tube geometry and kinetic electrons [65]. State of the art gyrokinetic simulations codes, such as the continuous GENE code for non-linear ITG turbulence operates in flux tube or flux surface geometry limited to a fixed radial position [66]. The particle in cell code EUTERPE provides a global gyrokinetic treatment,

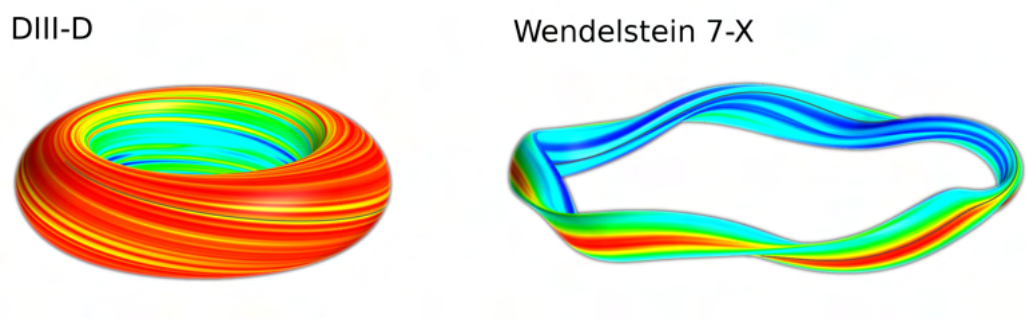

Figure 2.13: GENE simulation of ITG turbulence in tokamak (left) and stellarator (right) geometry. Red colors indicate strong fluctuations, blue colors weak. Courtesy of P. Xanthopoulos.

however it is limited to linear ITG modes [67,68]. The most important electrostatic microinstabilities in tokamaks, the ITG and the TEM mode, are predicted to occur in stelllarators too. However, their appearance is different [69–75]. One of the most obvious differences is the spatial distribution of turbulent fluctuations. In a tokamak, turbulent fluctuations peak over the whole outboard side of the torus where the curvature is unfavourable (c.f. Fig. 2.13). Whereas in a stellarator the unfavourable curvature and, thus, the fluctuations are much more poloidaly localised in a narrow band along the magnetic field lines [71, 76, 77]. Furthermore, the range of fluctuation amplitudes in stellarators seem to be greater [77]. For similar values of the temperature gradient, the growth rates of ITG modes in Wendelstein 7-X seem to be comparable to those of a tokamak [77]. The difference can be even further reduced, if the connection length between regions of good and bad curvature is chosen to be similar in the tokamak [74,77]. If the local curvature radius is similar, the local curvature driven ITG branch is the same for tokamaks and stellarators [71]. However, the parallel connection length between regions with different magnetic properties is significantly shorter in Wendelstein 7-X than in a typical tokamak, which acts stabilizing on the toroidal branch [77]. In a tokamak the parallel connection length is in the order of qR, with $q = 1/\iota$ being the safety factor and R the major radius, whilst in a stellarator it is rather a field period, which is much less [71]. Therefore, ITG modes are expected to be more slab like and less curvature driven, which is confirmed by numerical and analytical investigations [71,74]. First indications exist, that the corresponding turbulent transport in Wendelstein 7-X is lower than in a typical tokamak [77]. However, this need to be further assessed in studies of saturated turbulence [77].

A significant difference between stellarators emerges from analytical and numerical investigations of TEM turbulence [71–73, 77, 78]. These kind of modes are excited by trapped electrons in regions of bad curvature.In a tokamak, trapped particles reside in places where the curvature is unfavourable, namely on the outboard side of the torus, whereas in a stellarator they can be located at different places. Perfectly quasi-isodynamic stellarators [79] are so called maximum-J devices i.e. $\partial J/\partial\psi < 0$, where J is the parallel adiabatic invariant and ψ the toroidal flux [71]. It has been shown, that in maximum-J configurations the bounce averaged curvature is favourable [71, 78]. In these configurations the poloidal direction in which the electrons precess is opposite to the direction of the drift wave propagation, which prevents a resonant interaction. Exact quasi-isodynamicity is impossible to reach [71, 80]. However, Wendelstein 7-X is the first stellarator which approaches quasi-isodynamicity for high plasma β (β is the normalised plasma pressure) [71]. Plunk et al. found the analytical expression $\omega = -(Q \pm \sqrt{Q^2 - 4PR})/(2P)$ for the angular frequency arising from a trapped particle instabilities in stellarator geometry, which propagates in the ion diamagnetic drift direction and has a wavelength comparable to the ion gyroradius [75]. This instability, arising from the ions, is named ion-driven trapped electron mode (ITEM) [75]. The important observation is at this point, that a positive R can lead to a destabilization as it shifts the radicand towards negative values (P is positive definite). It can be written as [75]

$$R = \underbrace{\frac{\omega_{*i}T_e}{T_i}\int_{-\infty}^{\infty}\hat{\omega}_{di}F(b,\eta_i)|\Phi|^2\frac{\mathrm{d}l}{B}}_{\text{ion contribution}} + \underbrace{\frac{3(1+\eta_e)\omega_{*e}}{4}\int_{1/B_{\max}}^{1/B_{\min}}\sum_j \tilde{\omega}_{dej}\tau_j|\Phi|^2\mathrm{d}\lambda}_{\text{electron contribution}}$$

where ω_{*s} is the diamagnetic drift frequency for ions ($s = i$) and electrons ($s = e$), T_s the temperature, η_s the usual normalized temperature gradient, $\hat{\omega}_{di}$ the magnetic drift frequency of the ions, $\tilde{\omega}_{dej}$ the magnetic drift frequency of the electrons in the j-th magnetic well and $F(b, \eta_i)$ is a positive function for all b if $\eta_i > 0$ (F is the expression in square brackets in (3.5) in [75]). For a more detailed description the interested reader is referred to [75]. The first summand represents the ion contribution and is destabilizing if $\omega_{*i}\hat{\omega}_{di} > 0$ which is the criterion for bad curvature. The second term, having products of $\omega_{*e}\tilde{\omega}_{dej}$ describes the bounce averaged electron contribution and is negative in maximum-J devices. Thus, there is a *stabilizing* contribution from the electrons. This holds true for any $\eta_e > 0$ as long as the phase velocity of the instability is between the ion- and electron thermal velocities $v_{Ti} \ll \omega/k_\parallel \ll v_{Te}$ (no Landau damping) and the magnetic drift frequencies are smaller than the diamagnetic frequency (decouples ITG and TEM instability) [75].

Therefore, an increase of the electron temperature gradient stabilizes since the electron term is proportional to η_e. Furthermore, the mode does not necessarily peak in regions of bad curvature [75]. In some cases it might be even completely stabilized by favourable averaging of the ion magnetic drift [75].

As discussed above, instabilities on the ion scale are expected to play an important role in Wendelstein 7-X. Although their appearance is different, the fundamental physics mechanisms (gradient driven, destabilization through curvature, trapped particles and non-adiabatic electrons) are the same. This is an important aspect as it allows to narrow down the spatiotemporal scales required to resolve for turbulence measurements in Wendelstein 7-X to be similar to those expected in tokamaks (c.f. Fig. 2.12).

Chapter 3

Phase Contrast Imaging

The principle of phase contrast imaging (PCI) is used in a wide field of applications. In this chapter we summarize the general theoretical description of the PCI diagnostics. In Sec. 3.2 it is shown that the considered plasmas act like an optically homogeneous medium with a perturbed refractive index and the problem reduces to imaging those perturbations. This can be split up into two parts: the first part, described in Sec. 3.3, explains in more detail the imaging of the refractive index perturbation and the need for shifting part of the light by $\pi/2$, to obtain a linear response between perturbation amplitude and signal. The second part, Sec. 3.4, describes how the phase shift can be obtained by methods of Fourier optics. This chapter is based on former work presented in [81].

3.1 A Brief History

Creating phase contrast is a long existing problem. The simplest way to investigate an arbitrary object with the help of light – or in general electromagnetic radiation – is to use its property to diminish the amplitude of an incoming probe beam. After passing through the object, the amplitude of the wave is modulated depending on the absorption properties of the object. The amplitude modulation contains information about the object and can be easily measured since the intensity is proportional to the square of the amplitude. Objects, that change only the amplitude of a wave are called

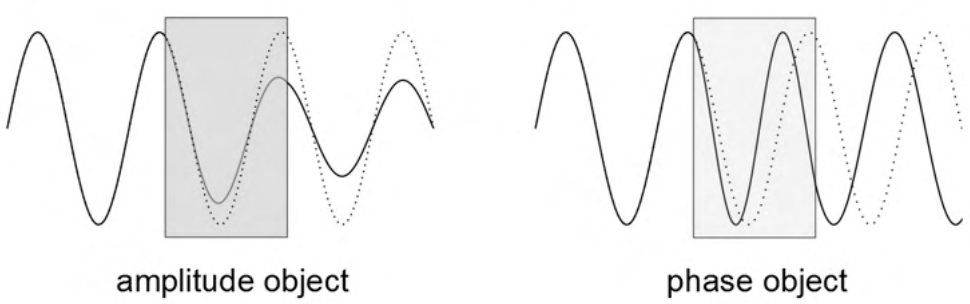

Figure 3.1: Different effects of phase and amplitude objects on electromagnetic waves. The dotted lines show the wave without the influence of the objects. The wave travels from the left to the right hand side.

amplitude objects. In contrast, *phase objects* change only the phase of the probe beam (c.f. Fig 3.1). Such objects do not alter the beam's amplitude and are invisible for direct amplitude sensitive detection mechanisms like the human eye or CCD sensors. For example, many biological tissues are phase objects, which makes them hard to examine with a bright field microscope.

The first attempts to make phase objects visible were made in the 17th century by Antoni van Leeuwenhoek, Robert Hooke and Christiaan Huygens and can be referred to the dark field microscopy and *schlieren* (German for "streak") method [82, 83]. The latter is often attributed to August Toepler who reinvented the *schlieren* method between 1859 and 1864 [82]. In the 1930s the Dutch Physicist Frits Zernike invented the phase contrast imaging method when he studied imperfections in diffraction gratings [84]. He applied this technique to microscopes which became later on important in the field of biology and medicine [85]. Zernike's invention was of such great importance that he was awarded the physics Nobel prize in 1953. Outside microscopy phase contrast imaging was less frequent. However, in the field of X-ray imaging and plasma diagnostics the same challenge of making phase objects visible had to be faced. In 1965 Bonse and Hart developed a method to measure phase shifts in X-rays [86].

Plasma density fluctuations act as phase objects and in 1967 Presby and Finkelstein published their results about *Plasma Phasography* [87], the adaption of Zernikes method to plasmas. They used a ruby-laser for illumination "to make possible the observation of macroscopic moving tenuous objects, such as jets, shock waves, and plasmas" [87] and were able to demonstrate

the superiority to the schlieren method.

For the observation of density fluctuations in magnetically confined plasmas, the phase contrast technique was first used by Weisen [88–92]. He used a 23 cm wide CO_2 Laser beam operating at 10.6 µm to study turbulence and driven Alfén waves in the TCA tokamak. Later on, this technique was applied to various experimental devices including the DIII-D tokamak [93, 94], the Heliotron-E device [95, 96], the TEXT-U tokamak [97, 98], the CDX-U tokamak [99], the Alcator C-Mod tokamak [100, 101] and the LHD stellarator [102].

3.2 The Plasma as Phase Object

When electromagnetic waves interact with matter in a classical picture, they apply a force which accelerates the charged particles and leads to emission of additional electromagnetic radiation into all directions. This process is refereed to as scattering. From the analysis of the scattered waves, various properties of the scattering object can be obtained. Diagnosing plasmas with electromagnetic waves (of sufficiently small amplitude) has the great advantage of being non invasive: the probe waves causes negligible perturbations to the plasma but can provide information about its properties, e.g., density, temperature and magnetic field [103]. We will see that for the PCI probe beam (wavelength 10.6 µm) the refractive index of the plasma depends approximately linear on its density. The plasma can be treated as an optical medium with changes in its refractive index and acts consequently as a phase object. The subsequent derivation is rather general but highlights some important aspects of the used infrared probe beam, e.g., the effective isotropy of the plasma [104].

The plasma is treated as a quasi-neutral, continuous medium described by Maxwell's equations

$$\nabla \times \vec{B} = \mu_0 \left(\vec{j} + \epsilon_0 \frac{\partial \vec{E}}{\partial t} \right) , \tag{3.1}$$

$$\nabla \times \vec{E} = -\frac{\partial \vec{B}}{\partial t} , \tag{3.2}$$

where $\vec{B}$ is the magnetic flux density, $\vec{E}$ the electric field strength and $\vec{j}$ the current density, the latter containing all plasma properties. The plasma

is assumed to be in an equilibrium state described by zero order quantities (index 0), constant in space and time. The electromagnetic probe wave is monochromatic with angular frequency ω_b and wave vector $\vec{k}_\mathrm{b}$. It causes a small perturbation of the equilibrium state, described by first order quantities (index 1), so that the overall quantities are given by the superposition of the zero and first order quantities e.g. $\vec{E} = \vec{E}_0 + \vec{E}_1 \exp[i(\vec{k}_\mathrm{b} \cdot \vec{r} - \omega_\mathrm{b} t)]$. Due to this superposition and the linearity of Maxwell's equations, equilibrium and perturbed quantities can be treated separately and we can restrict in the further analysis to the perturbed quantities. The relationship between $\vec{j}_1$ and $\vec{E}_1$ is given by Ohm's law

$$\vec{j}_1 = \underline{\sigma}\vec{E}_1 \,, \tag{3.3}$$

where $\underline{\sigma}$ is the conductivity tensor taking into account the possible anisotropy of the plasma, e.g. due to a background magnetic field. The magnetic flux density can be eliminated by taking $\partial/\partial t$ of eq. (3.1) and $\nabla\times$ of eq. (3.2)

$$\nabla \times (\nabla \times \vec{E}) + \mu_0 \frac{\partial}{\partial t}\left(\vec{j} + \epsilon_0 \frac{\partial \vec{E}}{\partial t}\right) = 0 \,. \tag{3.4}$$

Using (3.3) and Fourier transform, the first order quantities are given by

$$\vec{k}_\mathrm{b} \times (\vec{k}_\mathrm{b} \times \vec{E}_1) + i\omega_\mathrm{b}\mu_0(\underline{\sigma}\vec{E}_1 - i\omega_\mathrm{b}\epsilon_0\vec{E}_1) = 0 \tag{3.5}$$

$$\Leftrightarrow \vec{N} \times \left(\vec{N} \times \vec{E}_1\right) + \underline{\epsilon}\vec{E}_1 = 0 \,, \tag{3.6}$$

where in the last step the definition of the speed of light $c = 1/\sqrt{\epsilon_0\mu_0}$, the refractive index vector $\vec{N}$ and the dielectric tensor $\underline{\epsilon}$ were used:

$$\vec{N} = \frac{c}{\omega_\mathrm{b}}\vec{k}_\mathrm{b} \,, \tag{3.7}$$

$$\underline{\epsilon} = \mathbb{1} + \frac{i}{\omega_\mathrm{b}\epsilon_0}\underline{\sigma} \,. \tag{3.8}$$

Equation (3.6) gives a relation between the wave properties $\vec{E}_1$, $\vec{k}_\mathrm{b}$ and ω_b and the plasma properties described by $\underline{\epsilon}$ respectively $\underline{\sigma}$. To get a detailed description of $\underline{\epsilon}$ it is necessary to investigate the response of a plasma to an incident electromagnetic wave. Treating the plasma as cold and ignoring collisions the change in the momentum of species s is determined by the Lorentz force and an expression for the cold plasma dielectric tensor can be found [104]

$$\underline{\epsilon} = \begin{pmatrix} S & -iD & 0 \\ iD & S & 0 \\ 0 & 0 & P \end{pmatrix} \tag{3.9}$$

where the annotation according to Stix was used [104]:

$$P = 1 - \sum_s \frac{\omega_{\mathrm{p}s}^2}{\omega_{\mathrm{b}}^2}\,, \tag{3.10}$$

$$S = \frac{1}{2}(R+L) = 1 - \sum_s \frac{\omega_{\mathrm{p}s}^2}{\omega_{\mathrm{b}}^2 - \omega_{cs}^2}\,, \tag{3.11}$$

$$D = \frac{1}{2}(R-L) = \sum_s \frac{\mathrm{sgn}(q_s)\omega_{\mathrm{p}s}^2\omega_{cs}}{\omega_{\mathrm{b}}(\omega_{\mathrm{b}}^2 - \omega_{cs}^2)}\,, \tag{3.12}$$

$$R = S + D = 1 - \sum_s \frac{\omega_{\mathrm{p}s}^2}{\omega_{\mathrm{b}}(\omega_{\mathrm{b}} + \mathrm{sgn}(q_s)\omega_{cs})}\,, \tag{3.13}$$

$$L = S - D = 1 - \sum_s \frac{\omega_{\mathrm{p}s}^2}{\omega_{\mathrm{b}}(\omega_{\mathrm{b}} - \mathrm{sgn}(q_s)\omega_{cs})}\,, \tag{3.14}$$

where $\omega_{\mathrm{p}s} = \sqrt{n_s q_s^2/(\epsilon_0 m_s)}$ denotes the plasma frequency of species s, q_s its charge, m_s its mass, n_s is the density, $\omega_{cs} = |q_s|B_0/m_s$ is the cyclotron frequency and $\mathrm{sgn}(q_s) = q_s/|q_s|$ the signum function. The magnetic field $\vec{B_0} = B_0\vec{e}_z$ is set along the z-axis. Without loss of generality we define the refractive index vector (3.7) as lying in the xz-plane, where γ denotes the angle between the z-axis and $\vec{N}$

$$\vec{N} = \begin{pmatrix} N\sin(\gamma) \\ 0 \\ N\cos(\gamma) \end{pmatrix}\,, \qquad N = c\frac{k_{\mathrm{b}}}{\omega_{\mathrm{b}}}\,. \tag{3.15}$$

This definition and the dielectric tensor (3.9) allows one to rewrite (3.6) as

$$\begin{pmatrix} S - N^2\cos^2(\gamma) & -iD & N^2\sin(\gamma)\cos(\gamma) \\ iD & S - N^2 & 0 \\ N^2\sin(\gamma)\cos(\gamma) & 0 & P - N^2\sin^2(\gamma) \end{pmatrix} \begin{pmatrix} E_{1x} \\ E_{1y} \\ E_{1z} \end{pmatrix} = 0\,. \tag{3.16}$$

In order to find non-trivial solutions, the determinant of the coefficient matrix must be zero which leads to the following expression

$$AN^4 - BN^2 + C = 0 \quad \Rightarrow \quad N^2 = \frac{B \pm F}{2A} \tag{3.17}$$

where

$$A = S\sin^2(\gamma) + P\cos^2(\gamma)\,, \tag{3.18}$$

$$B = RL\sin^2(\gamma) + PS(1+\cos^2(\gamma))\,, \tag{3.19}$$

$$C = PRL\,, \tag{3.20}$$

$$F = \sqrt{(RL - PS)^2\sin^4(\gamma) + 4P^2D^2\cos^2(\gamma)}\,. \tag{3.21}$$

The identity $S^2 - D^2 = RL$ was used [104]. Equation (3.17) determines N as a function of the angular frequency ω_b, the wave number k_b and the plasma parameter ω_{ps} and ω_{cs}. The probe beam for the PCI diagnostic has a vacuum wavelength of $\lambda_\mathrm{b} = 10.6\,\mu\mathrm{m}$ which corresponds to a frequency of $\omega_\mathrm{b} = 2\pi c/\lambda_\mathrm{b} = 2 \times 10^{14}\,\mathrm{s}^{-1}$. Assuming an extremely high magnetic field of 10 T leads to an electron cyclotron frequency $\omega_\mathrm{ce} = 2 \times 10^{12}\,\mathrm{s}^{-1}$. Due to the mass ratio of $m_p \approx 1836 m_\mathrm{e}$, where m_p denotes the proton mass, the ion contribution is much smaller: $\omega_\mathrm{ci}/\omega_\mathrm{ce} = z m_\mathrm{e}/m_\mathrm{i}$. With $z = |q_\mathrm{i}|/e$ denoting the charge number of the ions. We can find an upper limit for the ion cyclotron angular frequency as following where $n_\mathrm{p} \leq z$ denotes the number of protons, n_n the number of neutrons and m_n is the neutron mass

$$\frac{\omega_\mathrm{ci}}{\omega_\mathrm{ce}} = z\frac{m_\mathrm{e}}{m_\mathrm{i}} = z\frac{m_\mathrm{e}}{n_\mathrm{p}m_\mathrm{p} + n_\mathrm{n}m_\mathrm{n}} < \frac{z}{n_\mathrm{p} + n_\mathrm{n}}\frac{m_\mathrm{e}}{m_\mathrm{p}} \leq \frac{z}{z + n_\mathrm{n}}\frac{m_\mathrm{e}}{m_\mathrm{p}} \leq \frac{m_\mathrm{e}}{m_\mathrm{p}} \approx \frac{1}{1836}\,. \tag{3.22}$$

The ordering is finally $\omega_\mathrm{b} \gg \omega_\mathrm{ce} \gg \omega_\mathrm{ci}$, which can be used to simplify the parameters (3.10) - (3.14):

$$P \approx R \approx L \approx S = 1 - \sum_s \frac{\omega_{ps}^2}{\omega_\mathrm{b}^2}\,, \quad D \approx 0 \tag{3.23}$$

$$\Rightarrow A \approx P\,, \quad B \approx 2P^2\,, \quad C \approx P^3\,, \quad F \approx 0 \tag{3.24}$$

$$\Rightarrow N^2 \approx P = 1 - \sum_s \frac{\omega_{ps}^2}{\omega_\mathrm{b}^2}\,. \tag{3.25}$$

Hence, the dispersion relation does not depend anymore on γ and the plasma is effectively isotropic for the probe beam. The ratio of the ion and electron plasma frequency is given by $\omega_\mathrm{pi}^2/\omega_\mathrm{pe}^2 = z^2 m_\mathrm{e} n_\mathrm{i}/(m_\mathrm{i} n_\mathrm{e})$. For a hydrogen plasma it is $z = 1$ and quasi-neutrality gives $n_\mathrm{e} \approx n_\mathrm{i}$, therefore $\omega_\mathrm{pe}^2 \gg \omega_\mathrm{pi}^2$ and N can be expressed as

$$N \approx \sqrt{1 - \frac{\omega_\mathrm{pe}^2}{\omega_\mathrm{b}^2}}\,. \tag{3.26}$$

The electron plasma frequency for an upper limit density of $n_\mathrm{e} = 1 \times 10^{21}\,\mathrm{m}^{-3}$ is $\omega_\mathrm{pe} = 2 \times 10^{12}\,\mathrm{s}^{-1} \ll \omega_\mathrm{b}$. The square root can be expanded as $\sqrt{1 - x^2} = 1 - x^2/2 + \mathcal{O}(x^4)$ and the definition for the plasma frequency can be used to obtain a linear relationship between the refractive index and the electron plasma density:

$$N \approx 1 - \frac{e^2}{2\epsilon_0 m_\mathrm{e} \omega_\mathrm{b}^2} n_\mathrm{e}\,. \tag{3.27}$$

The square root approximation, which yields $N \propto n_\mathrm{e}$, makes clear that the lower limit for ω_b is determined by the ordering $\omega_\mathrm{b} \gg \omega_\mathrm{pe}$.

The above discussion considered the unperturbed plasma as uniform in space. This is of course an idealized model and in reality there always exist spatial gradients. However, if the plasma parameters vary sufficiently slow in space, the plasma can be locally approximated as uniform in space and waves can be described as plane waves with a slowly varying wave number

$$E \propto e^{i \int \vec{k}_\mathrm{b} \cdot \mathrm{d}\vec{l} - i\omega t} \,, \tag{3.28}$$

where the line integral is along the ray path l and $\vec{k}_\mathrm{b}$ is the local solution $\vec{k}_\mathrm{b} = \vec{k}_\mathrm{b}(\omega)$ of the dispersion relation [103]. This approximation is called the WKB (after Wentzel, Kramers and Brillouin) or eikonal approximation and is a widely used concept. Inter alia it describes the transition from wave to geometrical optics and is used in the subsequent calculations. The approximation is sufficiently precise provided that the gradient length of k_b is small [103]

$$\frac{|\nabla k_\mathrm{b}|}{k_\mathrm{b}^2} \ll 1 \,. \tag{3.29}$$

From this point of view an increase of k_b would lead to more accuracy. However, in Sec. 3.4 it is shown that a small value of k_b increases the separation between zero and first order scattered beams, which allows one to detect smaller wavelength of perturbations.

To summarize, the plasma is effectively isotropic for the probe beam due to its high frequency compared to the cyclotron and plasma frequencies. Furthermore the electron contribution is dominant due to the small electron mass compared to the ions. This leads to a linear relationship between refractive index and electron density.

3.3 Measuring Phase Contrast

The light coming from a macroscopic object is basically a superposition of spherical waves emitted by the atomic scattering centres of the object. The description of image creation of an object through an optical system (e.g. lenses) by calculating their wave fields is a complete but time consuming

procedure. Geometrical optics provide a more abstract and simpler, but also more incomplete method. It can be applied when the wave character of the light can be neglected and the typical system dimensions are much greater than the wavelength of the used light. The link between the two formalisms is given by plane waves, which carry wave information (e.g. amplitude and phase) and the information of geometric light rays (directional).

The aim of an optical imaging system is the mapping of an object as exactly as possible to the image plane. Ideally this means to reconstruct the wave field at the object plane. Due to Fermat's principle, every light path between object and image plane must be equivalent. In other words, they have the same optical path length or equivalently cause the same phase change. An ideal phase object alters – by definition – only the phase of an incoming wave. Thus, the ideal image of a phase object is as well a wave field, where only the phase is modulated and the amplitude remains unchanged.

Consider the situation in Fig. 3.2: A plane wave with wave vector $\vec{k}_\mathrm{b} = k_\mathrm{b}\vec{e}_z$ encounters a single sinusoidal perturbation with wave number $\vec{k} = k\vec{e}_x$ in the refractive index $N(x', y', z)$ which is extended over a length L along the z-axis:

$$N(x', y', z) = N_0 + h(z)N_1 \cos(kx' - \varphi), \tag{3.30}$$

where N_0 is the value of the background refractive index, N_1 the amplitude of the perturbation and φ an arbitrary phase shift. The envelope function $h(z)$ is given by

$$h(z) = \begin{cases} 1\,, & z \in [-L, 0] \\ 0\,, & \text{otherwise} \end{cases} \quad . \tag{3.31}$$

In general the connection between refractive index and phase velocity c_i is $N_i = c/c_i$. Equation (3.30) is linked to the density perturbation

$$n_\mathrm{e} = n_\mathrm{e0} - h(z)n_\mathrm{e1} \cos(kx' - \varphi) \tag{3.32}$$

via (3.27) where

$$N_0 = 1 - \eta \tag{3.33}$$

$$N_1 = \eta \frac{n_\mathrm{e1}}{n_\mathrm{e0}} \quad \text{with} \quad \eta := \frac{\omega_\mathrm{pe}^2}{2\omega_\mathrm{b}^2} \tag{3.34}$$

and ω_pe is the plasma frequency of the unperturbed background. A plasma with $n_\mathrm{e0} = 1 \times 10^{20}\,\mathrm{m}^{-2}$ and a laser wavelength of 10.6 µm results in $\eta = 5 \times 10^{-6}$.

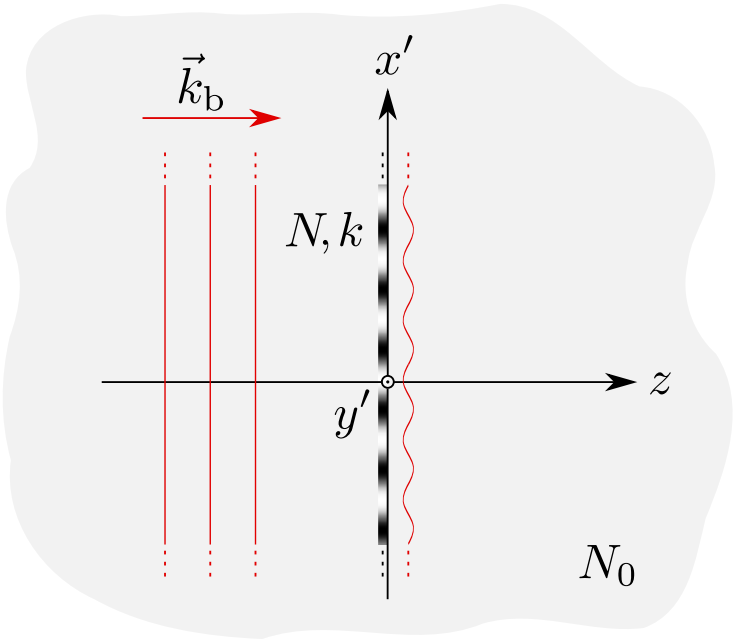

Figure 3.2: Wave field corrugation of an electromagnetic wave at a single k perturbation of the refractive index N. The perturbation has an infinite extent along the x'- and y'-axis but is infinitely small along the z-axis. The grey coloured region indicates the values of the refractive index. The phase fronts before and after passing the perturbation are shown in red. For illustration the corrugation is exaggerated.

Thus, the refractive index perturbations are very small. The minus in (3.32) occurs because of $-\cos(x) = \cos(x - \pi)$ such that density and refractive index perturbation are shifted by π. In the further analysis, only the refractive index is considered, which is of course equivalent to taking into account only the density perturbation.

After passing through the density perturbation, the phase front of the incoming plane wave is corrugated due to the fact that large values of N retard and small values of N advance the phase front.

We follow the derivation in Ref. [105] to describe the diffraction of light by high frequency sound waves. The concept is applied to the PCI diagnostic in Ref. [106]. In acousto-optics light, waves are scattered at refractive index perturbations that are caused by sound waves. Assuming homogeneity of the

medium, the following calculation uses a scalar approach.

The phase ϕ of an electromagnetic wave with wave number k_b travelling trough a medium can be calculated by performing the line integral

$$\phi = k_\mathrm{b} \int_{s_0}^{s_1} N \,\mathrm{d}s \tag{3.35}$$

along the beam path s. In this calculation the beam path is along the z-axis. Inserting (3.30) in (3.35) leads to

$$\phi = \phi_0 + \phi_1 \cos(kx' - \varphi)\,, \quad \text{where} \tag{3.36}$$

$$\phi_0 = k_\mathrm{b} \int_{z_0}^{0} N_0 \,\mathrm{d}z \quad \text{and} \quad \phi_1 = k_\mathrm{b} L N_1\,. \tag{3.37}$$

z_0 is an arbitrary reference point and L is the extent of the perturbation. It is assumed that L is small enough to treat the plasma as thin. This approximation is discussed in more detail in Sec. 3.5. Moreover the phase modulation is supposed to be small

$$|\phi_1| \ll 1\,. \tag{3.38}$$

It is now possible to describe the electric field after the perturbation as

$$E_\mathrm{obj} = E_A e^{i\phi} = E_A e^{i[\phi_0 + \phi_1 \cos(kx' - \varphi)]}\,, \tag{3.39}$$

where E_A is the amplitude. Due to the fact that the phase ϕ_1 is small, the amplitude is approximate constant for every x'. An ideal imaging system maps E_obj, apart from a phase shift, exactly to the image plane $E_\mathrm{img} = \exp(i\phi_\mathrm{sys}) E_\mathrm{obj}$, where for simplicity the magnification was set to one and the factor $\exp(i\phi_\mathrm{sys})$ describes the additional phase shift caused by the imaging system. Real imaging systems, however, are never able to reproduce the electric field exactly because it is never possible to manipulate the whole, infinitely extended electric field. Therefore real systems are always diffraction limited [107].

The electric field at the object plane can be expanded into Bessel functions J_n of the first kind of n-th order with the help of the Jacobi-Anger expansion [108]:

$$e^{i\alpha\cos(\beta)} = \sum_{n=-\infty}^{\infty} i^n \mathrm{J}_n(\alpha) e^{in\beta}\,. \tag{3.40}$$

This leads to an electric field

$$E_{\text{img}} = E_A e^{i\tilde{\phi}_0} \sum_{n=-\infty}^{\infty} i^n \mathrm{J}_n(\phi_1) e^{in(kx'-\varphi)}\,, \quad \text{where} \quad \tilde{\phi}_0 = \phi_0 + \phi_{\text{sys}}\,. \tag{3.41}$$

In the first instance this is just a mathematically equivalent representation without a deeper physical meaning. However, in Sec. 3.4.1 it will turn out that every summand for a certain n belongs to a physical light ray. Looking at the polynomial representation of the Bessel functions [109]

$$\mathrm{J}_p(x) = \sum_{k=0}^{\infty} \frac{(-1)^k}{k!\,\Gamma(p+k+1)} \left(\frac{x}{2}\right)^{2k+p} = \frac{1}{p!}\left(\frac{x}{2}\right)^p + \mathcal{O}(\phi_1^{2+p}) \tag{3.42}$$

$$\text{where} \quad |x| < \infty\,, x \notin (-\infty, 0] \quad \text{and} \quad p \in \mathbb{R}\backslash\mathbb{Z}_{<0}$$

$$\Rightarrow \mathrm{J}_0(\phi_1) = 1 + \mathcal{O}(\phi_1^2)\,, \quad \mathrm{J}_1(\phi_1) = \frac{\phi_1}{2} + \mathcal{O}(\phi_1^3)\,, \quad \mathrm{J}_{n\geq 2}(\phi_1) = \mathcal{O}(\phi_1^2)\,, \tag{3.43}$$

it becomes clear, that due to condition (3.38) every summand with $n \geq 2$ in (3.41) can be neglected and the approximations in (3.43) can be used. In reality, the intensity $I_{\text{img}} \propto |E_{\text{img}}|^2$ is measured, which make the higher orders even more unimportant. Rewriting (3.41) leads to

$$E_{\text{img}} = E_A e^{i\tilde{\phi}_0} \left(i^{-1}\mathrm{J}_{-1}(\phi_1) e^{-i(kx'-\varphi)} + \mathrm{J}_0(\phi_1) + i\mathrm{J}_1(\phi_1) e^{i(kx'-\varphi)}\right) + \mathcal{O}(\phi_1^2)\,. \tag{3.44}$$

Applying the simplifications (3.43) and the relationships [109]

$$\mathrm{J}_{-n}(x) = (-1)^n \mathrm{J}_n(x)\,\forall\, n \in \mathbb{N}_{>0}\,, |x| < \infty \quad \text{and} \quad e^{ix} + e^{-ix} = 2\cos(x) \tag{3.45}$$

E_{img} can finally be written as

$$E_{\text{img}} = E_A e^{i\tilde{\phi}_0} \left[1 + i\phi_1 \cos(kx' - \varphi)\right] + \mathcal{O}(\phi_1^2)\,. \tag{3.46}$$

Using $i = \exp(i\pi/2)$ it turns out the superposition of the $n = \pm 1$ terms are phase shifted by $\pi/2$ relative to the $n = 0$ summand. The detector measures the intensity $I_{\text{img}} \propto |E_{\text{img}}|^2$

$$I_{\text{img}} \propto 1 + \mathcal{O}(\phi_1^2)\,. \tag{3.47}$$

Thus, the resulting response is constant within the order of the approximation as we expect for a phase object. The response can be improved if the ray

belonging to $n = 0$ is phase shifted by $\pi/2$, which can be described by an additional imaginary unit i. In this case, the modified electric field at the image plane reads

$$E_{\text{img}}^{\text{PCI}} = E_A e^{i\tilde{\phi}_0} \left[i + i\phi_1 \cos(kx' - \varphi) \right] + \mathcal{O}(\phi_1^2) \tag{3.48}$$

and the intensity

$$I_{\text{img}}^{\text{PCI}} \propto 1 + 2\phi_1 \cos(kx' - \varphi) + \mathcal{O}(\phi_1^2) \tag{3.49}$$

is linear in ϕ_1. The phase shift of the $n = 0$ ray can be achieved by the use of Fourier optic methods described in sec. 3.4.

3.4 Scattering of Electro Magnetic Waves at Refractive Index Perturbations

In Sec. 3.3 we discussed the need for a $\pi/2$ phase shift of the $n = 0$ summand in (3.41). How this can be accomplished and the physical meaning of the expansion (3.41) is shown in the present section. The basic concept is Fraunhofer's and Kirchhoff's diffraction theory. A detailed description of the fundamental theoretical framework can be found in Refs. [107] and [110]. Again we follow the acousto-optics approach (Refs. [105] and [106]).

3.4.1 Scattering at a Phase Grating

We consider a similar situation as described in Sec. 3.3 (cf. Fig. 3.3): A plane wave with wave vector $\vec{k}_{\text{b}} = k_{\text{b}}\vec{e}_z$ encounters a single sinusoidal perturbation $N(x', y', z)$ with wave number $\vec{k} = k\vec{e}_x$ in the refractive index, which is infinitely small extended along the z-axis. The objective of this section is to determine the value of the electric field at the point P. According to the Fraunhofer diffraction theory (cf. also remarks in Sec. 3.3) the calculation is simplified by using a scalar approach.

Knowing the electric field at the exit of the perturbation (3.39) allows one to calculate the wave field at a chosen point P by using the Fraunhofer

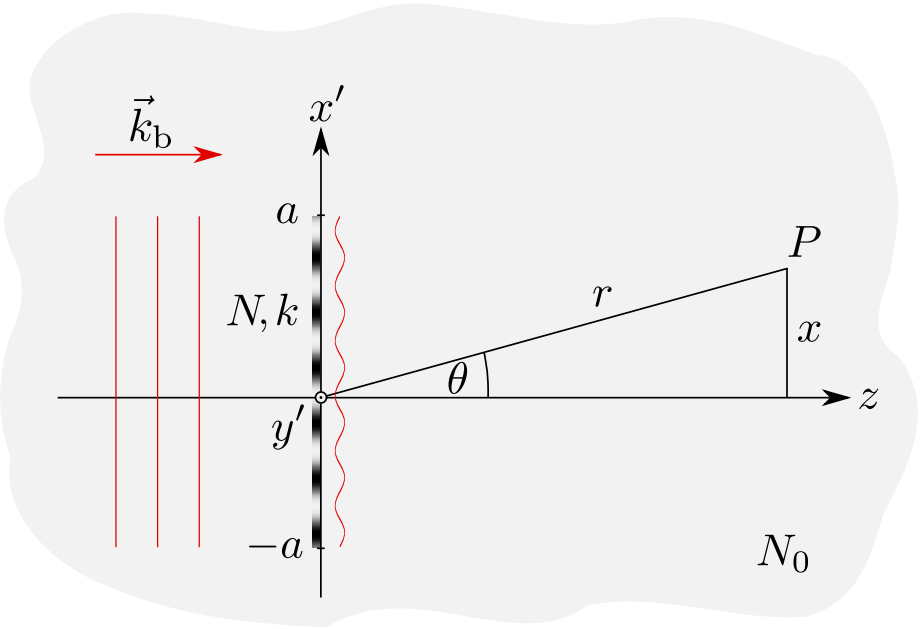

Figure 3.3: Coordinate system for calculating the scattering of an electromagnetic wave at a single k perturbation of the refractive index N. The perturbation has an infinite extent along the x'- and y'-axis, but is infinitely small along the z-axis. The grey coloured region indicates the values of the refractive index. In red colours the phase fronts are shown before and after passing the perturbation (the corrugation is exaggerated for better illustration).

diffraction formula. The Fraunhofer diffraction formula for an aperture described in Cartesian coordinates reads [107, 110]

$$A_{II}(k_x, k_y) = \int_{-\infty}^{\infty}\int_{-\infty}^{\infty} A_I(x', y') e^{-i(k_x x' + k_y y')}\,\mathrm{d}x'\mathrm{d}y'\,, \quad \text{where} \tag{3.50}$$

$$A_I(x', y') = A_0(x', y') e^{i\chi(x', y')}\,, \tag{3.51}$$

$$k_x = k_\mathrm{b}\frac{x}{r} \quad \text{and} \quad k_y = k_\mathrm{b}\frac{y}{r}\,. \tag{3.52}$$

It is the Fourier transform of the pupil function $A_I(x', y')$, where $A_0(x', y')$ describes the amplitude over the aperture and $\chi(x', y')$ the phase of the electric field with wave number k_b. The resulting field $A_{II}(k_x, k_y)$ is evaluated at a point (x, y) that is equivalent to the wave numbers k_x and k_y at distance r

from the aperture.

It is important to note that this formula is only valid if the distance r_s between source and aperture, the wavelength $\lambda_\mathrm{b} = 2\pi/k_\mathrm{b}$ and the maximum radius of the aperture r_max meet the following criteria:

$$r_s, r \gg \lambda_\mathrm{b}\,, \quad r_\mathrm{max} \ll r_s, r \quad \text{and} \quad r \gg \frac{r_\mathrm{max}^2}{\lambda_\mathrm{b}}\,. \tag{3.53}$$

To apply this to the scattering problem at the phase grating, a rectangular beam with diameter in x-direction of $2a$ and in y-direction of $2b$ is assumed for simplicity. To calculate the integral (3.50) we expand (3.39) again into Bessel functions as done in Sec. 3.3:

$$E_\mathrm{obj} = E_A e^{i\phi_0} \sum_{n=-\infty}^{\infty} i^n \mathrm{J}_n(\phi_1) e^{in(kx'-\varphi)}\,. \tag{3.54}$$

Inserting (3.54) into (3.50) yields the electric field at point P as

$$E_{II} = E_A e^{i\phi_0} \sum_{n=-\infty}^{\infty} i^n e^{-in\varphi} \mathrm{J}_n(\phi_1) \int_{-b}^{b}\int_{-a}^{a} e^{-i(k_x-nk)x'} e^{-ik_y y'}\,\mathrm{d}x'\mathrm{d}y' \tag{3.55}$$

$$= 4E_A e^{i\phi_0} \sum_{n=-\infty}^{\infty} e^{-in(\varphi-\pi/2)} \mathrm{J}_n(\phi_1) \frac{\sin(a[k_x-nk])}{k_x-nk} \frac{\sin(bk_y)}{k_y}\,. \tag{3.56}$$

The factor $\sin(bk_y)/k_y$ describes the diffraction of the beam along the y-axis and has its maximum at $k_y = 0$ respectively $y = 0$, cf. (3.52). The variation of the density along the x'-axis leads obviously only to an effect along the x-axis and the electric field variation along the y-axis remains unperturbed. The factor $\sin(a[k_x - nk])/(k_x - nk)$ covers the effect of the phase grating. The maxima are given by $k_x - nk = 0$. Using the definition (3.52) of k_x and the relationship $\sin(\theta) = x/r$ (cf. Fig. 3.3), the condition for the n-th maximum can be expressed as

$$\sin(\theta_n) = n\frac{k}{k_\mathrm{b}} \quad \text{with } n \in \mathbb{Z}\,. \tag{3.57}$$

It becomes clear that every summand in (3.56) leads to a maximum under a specific angle for a single-k sinusoidal phase grating. The amplitude of the n-th maximum in x-direction for a certain value of y is

$$E_{II,\mathrm{max}}^n := \max_x E_{II}^n \propto \lim_{k_x-nk\to 0} e^{-in(\varphi-\pi/2)} \mathrm{J}_n(\phi_1) \frac{\sin(a[k_x-nk])}{k_x-nk} \tag{3.58}$$

$$= a e^{-in(\varphi-\pi/2)} \mathrm{J}_\mathrm{n}(\phi_1)\,, \tag{3.59}$$

where E_{II}^n is the n-th summand in (3.56). It depends, apart from a phase factor, on the amplitude of the phase shift ϕ_1 and the aperture size $2a$. As discussed in Sec. 3.3, every summand with $n \geq 2$ can be neglected due to condition (3.38).

It is known from the diffraction at an aperture that the width of the diffraction pattern depends on the ratio of the wavelength and the size of the aperture. A clear diffraction pattern occurs only if these two quantities are of the same order of magnitude. If the size of the aperture is much greater than the wavelength, the incoming wave is almost undisturbed and remains localized. This becomes clear if the limit $a, b \to \infty$ in (3.55) is performed in such a way that the conditions (3.53) are still satisfied. In this case, the resulting electric field is given by

$$\lim_{a,b\to\infty} E_{II} \propto \sum_{n=-\infty}^{\infty} e^{-in(\varphi-\pi/2)} \mathrm{J}_n(\phi_1)\delta(k_x - nk)\delta(k_y)\,, \tag{3.60}$$

where δ is the delta distribution. In the case of phase contrast imaging, the dimensions a and b are usually much greater than the wavelength $\lambda_\mathrm{b} = 2\pi/k_\mathrm{b}$. This means the maxima described in (3.56) are highly localized and every maximum propagating at angle θ_n describes a light ray. In Sec. 3.3 the need for phase shifting the $n = \pm 1$ component by $\pi/2$ relative to the $n = 0$ component became evident. According to (3.57), the scattering angle depends on the value of n. The unscattered ($n = 0$) component is independent of k and k_b. This separation in real space allows for a phase retardation or advancing of the unscattered wave relative to the scattered waves ($n \neq 0$). It is achieved by changing the optical path length either by a transmissive or a reflective phase plate. A transmissive phase plate is made of regions with different optical thickness. A light ray passing through is partly shifted in phase. Different from that a reflective phase plate obtains the phase shift by a groove or a dent which increases for the unscattered wave the travel distance by $\lambda_\mathrm{b}/4$. For phase contrast imaging, a reflective phase plate is normally used owing to easier manufacturing.

As we have seen above, the scattering process is two dimensional: the variation of a refractive index perturbation along the x'-axis leads to a scattering in the $x'z$-plane. Thus, the diffraction pattern of a phase grating rotated around the z-axis is tilted by the same angle as the phase grating itself. This is an important property as it allows to select for specific fluctuation orientations by masking specific angles. If we assume turbulent fluctuations to be well aligned with the magnetic field lines and a variation of the magnetic

field angle along the line of sight, a selection of a specific fluctuation orientation corresponds to a position along the the line of sight. Thus masking the fluctuation orientation can present a mean for spatial localisation along the line of sight.

The above made discussion was done for a simple sinusoidal phase grating. However, turbulent fluctuations exhibit a broadband wavenumber spectrum. A general representation of a phase modulation due to broadband fluctuations is given by its Fourier representation

$$\phi(x') = \int_{-\infty}^{\infty} \hat{\phi}(k) e^{ikx'} \, \mathrm{d}k \quad \text{where} \tag{3.61}$$

$$|\hat{\phi}(k)| \overset{!}{\ll} 1 \, . \tag{3.62}$$

In can be shown that the PCI response is in this case given by [81]

$$I_{\mathrm{img}}^{\mathrm{PCI}} \propto 1 + 2 \int_{-\infty}^{\infty} \hat{\phi}(k) e^{ikx'} \, \mathrm{d}k \tag{3.63}$$

thus recovering completely the original fluctuation.

3.4.2 Oblique Incidence

In the previous calculations for simplicity the incident beam was taken to be perpendicular to the fluctuation of the refractive index. In this section the effect of a non-perpendicular incidence should be discussed. We follow again Ref. [106] and Ref. [111].

Firstly a qualitative understanding should be developed. Given a single sinusoidal perturbation in the refractive index, it extends along the beam direction as shown in Fig. 3.4. We consider the behaviour of an impinging plane wave. As noted in Ref. [111], the bending of the incoming wave due to the inhomogeneous refractive index can be ignored unless the length L of the perturbation is sufficiently small. To understand the mechanism, it is useful to follow specific points at the phase front of the incident wave, e.g., the point indicated by the red arrow. In the perpendicular $\beta = 0$ case the observed phase point experiences along its path (longitudinal direction) a

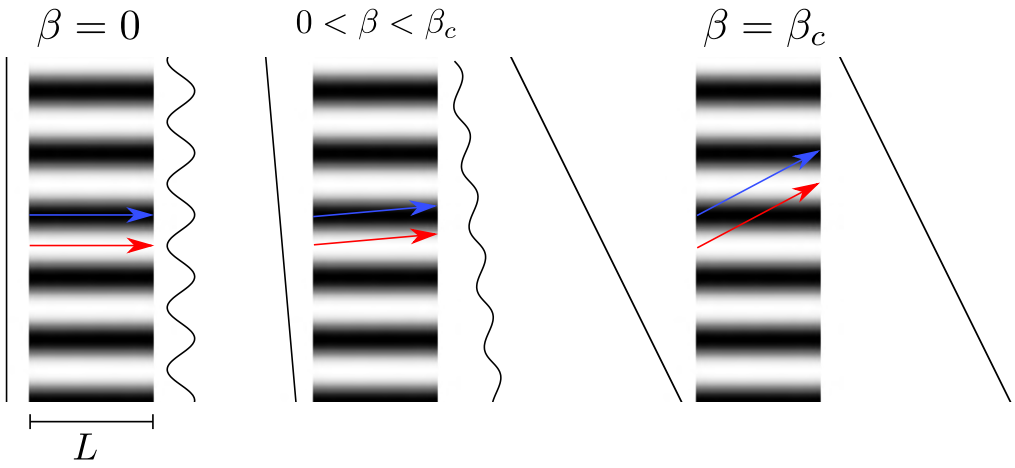

Figure 3.4: Change of wave front corrugation due to finite incidence angle β. The black lines illustrate the wave front of the incoming plane waves that are corrugated by the perturbation in the refractive index (grey-white colour coded).

constant value of $N = N_{\text{red}}$. This is valid for every phase point along the wave front of the probe beam. However a phase point, which is $\lambda/2$ shifted (blue arrow), experiences a constant $N = N_{\text{blue}}$. The two values are different $N_{\text{red}} \neq N_{\text{blue}}$ and thus the optical path lengths are different for the two phase points, which causes the corrugation on the exit of the perturbation.

This changes in the case of an angle $0 < \beta < \beta_{\text{c}}$. Now the values of N along the two different transversal positions vary also in longitudinal direction. The red arrow in Fig. 3.4 points on a value of N that is only on the admittance N_{red} and during propagation the value for N is always less then N_{red}. The same argument can be applied to the path incident by the blue arrow, apart from the fact that the value of N increases during propagation. Therefore the difference in the optical path length is reduced compared to $\beta = 0$ case, which leads to a smaller corrugation.

Finally, the corrugation disappears in the case of $\beta = \beta_{\text{c}}$. In this case, the phase point is on exit exactly shifted by λ with respect to the $\beta = 0$ position. For the $\beta = \beta_{\text{c}}$ red path N decreases from N_{red} to N_{blue} in the first half and increases from N_{blue} to N_{red} in the second half. This happens analogously with the blue path. Hence, the optical path lengths are the same and the corrugation disappears. This behaviour can be easily extended to the case where the shift at the exit is $n\lambda\,, n \in \mathbb{N}$. A simple geometrical

consideration leads to a critical angle of $\beta_{c,n} = \arctan(n\lambda/L)$. Indeed, a more precise mathematical treatment confirms this behaviour [111].

We want to treat the above problem in more general. Consider a perturbation in the refractive index

$$N(\vec{r}) = h_0(\vec{r})N_0 + h_1(\vec{r})N_1 \cos(\vec{k}\cdot\vec{r} - \varphi)\,, \tag{3.64}$$

where the functions $h_i : \mathbb{R}^3 \to [0,1]\,, i = 1,2$ are envelopes of the constant ($i = 0$) and fluctuating ($i = 1$) part of $N(\vec{r})$. The probe beam is again along the z-axis and the phase shift caused by $N(\vec{r})$ is given by (3.35) with $s = z$. The k-vector of N is not necessarily parallel to the x-axis and ϕ can be written as

$$\phi = \phi_0 + k_\mathrm{b} N_1 \int_{-\infty}^{\infty} h_1(z)\cos(k_x x + k_y y + k_z z - \varphi)\mathrm{d}z \tag{3.65}$$

where

$$\phi_0 = k_\mathrm{b} N_0 \int_{-\infty}^{\infty} h_0(z)\mathrm{d}z = \text{const.} \tag{3.66}$$

With the identity $\cos(a+b) = \cos(a)\cos(b) - \sin(a)\sin(b)$ Eq. (3.65) can be written as

$$\begin{aligned}\phi = \phi_0 &+ k_\mathrm{b} N_1 \cos(k_x x + k_y y - \varphi) \int_{-\infty}^{\infty} h_1(z)\cos(k_z z)\mathrm{d}z \\ &- k_\mathrm{b} N_1 \sin(k_x x + k_y y - \varphi) \int_{-\infty}^{\infty} h_1(z)\sin(k_z z)\mathrm{d}z\,.\end{aligned} \tag{3.67}$$

With the definitions for the cosine and sinus transform (note: the lower integral limit is now zero)

$$\mathcal{COS}[f(x)](y) = \sqrt{\frac{2}{\pi}} \int_0^{\infty} f(x)\cos(xy)dx \tag{3.68}$$

$$\mathcal{SIN}[f(x)](y) = \sqrt{\frac{2}{\pi}} \int_0^{\infty} f(x)\sin(xy)dx\,. \tag{3.69}$$

and the coefficients

$$\phi_\mathrm{s} := \sqrt{\frac{\pi}{2}} k_\mathrm{b} N_1 \, \mathcal{COS}[h_1(z) + h_1(-z)](k_z) \tag{3.70}$$

$$\phi_\mathrm{as} := \sqrt{\frac{\pi}{2}} k_\mathrm{b} N_1 \, \mathcal{SIN}[h_1(z) - h_1(-z)](k_z) \tag{3.71}$$

we finally obtain

$$\phi = \phi_0 + \phi_\mathrm{s} \cos(k_x x + k_y y - \varphi) - \phi_\mathrm{as} \sin(k_x x + k_y y - \varphi) \,. \tag{3.72}$$

This is a very similar to (3.36). From (3.49) we know that the intensity depends linearly on the coefficients ϕ_s and ϕ_as, which are proportional to the cosine and sine transform and are functions of k_z. Without knowing the exact shape of $h_1(z)$, we can expect, due to the properties of the sine and cosine transform, for a broad envelope a narrow function in k_z which approaches quickly zero for greater k_z. In other words: the more the perturbation is oriented along the beam (greater k_z) the smaller is the resulting intensity. This is demonstrated with the help of a Gaussian envelope along the z-axis

$$h_1(z) = e^{-\frac{z^2}{L^2}} \,, \tag{3.73}$$

where L is the effective length. The perturbation is rotated around the y-axis by an angle β resulting in

$$N(\vec{r}) = N_0 h_0(\vec{r}) + N_1 e^{-\frac{z^2}{L^2}} \cos(k\cos(\beta)x + k\sin(\beta)z - \varphi) \,, \tag{3.74}$$

hence $k_x = k\cos(\beta)$, $k_y = 0$ and $k_z = k\sin(\beta)$. The envelope is symmetric $h_1(z) = h_1(-z) \Rightarrow \phi_\mathrm{as} = 0$ and thus the cosine transform is proportional to the Fourier transform. With [109]

$$\mathcal{COS}\left[e^{-\frac{x^2}{L^2}}\right](y) = \frac{\sqrt{2}}{2} L e^{-L^2 y^2/4} \tag{3.75}$$

we obtain

$$\phi_\mathrm{s} = \phi_1 e^{-k^2 L^2 \sin^2(\beta)/4} \,, \tag{3.76}$$

where

$$\phi_1 = \sqrt{\pi} k_\mathrm{b} N_1 L \tag{3.77}$$

is the value for the $\beta = 0$ case. Equation (3.76) has its maximum at $\beta = 0$ and approaches zero for $\beta > 0$. The width of the peak is determined by

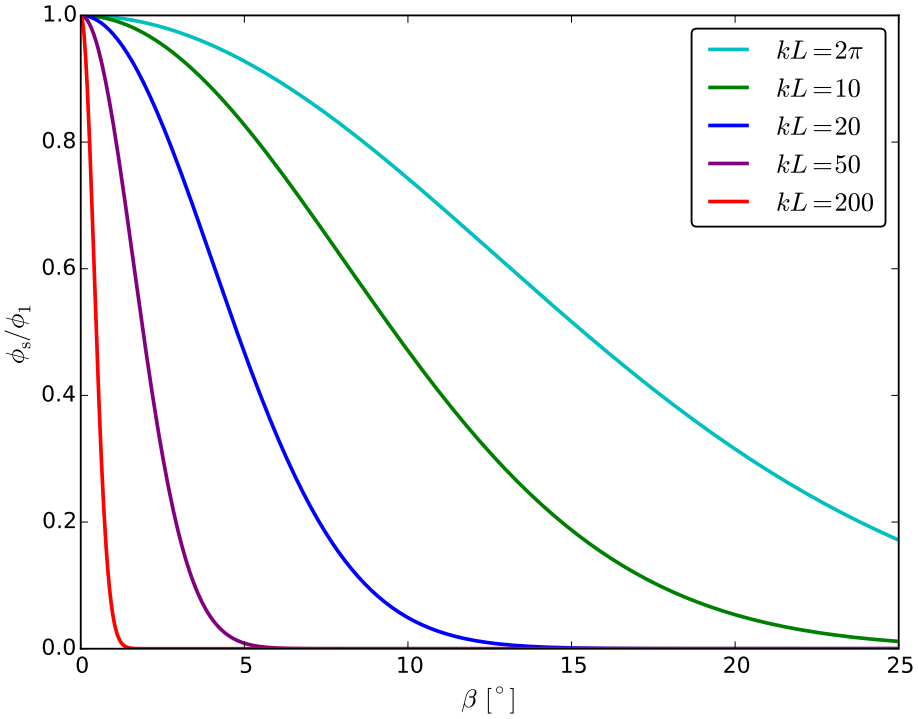

Figure 3.5: ϕ_s/ϕ_1 as function of β for different values of kL. With greater values of kL the PCI signal drops off very quickly.

the value kL. Its lower limit can be found by assuming a wavelength λ not longer than the effective length L which results in $kL = 2\pi L/\lambda \geq 2\pi$. The value of ϕ_s/ϕ_1 as function of β for different values of kL is shown in Fig. 3.5. It turns out that the PCI signal is very sensitive to the incident angle β, at least for great values kL. For these values, the PCI signal results mainly from perturbations propagating perpendicular to the probe beam. The exponential decrease for a Gaussian envelope has been experimentally verified for scattering of a HeNe laser at ultrasonic waves in air [112].

One final note: The linear response of the PCI system depends highly on the successful shift of the $n = \pm 1$ order beams relative to the $n = 0$ order beam. This means, if the zero order component does not encounter the groove in the phase plate, the response is only in the order of ϕ^2 as shown in Eq. (3.47). From (3.55) we see that the $n = 0$ term depends only on the integration area and not on the perturbation. If the integration area does not change the $n = 0$ order component is always in the same direction.

3.5 Limiting Effects

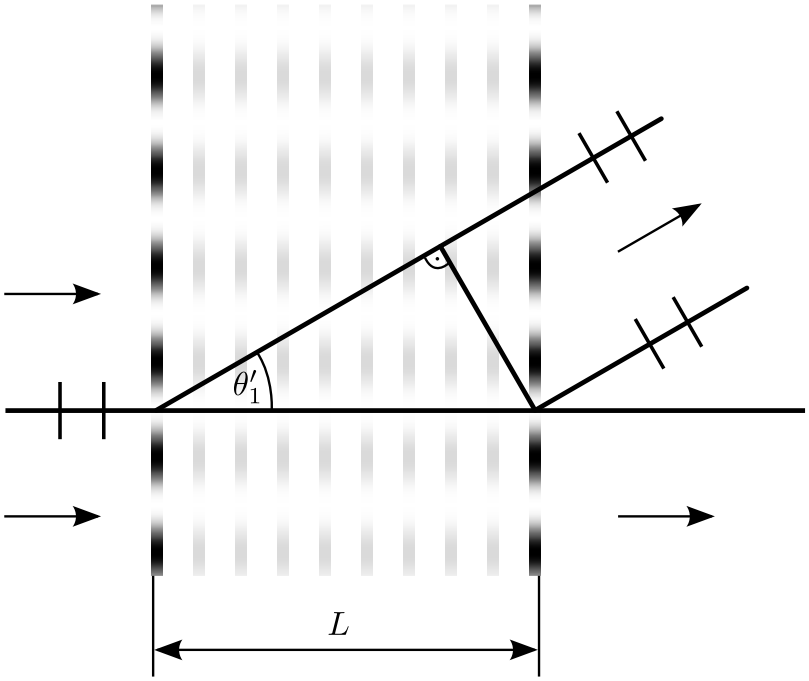

Figure 3.6: Scattering at a phase grating with finite extent. The extended phase grating can bes seen as many thin phase gratings. It can be considered as thin as long as the phase difference between the scattered waves is small (figure inspired by [113], p. 389)

.

In the previous sections, the scattering of the incoming wave was treated as to occur from a single infinite thin plasma layer. Real plasmas do have a finite extend but behave under certain circumstances similar as described above. Following the approach described in Ref. [113], the limits of the thin plasma approximation are identified by dividing an extended scattering volume in multiple, sufficiently thin layers, as shown in Fig. 3.6. The phase difference between two waves scattered at the front and at the backside is given by

$$\Delta\phi = k_\mathrm{b} N_0 L[1 - \cos(\theta_1')] \tag{3.78}$$

$$= 2k_\mathrm{b} N_0 L \sin^2\left(\frac{\theta_1'}{2}\right) \tag{3.79}$$

where $1 - \cos(x) = 2\sin^2(x/2)$ was used and the relationship between the vacuum wave number k_b and its value in the medium given by $k_0' = k_\mathrm{b} N_0$.

The modified wave number must also be considered in (3.57) and one obtains

$$\sin(\theta_1') \approx \theta_1' = \frac{k}{N_0 k_\mathrm{b}} \quad \text{for} \quad \theta_1' \ll 1\,. \tag{3.80}$$

The refractive index appears now because the superposition after the phase modulation happens in the medium, whereas in the previous calculations the diffraction integral was performed in the vacuum after the phase modulating layer. The phase shift can be written as

$$\Delta\phi = \frac{1}{2}\frac{Lk^2}{N_0 k_\mathrm{b}}\,. \tag{3.81}$$

If $\Delta\phi \ll 1$ the scattered waves interfere constructively and the scattering volume appears to be thin. Due to $N_0 \approx 1$ we can write as a condition for the interaction length

$$L \ll L_\mathrm{max} = \frac{2k_\mathrm{b}}{k^2}\,. \tag{3.82}$$

For fluctuations in the ion scale ($k \approx 3\,\mathrm{cm}^{-1}$) we find $L_\mathrm{max,i} \approx 13\,\mathrm{m}$ and for the electron scale ($k \approx 30\,\mathrm{cm}^{-1}$) it is $L_\mathrm{max,e} \approx 0.13\,\mathrm{m}$. The plasma diameter for the PCI diagnostic on Wendelstein 7-X is about 1.4 m. Thus for ion scales the plasma can be approximated as thin layer whereas fluctuations in the electron scale must be already very localised. Treating the plasma as a thin object is a very common approach for the description of the PCI. In general the thin scattering layer treatment is often referred to as the *Raman-Nath regime* and separated by the Klein-Cook parameter $Q = Lk^2/(N_0 k_\mathrm{b})$ ($Q \ll 1$) from the *Bragg regime* $Q \gg 1$ [114]. In general the Raman-Nath regime is characterised by the occurrence of many diffraction orders, whereas in the Bragg regime only one diffraction order occurs. Although Q is traditionally used in the field of acousto optics to differentiate between Raman-Nath and Bragg regime, there exist cases where it is not reliable and alternatives were proposed e.g. in Ref. [115]. A more detailed approach involves solving the wave equation in quasi-homogeneous media [116–119].

Another simplification was made by ignoring the finite propagation time of the laser. This is valid as long as the transit time is smaller than the time scale of the signal $L_\mathrm{plasma}/c \ll 1/f_\mathrm{s}$ (f_s is the signal frequency and L_plasma the plasma length). For the PCI position this gives $f_\mathrm{s} \ll 210\,\mathrm{MHz}$. Drift wave turbulence is observed up to $\approx 1\,\mathrm{Mhz}$, thus far below the limitation.

In reality non-ideal hardware elements influence the signal. As shown in Sec. 3.3, the linear response of the PCI system depends on the success of

shifting the $n = 0$ component by $\pi/2$. In reality the phase shift will never be exactly $\pi/2$. The error can be described by an additional phase δ and the electric field at the image plane for a single sinusoidal perturbation can be written as [106]

$$E_{\text{img}}^{\text{PCI}} = E_A e^{i\tilde{\phi}_0} \left[ie^{i\delta} + i\phi_1 \cos(kx' - \varphi)\right] + \mathcal{O}(\phi_1^2)\,. \tag{3.83}$$

The resulting intensity becomes

$$I_{\text{img}}^{\text{PCI}} \propto 1 + 2\phi_1 \cos(\delta)\cos(kx' - \varphi) + \mathcal{O}(\phi_1^2)\,. \tag{3.84}$$

For small values δ, the cosine can be expanded and it turns out that the error due to a non perfect phase plate is of the order of δ^2.

Although the PCI response is linear in ϕ_1, its contribution to the total signal (3.49) is still very small as given by Eq. (3.38). To improve the contrast, the signal can be either measured by an AC coupled detector, which measures only the fluctuating part $\propto \phi_1$ or the intensity of the $n = 0$ component is reduced by a fraction $\rho < 1$ as described in Ref. [119]. The modified electric field at the image plane transforms to

$$E_{\text{img}}^{\text{PCI}} = E_A e^{i\tilde{\phi}_0} \left[i\sqrt{\rho} + i\phi_1 \cos(kx' - \varphi)\right] + \mathcal{O}(\phi_1^2)\,, \tag{3.85}$$

which leads to the intensity

$$I_{\text{img}}^{\text{PCI}} \propto \rho + 2\sqrt{\rho}\phi_1 \cos(kx' - \varphi) + \mathcal{O}(\phi_1^2)\,. \tag{3.86}$$

Thus the ratio of the AC to the DC part is increased by a factor $1/\sqrt{\rho}$. Further information can be found in [101, 119]. For a quantitative discussion of limitations arising from the specific implementation see Sec. 4.5.

Chapter 4

PCI Implementation on Wendelstein 7-X

In this chapter we discuss the implementation of the PCI diagnostic on Wendelstein 7-X. While the design should be as flexible as possible to cover spatial scales from the ion down to the electron scale and frequency scales up to several hundred kilohertz, the specific requirements of Wendelstein 7-X complicate the design. Most importantly the long beam path of more than 20 m and the limited torus hall access during operation requiring remote control capabilities.

4.1 Main Design Considerations

As discussed in the previous chapter, the most simple PCI system consists of four elements: a collimated, monochromatic light source, a phase object, a phase plate and some imaging optics. In this rather theoretical set up the light is diffracted at the phase grating and mapped on the phase plate which is placed in infinite distance to the phase object. According to Fraunhofer diffraction theory, the electric field on the phase plate is the Fourier transform of the electric field after the phase object. The spatial separation of light rays due to the scattering allows for shifting the $n = \pm 1$ components relative to the $n = 0$ component, hence converting the phase modulation into an intensity modulation in the image plane created by the subsequently placed

	$k\rho_s$	k [cm^{-1}]	λ [cm]	θ [rad]	θ [°]
ITG	0.2	0.5	11	1×10^{-4}	0.005
TEM	1	2.7	2.3	5×10^{-4}	0.03
ETG	10	27	0.23	5×10^{-3}	0.3

Table 4.1: Expected wave numbers and scattering angles for different instabilities in Wendelstein 7-X. These values were calculated for the PCI laser with a wave length of $\lambda_\mathrm{b} = 10.6\,\mu\mathrm{m}$ and a magnetized plasma with $B = 2.5\,\mathrm{T}$, $T_e = 4\,\mathrm{keV}$, $m_i = m_p + m_n$ resulting in $\rho_s = \sqrt{m_i T_e}/(e_0 B) = 3.7\,\mathrm{mm}$.

imaging optics.

Practical limitations imposes a number of constraints which add complexity to the system. The most obvious limitation might be the requirement of an infinite distance between phase object and phase plate. This limitation can be overcome by placing an off axis parabolic mirror (OAP) after the phase plate creating the Fourier plane at a finite distance. The ultimate goal of the diagnostic is the measurement of turbulent, spatiotemporal quasi periodic structures in the range of ion to electron scale turbulence (c.f. Table 4.1).
From this perspective a large beam diameter is desirable as it increases the k-space resolution $\Delta k = 2\pi/d_\mathrm{b}$ with d_b being the beam diameter (see also 4.5 for more details about the limitations). Since the scattering angle $\theta = k/k_\mathrm{b}$ increases with k, the maximum beam diameter is limited by the beam enclosure before it can encounter any optical components which limit the divergence. If the scattering angle is to large for the given geometry of the beam enclosure, scattered components are lost and lead to a modification of the intensity response (3.49). Therefore, the design is naturally a balance between k-resolution and expected k-range. This requirement can be met if the beam size is adjustable with two telescopes, allowing to set the necessary beam diameter based on the k-range of interest.

As mentioned before, a CO_2 laser is chosen as light source: it provides an intense, monochromatic and directed infrared light source at a wave length of $\lambda_\mathrm{b} = 10.6\,\mu\mathrm{m}$ and a frequency of $f_\mathrm{b} = 28\,\mathrm{THz}$. The choice of wave length can be justified by considering the following aspects: on the one hand a small k_b or a large $\lambda_b \propto 1/k_\mathrm{b}$ is desirable as it increases the scattering angle $\theta = k/k_\mathrm{b}$, allowing to measure also small k-values whose $n = \pm 1$ components would otherwise fall into the phase plate groove preventing phase contrast. On the other hand, there exists an lower limit for the angular beam frequency

$\omega_\mathrm{b} = ck_\mathrm{b}$ by the approximation $\omega_\mathrm{b} \gg \omega_{pe}$ which allowed to linearise the relation ship (3.27) between refractive index and density. In Sec. 3.2 the plasma frequency was estimated for a high density of $n_e = 1 \times 10^{21}\,\mathrm{m}^{-3}$ to be $f_{pe} = 0.28\,\mathrm{THz}$, thus two orders of magnitude below f_b. The wavelength dependent scattering angle can impose a limit on the beam diameter which also limits the spatial Nyquist criterion. These limits depend highly on the specific implementation and are discussed in Sec. 4.5. Since the infrared laser radiation is invisible a second HeNe laser is installed which emits in the visible light range.

The superconducting magnetic field coils of Wendelstein 7-X are enclosed by a cryostat maintaining thermal insulation. As a result access to the plasma vessel is given by ports which are approximately two meters away from the plasma surface. This results in a total path length between the windows of 5.4 m, putting a strong constrain on the required beam position accuracy. In addition, the beam path length of more than 20 m increases the overall sensitivity of the system for drifts of the alignment. As torus hall access for alignment work is not possible during operation remote control capabilities were implemented (c.f. Sec. 4.4).

4.2 Diagnostic Setup

Figure 4.1 shows the PCI diagnostic in the Cartesian coordinate system of Wendelstein 7-X and Fig. 4.2 a component overview. The beam passes the magnetic axis at an toroidal position of 260.6°, which is 8.6° away from the next triangular shaped plane, hence the poloidal cross section is almost triangular shaped (the toroidal distance between triangular and bean shaped plane is 36°). It crosses the plasma at an angle of approximately 18° relative to the horizontal plane. The vertical plane defined by the beam is approximately 5° off the poloidal plane at this toroidal position. On the laser optics table (bottom left corner in Fig. 4.2) the laser beam is created, magnified and sent to a mirror box containing two mirrors which have a diameter of 9 ” $\approx$ 23 cm. From the mirror box the beam is redirected into the plasma. After the plasma a second mirror box, similar to the first one, redirects the beam to the receiving side optics table where the imaging optics are installed to map the signals from the plasma on two different detectors.

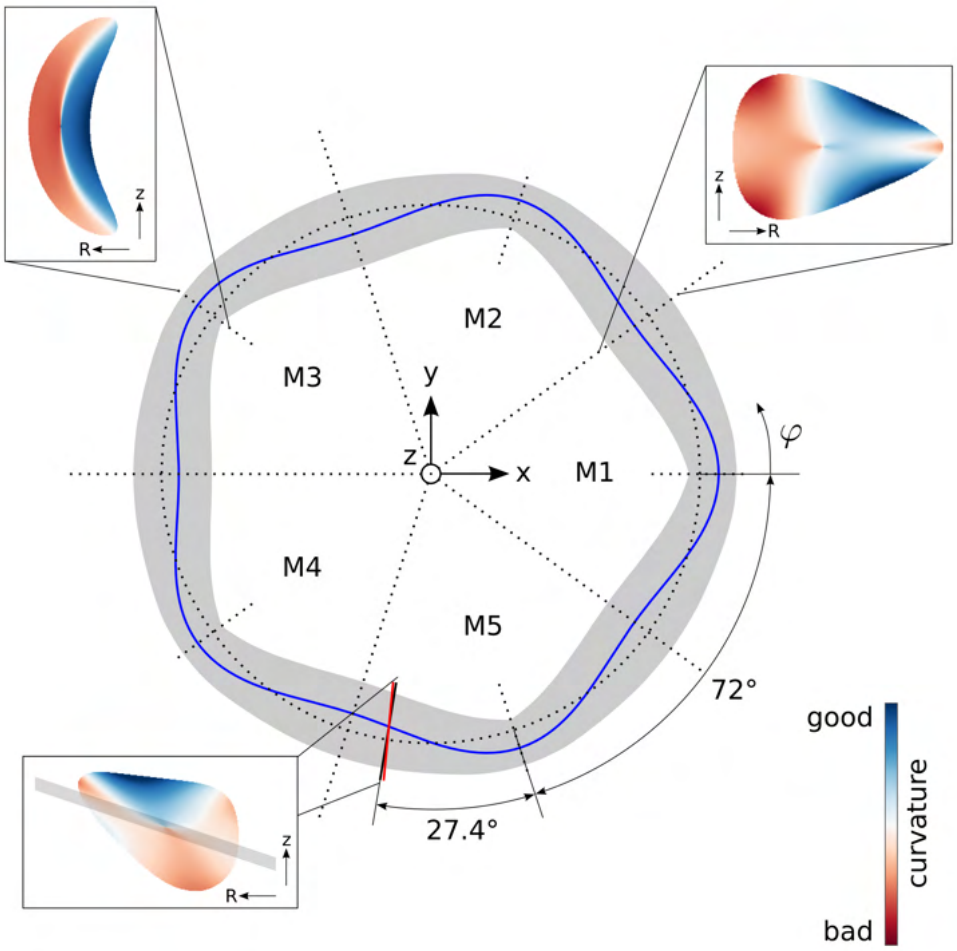

Figure 4.1: The PCI diagnostic position in the Cartesian coordinate system of Wendelstein 7-X. The blue line indicates the position of the magnetic axis. The grey area is the projection of the last closed flux surface (LCFS) onto the xy-plane. The red line shows the path of the PCI beam and the (slightly tilted) black line the projection onto the $\varphi = \text{const}$ plane. Due to the five-fold symmetry all components are grouped in five modules (labelled M1 – M5). The small figures show the LCFS in the poloidal plane. Their shape is repeated every period i.e. $\Delta\varphi = 72\,.$

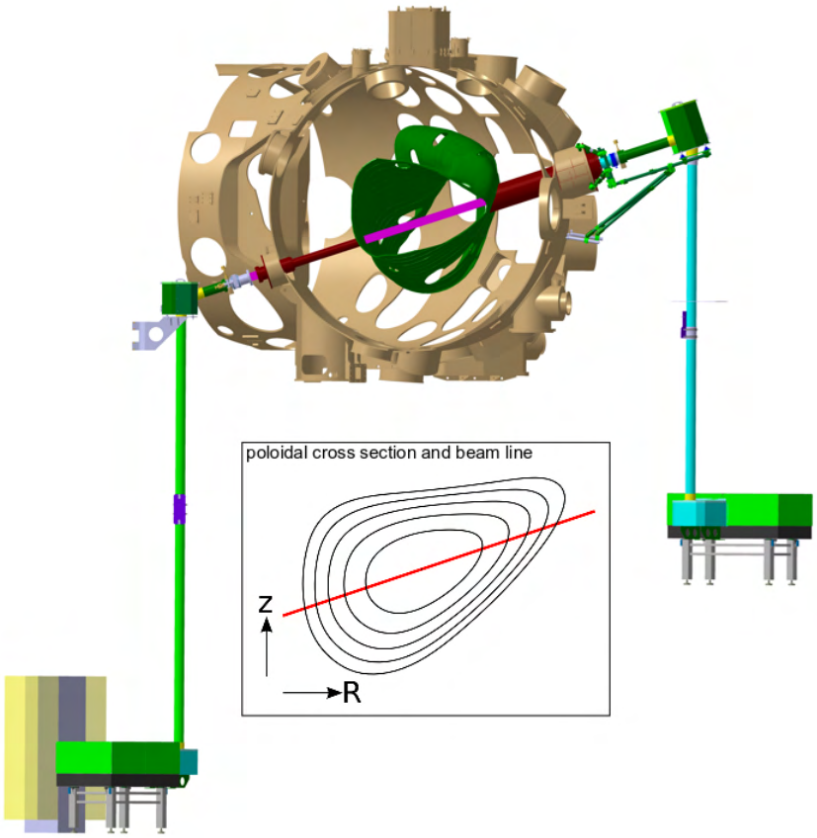

Figure 4.2: Component overview of the PCI diagnostic on Wendelstein 7-X. The transmitting side optics table housing the laser is shown on the bottom left, the receiving side optics table on the right.

4.2.1 Transmitting Side Optics Table

Central component of the transmitting side optics table is the CO_2 laser (c.f. Fig. 4.3 and Fig. 4.4). Attached to the CO_2 laser is a water cooled shutter which allows a quick switching of the laser without the need to cut the power. This makes it possible to keep the laser in thermal equilibrium not only during operation, but also during alignment work. Straight after the shutter a lens reduces the initial divergence of the beam. It encounters next the first 50/50 beam splitter. Half of the laser power is dumped on an air cooled beam dump in order to not overexpose the detectors on the receiving side table. As mentioned above, it is favourable to substitute most

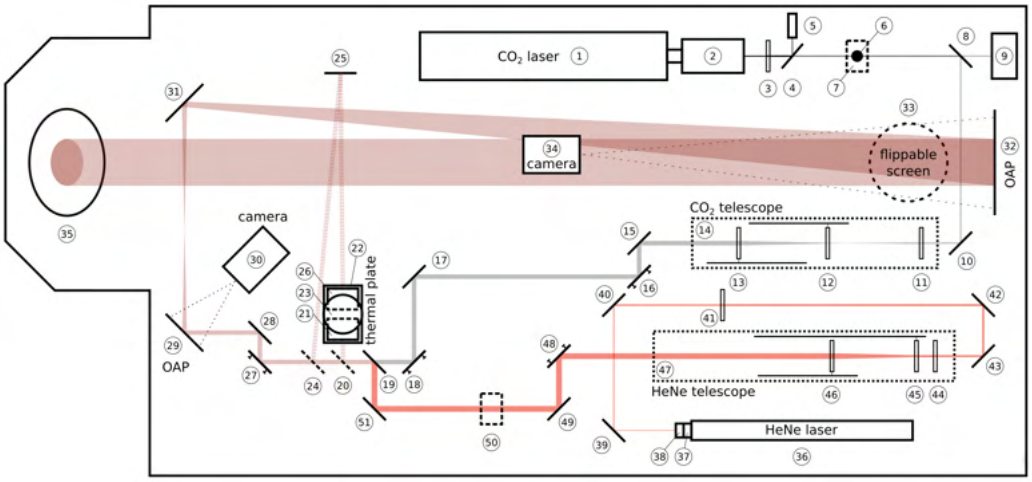

Figure 4.3: Sketch of the transmitting side optics table. Dimensions are not to scale. See Table A.1 for a detailed list of all components.

of the infrared laser beam path with a visible laser system. Therefore the light of a small laser diode is injected via a flipper mirror mount into the beam path, allowing for visual checks of the alignment. A second 50/50 beam splitter dumps half of the remaining power on a power meter for direct observation of the emitted infrared radiation power. The remaining 25% of the initial power are then sent into the first telescope, consisting of three lenses (c.f. Fig. 4.5). Two of these lenses are mounted on a rail system for precise mechanical guidance and can be moved by two remotely controllable linear stages in order to change the overall magnification of the system. After the telescope the infrared beam encounters four steerable mirrors in order to set position and direction of the beam on the 9" = 22.86 cm focal length off-axis parabolic (OAP) mirror further downstream. In the next step the infrared laser is combined with the visible HeNe laser emitted from a second branch and mapped, in this order, via a number of plane mirrors on a small OAP (f=9"), a plane and a larger OAP (f=80") mirror and leaves then the optics table towards the plasma. The two OAP mirros form a telescope with a fixed magnification of 80"/9" $\approx$ 9. Two flippable plane mirrors between the beam combiner and the plane mirrors in front of the small OAP mirror allow for redirecting the combined beam with different optical path lengths on a thermal plate for imaging the IR laser beam.

The HeNe laser (wavelength of 632.8 nm) follows conceptually a similar beam path as the infrared laser. The power can for safety reasons be reduced

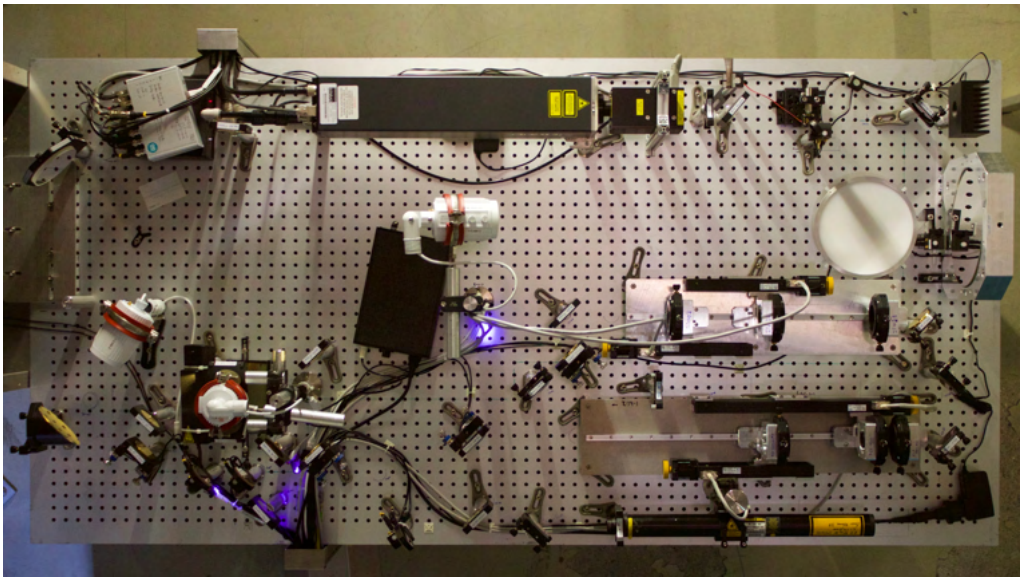

Figure 4.4: Implementation of the transmitting side optics table. The size of the table is 2 m × 1 m. For a sketch of the design and a detailed component list see Fig. 4.3 and Table A.1.

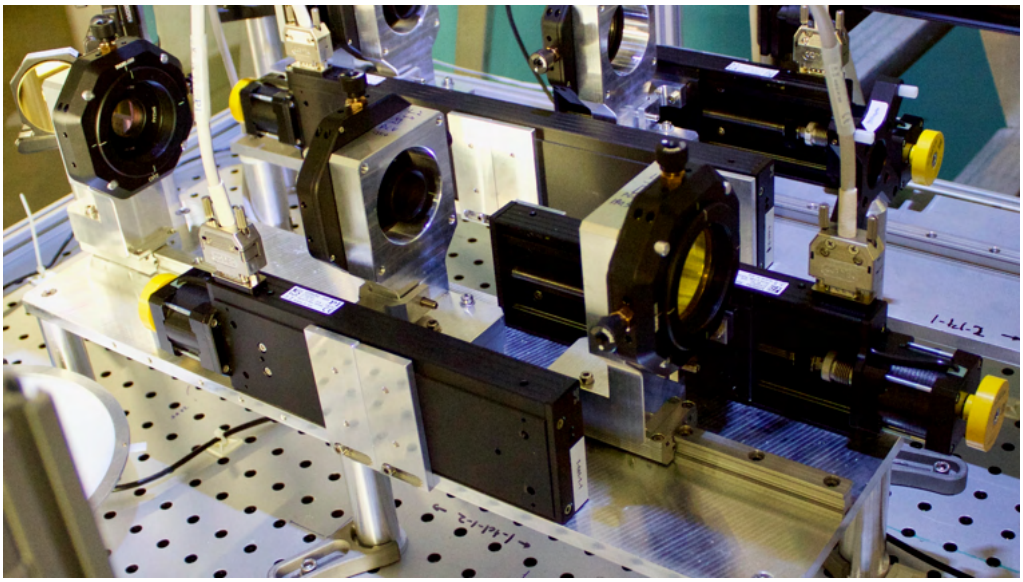

Figure 4.5: Picture of the IR telescope on the transmitting side. The movable lenses are attached to linear stages and guided by a rail system.

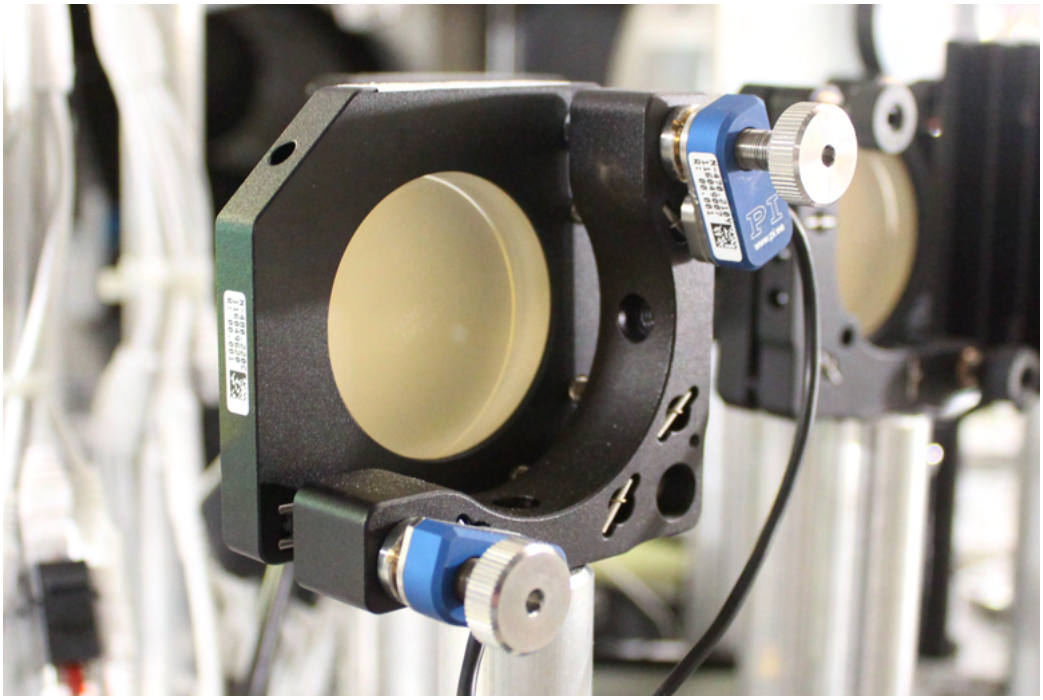

Figure 4.6: Remote steerable 2 ” lens holder motorized with piezo-interial drives. The piezo drives are uncritical in high magnetic field environments, have no holding currents and are vibration-free.

by a grey filter. A couple of plane mirrors guide the HeNe laser beam into a telescope for a flexible change of magnification. The telescope consists again of three lenses, two of them mounted on a rail system which is moved by two remotely controllable linear stages. After the telescope again plane mirrors guide the visible laser to the beam combiner where it is combined with the infrared laser.

4.2.2 Inter Optics Table Beam Path

Between the transmitting and receiving side optics table, plane mirrors (diameter 9 ” $\approx$ 23 cm) redirect the laser beams to the mirror boxes, through the AEZ-50 port window in the plasma vessel and from there in the AET-50 port in the second mirror box down to the receiving side optics table. Between the tables and the mirror boxes black iodized aluminium beam ducts (137 mm inner diameter) encapsulate the laser beams. The mirror boxes are mounted

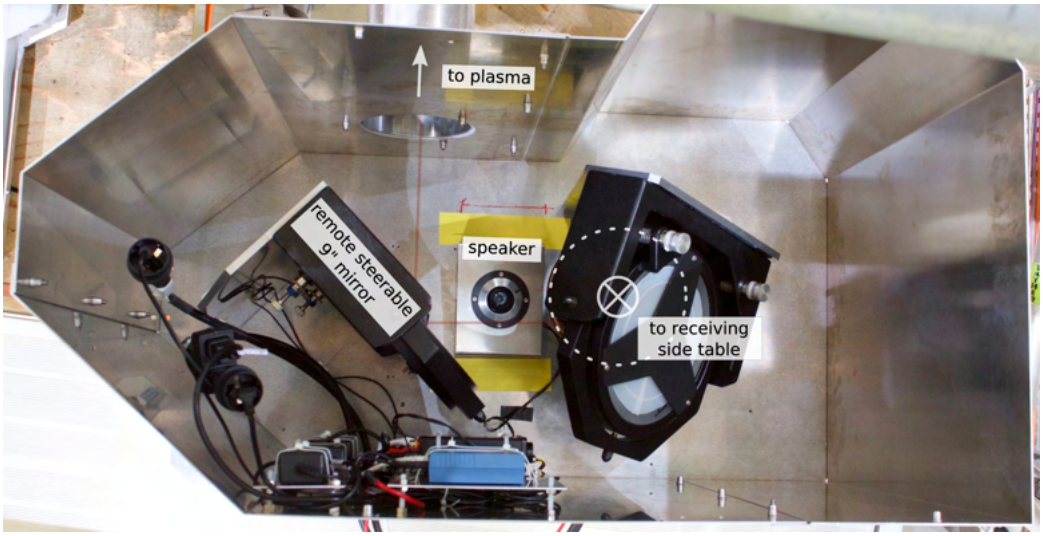

Figure 4.7: Image of the AET-50 mirror box showing the 9" mirrors M4 (remote steerable) and M5 (manually steerable), the sound speaker for calibration and related electronics. The red line indicates the optical path.

on a base plate via small, rubber made cylinders in order to reduce vibration from the attached support structures. The vacuum barrier consists out of ZnSe window mounted in a CF160 flange, equipped with a vacuum valve and a pressure sensor. The inner diameter of the AEZ-50 port sets the theoretical limit of 124 mm for the beam diameter. The outer mirror box at the AET-50 port contains a FOSTEX FT17H sound speaker as calibration source for the diagnostic. Sound bursts launched from the speaker imprint a refractive index perturbation in air which can be measured with the PCI diagnostic. The measured signal provides a reference for the direction of propagation, the wave number and intensity allowing in principal for absolute calibration of the plasma density signal.

4.2.3 Receiving Side Optics Table

On the receiving side optics table (c.f. Fig. 4.8 and Fig. 4.9), two flat 9" mirrors map the beam on a large OAP (9" diameter, 80" focal length). The converging beam is sent through a beam rotator consisting of three plane mirrors (c.f. Fig. 4.10). The beam rotator ensures that the image of the elongated plasma filaments is aligned with the 1D detector arrays, i.e.

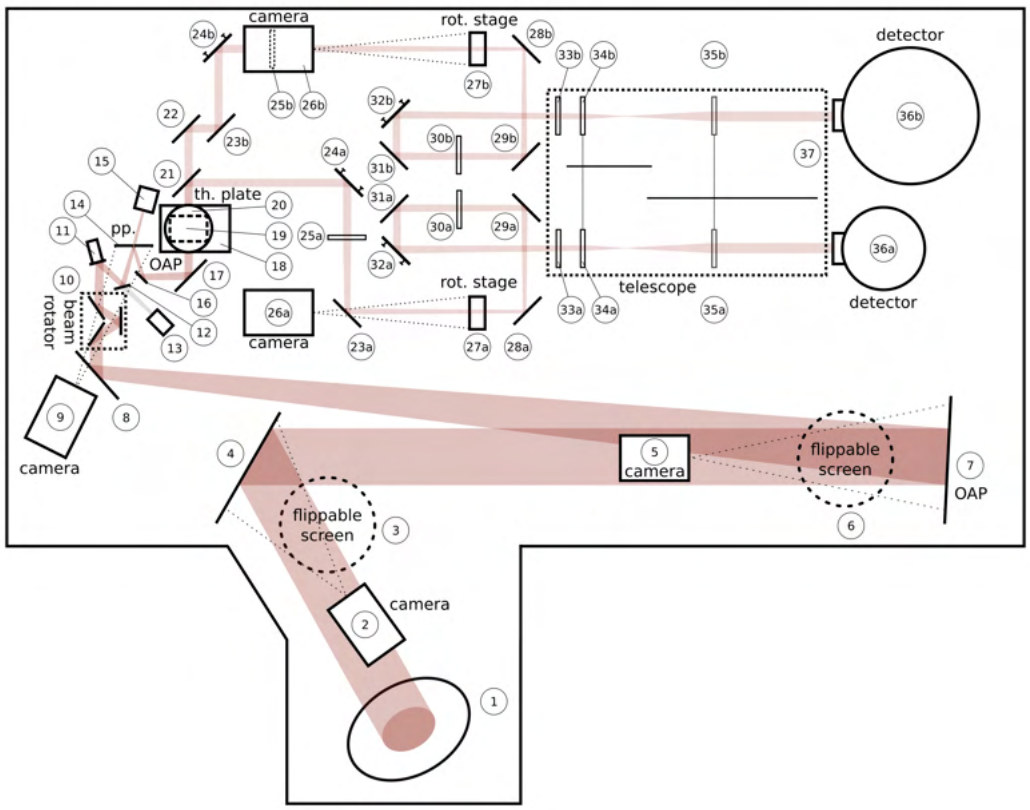

Figure 4.8: Sketch of the receiving side optics table. Dimensions are not to scale. See Table B.1 for a detailed list of all components.

the imaging is predominantly perpendicular to the magnetic field. After the beam rotator a steerable mirror and a subsequent quadrature detector form a vibration compensation system. The quadrature detector is installed behind a beam splitter and provides the feedback for the steerable mirror. The beam splitter has a 1% transmissivity for the IR light and is fully reflective for visible light. Further downstream of the beam splitter a focal point is formed on the phase plate which is essentially a 2" gold plated mirror with a 1.1 mm wide groove of depth $\lambda_b/8$ spanning a diameter. The ZnSe optic substrate has a reflection coefficient of $\rho \approx 0.28$, reducing the amplitude of the $n = 0$ component. According to (3.86) the reduced reflectivity increases the signal intensity by a factor $1/\sqrt{\rho} \approx 1.89$ over a perfectly reflective phase plate. The transmitted power is detected in a power meter to check for alignment degradation. The reflected part from the phase plate is mapped on a small OAP (6" focal length) which form with the previous large one a telescope with a fixed magnification of 80"/6" $\approx$ 13. In order to check

Figure 4.9: Overview image of the receiving side optics table. The size of the table is 2 m × 1 m. For a sketch of the design and a detailed component list see Fig. 4.8 and Table B.1.

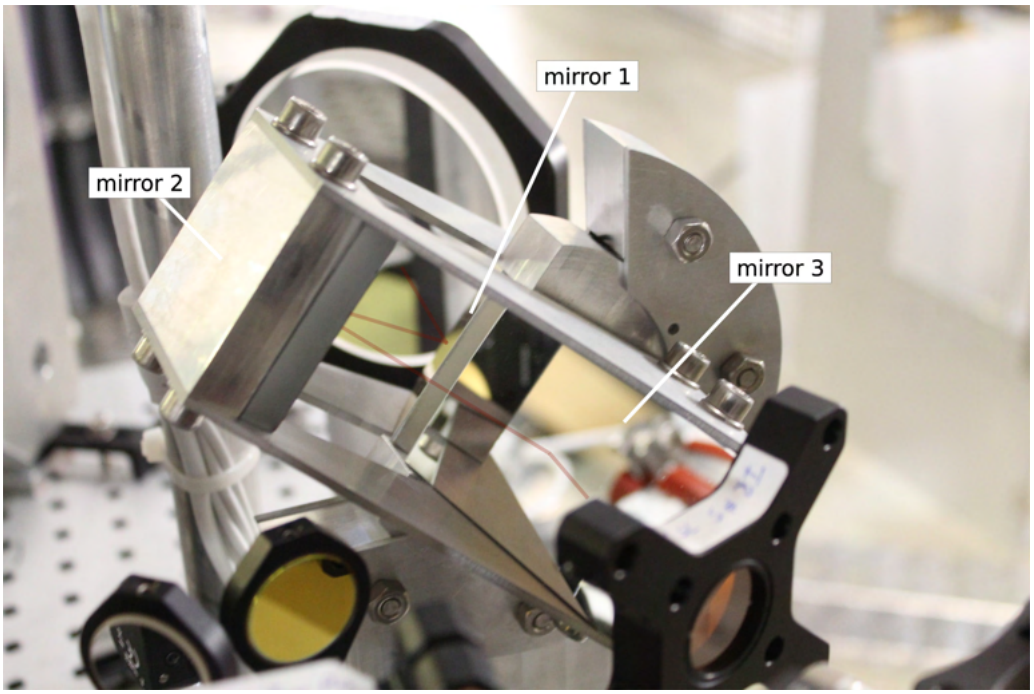

Figure 4.10: Image of the beam rotator. The red line indicates the optical path.

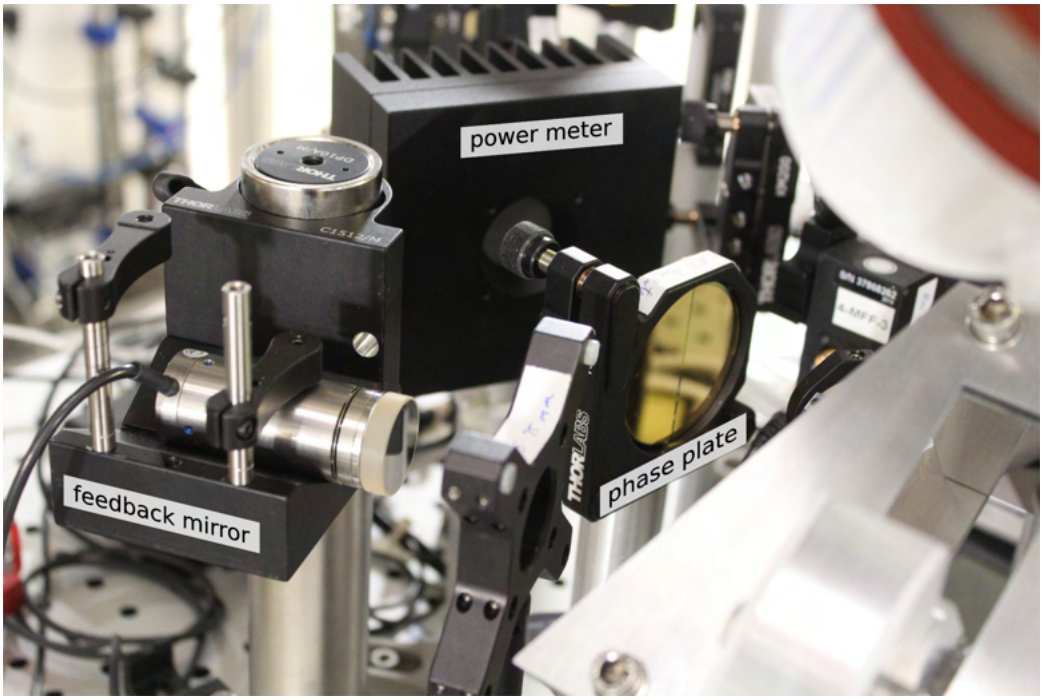

Figure 4.11: Detailed view on the phase plate and surrounding components.

co-alignment of visible and infrared laser, a flippable plane mirror behind the small OAP mirror maps the beam on a thermal plate.

As described in Sec. (3.4.1) the scattering process for a single phase grating is effectively a 2D process and selecting specific scattering angles allows for spatial localisation along the beam path. The measurement is line-of-sight integrated along the entire beam path through the plasma. However, under the assumption that the turbulent fluctuations are well aligned with the ambient magnetic field, optical filtering of specific regions of the phase plate allows to localize the measurement to specific ranges of magnetic field pitch angle and, thus, yields a radial localization. For each path, lenses create a Fourier plane at the rotational stage potentially holding a mask. Plane mirrors in between ensures the correct optical path length and allow to reduce the required space of the optical setup. After the rotating stages plane mirrors redirect the beams into a telescope, which maps them on the horizontally aligned, one dimensional photoconductive detector arrays.

4.3 Detectors

The infrared light is detected by a MCT-16-32 (detector one) and a MCT-12-32 (detector two) detector from Infrared Systems Development Corporation. Central component of each detector is the one dimensional, 32 element mercury cadmium telluride (HgCdTe) detector array. Each element has a size of $1\,\text{mm} \times 0.5\,\text{mm}$. They are stacked along the short side with a gap of $50\,\mu\text{m}$ between, resulting in a total width of 17.55 mm. The detectors are placed in a dewar cooled with liquid nitrogen (boiling point $77\,\text{K} = -196\,^\circ\text{C}$). The AC-part of the detector signals is digitized at 2 MHz after being pre-amplified. The data storage is handled by a MDS+ server.

The detectors were calibrated using an array of 114 OSRAM SFH 4059-QS LEDs operating at $0.86\,\mu\text{m}$. In order to calibrate the LED array response a Thorlabs PDA36A detector was used. The frequency response of the system detector-preamplifier is modelled as band-pass filter

$$H(f) = \frac{H_0}{\sqrt{\left(1 + \frac{f_{\text{high}}^2}{f^2}\right)\left(1 + \frac{f^2}{f_{\text{low}}^2}\right)}}\,, \tag{4.1}$$

where f_{high} and f_{low} are the high- and low-pass frequencies, respectively. Figure 4.12 shows the frequency response of detector one and the low and high pass frequencies for each detector and channel. The low-pass frequency is for both detectors around 2 kHz, the high pass frequency > 500 kHz. Between 10 kHz and 200 kHz the Amplitude response is essentially flat (c.f. top figure in Fig. 4.12). Below and above this interval the modified response has to be taken into account when considering the spectral power of a signal. The amplitude variation between channels is less important since the sound wave calibration is applied to each channel individually.

4.4 Remote Alignment

As mentioned in Sec. 4.1 the diagnostic is sensitive to misalignment due to the long optical beam path of 22 m between the optics tables and the requirement to steer the beam through the 5.4 m distant port windows, which are only slightly larger than the beam size. Limited torus access during operation imposes a further constrain requiring remote alignment capabilities. The challenge for the controlling scheme is now to identify the critical

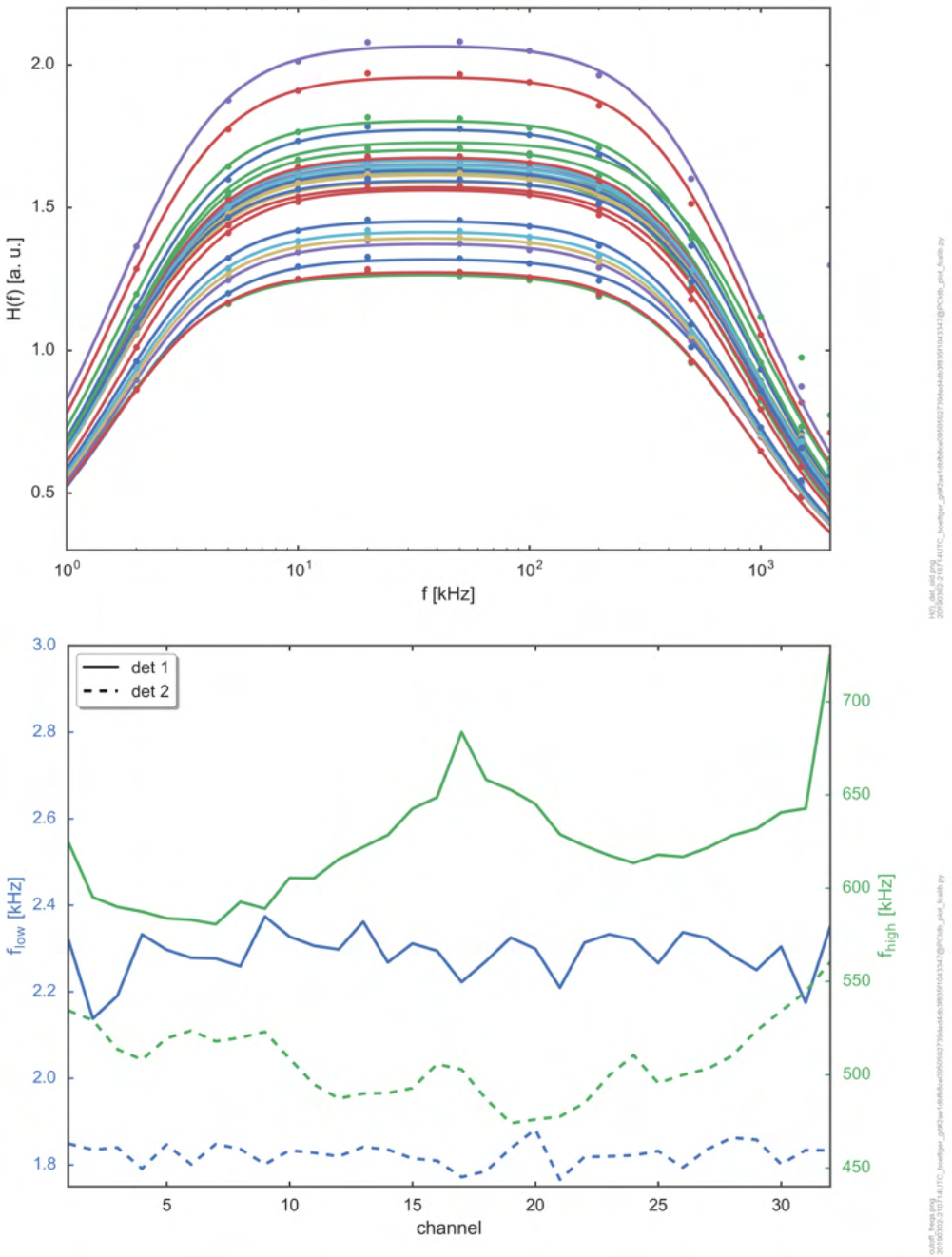

Figure 4.12: Top figure: frequency response of detector one for each channel. The dots are the measured values. Bottom figure: low- and high-pass frequencies for both detectors for for each channel.

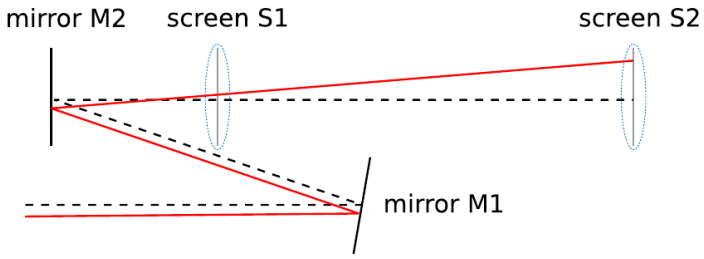

Figure 4.13: The smallest alignment unit consists of two screens and two mirrors to correct for positional and angular deviations of the beam.

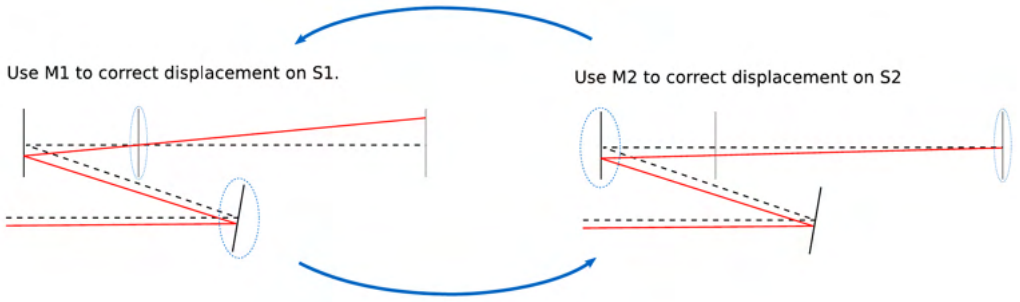

Figure 4.14: Iterative alignment cycle for planar mirrors. In each cylce the displacement is reduced by a factor $0 < r < 1$.

components/positions which need to be observed and implement appropriate countermeasures to be able to react on deviations from the ideal state while keeping the complexity of the system as low as possible. Critical are those objects, where perturbations from the ideal state lead to a significant reduction of their functionality. For example, the centring of the beam on the phase plate groove is crucial for a good measurement. In contrast, (small) positional deviations on plane mirrors do not change the principal functionality of the mirror. In terms of alignment the relevant beam properties which are affected are its position and direction along the optical path, which leaves 2×2 degrees of freedom at each position. A two axis steerable mirror can correct for two degrees of freedom which means that the smallest alignment unit for a full positional and directional error correction consists at least of two two axis steerable mirrors with two observations screens (c.f. Fig. 4.13).

As shown in Fig. 4.14 for planar mirrors the displacement on both observation screens can be iteratively reduced. We find for the displacement Δs_1^{n+1}

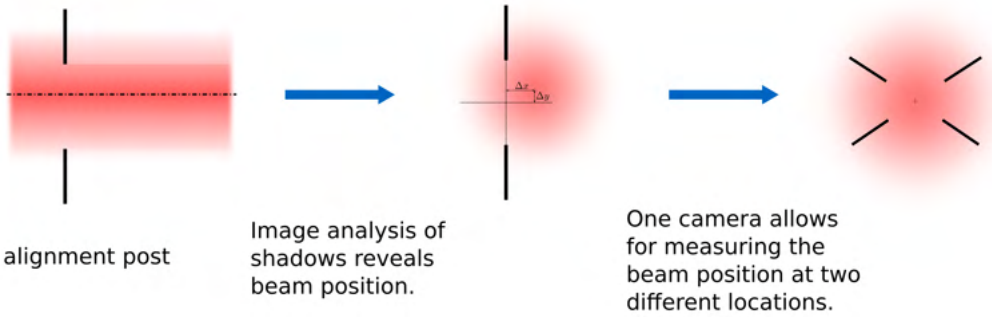

Figure 4.15: Principal scheme of beam position measurement through alignment posts inserted at positions along the beam.

on S1 in step $n+1$

$$\Delta s_1^{n+1} = \frac{d_2}{d_2 + d_3} \Delta s_2^n \,, \tag{4.2}$$

where Δs_2^n is the displacement on screen 2 in the iteration step n, d_1 the distance between M1 and M2, d_2 the distance between M2 and S1 and d_3 the distance between S1 and S2. Similar, we find for Δs_2^{n+2}

$$\Delta s_2^{n+2} \frac{d_1 + d_2}{d_1 + d_2 + d_3} = \Delta s_1^{n+1} \tag{4.3}$$

Combining (4.2) and (4.3) yields

$$\Delta s_i^{n+2} = r \Delta s_i^n \quad \text{with} \quad i = 1, 2 \tag{4.4}$$

where

$$r = \frac{1}{1 + \frac{d_1 d_3}{d_2 (d_1 + d_2 + d_3)}} < 1 \tag{4.5}$$

is the factor by which the displacement on each screen is reduced per cycle.This process converges always since $0 < r < 1$. The convergence can be increased by maximizing the distance between the mirrors and the screens (d_1 and d_3) or reducing the distance between M2 and S1 (d_2). A second simplification can be applied if we take into a account, that only a small stripe of the whole beam diameter is mapped on the linear detector array. The remaining part can be used for beam diagnosis, as shown in Fig. 4.15: in principal the shadow of posts partially inserted into the beam can be used to determine the beam position at the posts. This approach is used to monitor

the beam position on the port windows. Table 4.2 summarizes the alignment scheme.

The main diagnostic mean for determining the laser beam position are nine network cameras and power meter located behind the phase plate. The stray light of the visible laser beam is too low for a direct observation on the plane mirrors. To increase temporarily the reflectivity flippable screens are installed in front of each mirror. The final determination of the laser spot is done either by comparison with a reference image or by image processing which detects the laser spot programmatically. Table 4.2 summarizes the alignment scheme.

The control software is written in Python. A web server provides a graphical user interface and the access to single components. In order to prevent damage to the system, groups with a limited number of components and restricted paramter space are defined. To prevent these kind of unwanted motor movements, groups define a set of motors, devices and associated parameter limits which are safe to operate. The measured parameter defining the state of the PCI diagnostic (motor position, camera images, power measurements) are saved for each experimental program together with the actual measured data. As data acquisition system MDS+ is used.

#	laser	loc.	control goal	N_{pos}	N_{dir}	obs. 1	obs. 2	control 1	control 2
1	HeNe	T	large OAP (T32)	2	2	T33	T29	T27	T48
2	HeNe	wdw.	port windows	4	0	shadow on R3 or R6	-	T35/M1	M3
3	HeNe	R	large OAP (R7)	2	2	R3	R6	M4	R1/M6
4	HeNe	R	phase plate (R14)	2	0	R14	-	R1 or R11	-
5	HeNe	R	spatial filters (R27a/R27b)	2/2	0/0	R27a/R27b	-	R24a/R24b	-
6	IR & HeNe	T & R	co-alignment	2	2	T22 and R18	-	T16	T18

Table 4.2: Remote alignment scheme of the PCI diagnostic. The location prefixes 'T' and 'R' stand for the transmitting ('T') or receiving ('R') side optics table. The given numbers are those in Fig. 4.8 with table A.1 and Fig 4.3 with table B.1. For example 'T33' is element with number 33 on the transmitting side optics table. The variables N_x indicate the degrees of freedom for either position (x =pos) or direction (x=dir). M1 to M6 label the 9" mirrors which guide the beam from the transmitting side table through the vessel to the receiving side. Mirror M1≡T35 is located on the extension of the transmitting side optics table, M2 and M3 are located in the mirror box of the AEZ-50 port, M4 and M5 are in the mirror box at the AET-50 port and M6≡R1 sits on the receiving side optics table extension.

4.5 Limitations

4.5.1 Frequency and Wave Number Limits

Frequency Limits

In this section we want to discuss measurement and interpretation limits which are particular for the PCI implementation on Wendelstein 7-X. Both detectors sample at a frequency of $f_\mathrm{s} = 2\,\mathrm{MHz}$ which results in a Nyquist frequency of $f_\mathrm{ny} = f_\mathrm{s}/2 = 1\,\mathrm{MHz}$. Due to vibration of the laser beam and noise the lower limit can be estimated to be around 1 kHz. Hence, the frequency limit for data measured by the PCI diagnostic can be considered to be

$$1\,\mathrm{kHz} < f_\mathrm{PCI} < 1\,\mathrm{MHz}\,. \tag{4.6}$$

Note, although the frequency response of the detectors does not impose a hard limit on the frequency range (4.6) it might need to be taken into at the edges of the interval (c.f. Sec. 4.3).

Lower Waver Number Limit

As already mentioned the phase plate groove width w has a strong influence on the system performance. The choice of an ideal width is e.g. quantitatively discussed in [101]. Here we summarize the most important aspects. Diffraction effects lead to a finite spot width d of the beam. If the groove width is in the range or smaller than the spot size of the unscattered $n = 0$ component non-linear imaging effects occur: phase shifted parts of the central component interfere with non-shifted parts of the $n = 0$ component which are outside of the groove. This results in a severe deviation from the geometrical optic properties and non-linear effects such as image distortion. Furthermore, the overall response is reduced since only the phase shifted part of the $n = 0$ component leads to a phase contrast. For very small k or large λ the $n = \pm 1$ components move (partially) into the groove since the scattering angle becomes very small ($\theta = k/k_\mathrm{b}$). It can then happen, that parts of the $n = \pm 1$ components in the groove interfere with unshifted $n = 0$ components outside. This inverse phase shift effect leads to a (partial) cancellation of the signal. Assuming the groove width is sufficiently large (i.e. larger than the

spot width) in order to avoid these effects it still defines the wave number or wave length response. For such a large w the spot of the $n = 0$ component might fit fully into the groove, but any $n = \pm 1$ component with a separation distance s smaller than the groove width is not phase shifted, hence no phase contrast occurs. This limitation characterizes the lower wave number limit k_{min}. From this perspective a very large groove width is not desirable as it leads to an unnecessary high low wave number limit. On the other hand vibrations lead to a movement of the beam on the phase plate and it can make sense to chose a groove width which is not too tight: for a small w (but still $w > d$) a movement of the laser might bring the $n = 0$ component out of the groove and the response for all wave numbers drop. In contrast, a larger value of w requires a higher vibrational amplitude before the central component leaves the groove. The price to pay is the increased k_{min} – but all other wave numbers do not suffer from the intensity reduction of the central component. For the PCI setup in the OP1.2b campaign a groove width of $w = 1.1\,\mathrm{mm}$ was chosen. For a quantitative assessment of k_{min} we require that the spot size separation s between scattered and unscattered component is

$$s \geq \frac{w}{2}\,. \tag{4.7}$$

A geometrical consideration yields

$$s = \frac{k}{k_{\mathrm{b}}} F_{\mathrm{eff}}\,, \tag{4.8}$$

where F_{eff} is the effective focal length. Inserting (4.8) into (4.7) yields:

$$k \geq = k_{\mathrm{min}} = \frac{w k_{\mathrm{b}}}{2 F_{\mathrm{eff}}}\,. \tag{4.9}$$

For the PCI diagnostics the effective focal length is given by the large OAP mirror on the transmitting side optics table, $F_{\mathrm{eff}} = 80\text{”} = 2.032\,\mathrm{m}$. Together with $w = 1.1\,\mathrm{mm}$ and $\lambda_{\mathrm{b}} = 10.6\,\mu\mathrm{m}$ we find $k_{\mathrm{min}} = 1.6\,\mathrm{cm}^{-1}$. A possible second lower limit for the wave number arises from the finite beam width, or to be more precise, the spatial range d of the plasma which is mapped on the detector. This finite range leads to a wave number resolution $\Delta k = 2\pi/d$. This raises the question if the diffractional limit (4.9) or the the finite wave number resolution determines the lower k limit. In order to give an answer we might ask for the critical diameter d_c below the wave number resolution exceeds the diffractional limit:

$$k_{\mathrm{min}} < \Delta k_c \quad \Leftrightarrow d < d_c = \frac{2\pi}{k_{\mathrm{min}}}\,. \tag{4.10}$$

For the above given value of $k_{\min}$ we find $d_c = 3.9\,\mathrm{cm}$. In all plasma measurements so far d was always above d_c, hence the diffractional limit (4.9) defines the lower wave number limit which reaches in the wave number range of ion scale turbulence. However, the design of the PCI diagnostic incorporates also an operation regime with strongly reduced beam size for fluctuation measurements in the electron scale range. In this large wave number regime the large scattering angle (compared to ion scale, c.f. Table 4.1) leads to a loss of the $n = \pm 1$ components at the beam enclosure. In order to avoid this the beam diameter is reduced and the effective sampled beam diameter can drop below d_c.

Upper Wave Number Limit

The loss of scattered components at the beam enclosure, imposes also an upper limit. If the scattering angle θ it too large, the transversal displacement r_s of the scattered component exceeds the critical beam duct radius r_c before it encounters the large OAP on the receiving side optics table which reduces the divergence. The condition for preserving the scattered component reads

$$r_c > r_b + r_s = r_b + l_p \tan(\theta) \approx r_b + l_p \frac{k}{k_\mathrm{b}}\,, \tag{4.11}$$

with r_b being the beam radius and l_p the distance along the optical axis between scattering volume and considered position. In the last step we used the simplification $\tan\theta \approx \sin\theta \approx \theta$ since $\theta \ll 1$. We solve (4.11) for k and find

$$k < k_c = \frac{k_b}{2l_p}(d_c - d_\mathrm{b})\,, \tag{4.12}$$

where we expressed the radius in terms of the diameter $d_i = 2r_i$, $i = c, b$. If $k < k_c$ all scattered components can reach the OAP before they are lost at the wall. As we can see from (4.12) k_c is a function of the beam diameter. A second limitation arises from the spatial Nyquist limit

$$k_n = \frac{\pi N}{d}\,, \tag{4.13}$$

where N is the number of detector elements and d the diameter of the beam which is mapped on the detector. We make the ansatz $k_n(d_b) = k_c(d_b)$ in order to find out which limit is more restrictive when considering different

beam diameters. A short calculations yields

$$d_b = \frac{d_c}{2} \pm \sqrt{\frac{d_c^2}{4} - \frac{2\pi N l_p}{k_b}}\,. \tag{4.14}$$

For the PCI system it is $d_c = 150\,\mathrm{mm}$, $N = 32$ and $l_p = 11.4\,\mathrm{m}$ which gives $d_{b+} = 117\,\mathrm{mm}$ and $d_{b-} = 33\,\mathrm{mm}$. We conclude, for all $k \in [d_{b-}, d_{b+}]$ the Nyquist limit (4.13) imposes the more restrictive upper wave number limit. The theoretical maximum beam diameter for the PCI system on Wendelstein 7-X is given by the internal pipe of the AEZ-50 port of 124 mm. However, in practice this limit is hard to reach due to alignment accuracy. For the largest possible k measurement, the choice of $d_b = d_{b-}$ provides the optimum. In this case $k_c = k_n = 30\,\mathrm{cm}^{-1}$ which reaches in the range of electron scale turbulence.

4.5.2 Wave Number Uncertainty

The orientation of the elongated plasma fluctuations depends on the orientation of the magnetic field lines along the line of sight which varies by about 25 ° for the PCI diagnostic (c.f. Fig. 4.16). Since the detector is only one dimensional a plasma wave with wavelength λ_p is detected as a wave with a projected wavelength $\lambda_m = \lambda_p \cos(\beta)$, where β is the angle between the axis of the detector element and the plasma magnetic field line direction from which the plasma wave originates. Due to the line integrated character the detector measures thus always wave numbers with different orientations which lead to an uncertainty of the measured wave number. We can estimate this uncertainty by calculating the wave number error

$$\Delta k_\beta = |k_p - k_m| = k_m |\cos(\beta) - 1| \tag{4.15}$$

$$\Leftrightarrow \frac{\Delta k_\beta}{k_m} = |\cos(\beta) - 1|\,. \tag{4.16}$$

In the most unfavourable case $\beta = 25\,^\circ$ which gives $\Delta k_\alpha / k_m \approx 10$ %. In the best case the detector is oriented in the center of the angle interval such that $\alpha = 25^\circ/2$, which yields $\Delta k_\alpha / k_m \approx 2.4$ %.

A second uncertainty for the wave number measurement can be caused by a non-perfectly collimated beam. Any real space distance d_d on the detector array translates to the actual distance d_p in the plasma via

$$d_p = M d_d \tag{4.17}$$

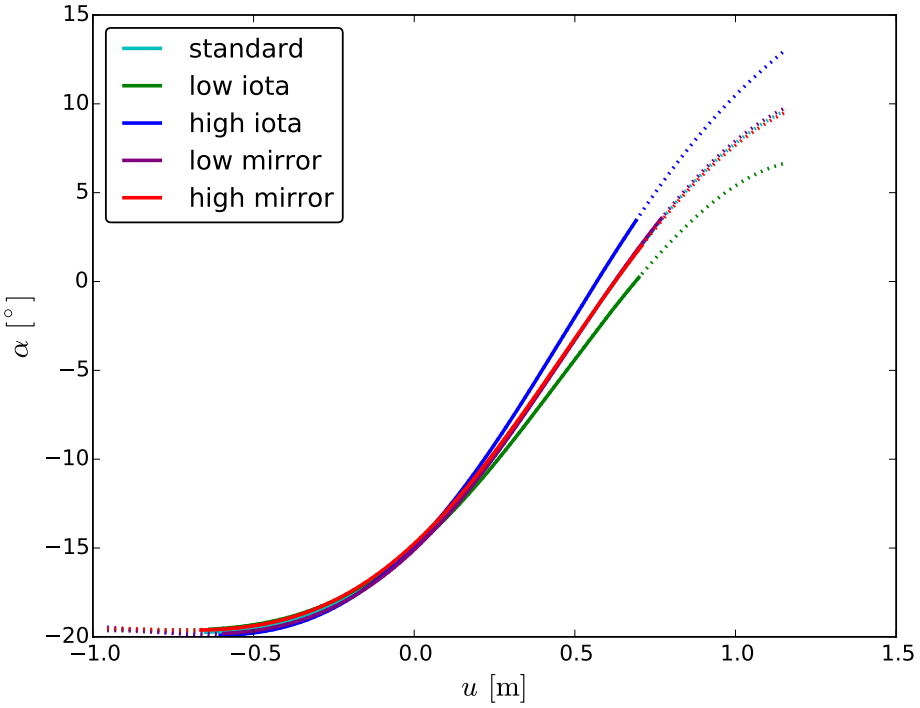

Figure 4.16: Variation α of the magnetic field angle in the transversal plane of the PCI beam along the beam chord from the AEZ-50 to the AET-50 port as function of the beam position u. The different colours represent different magnetic field configurations. The magnetic axis is at $u = 0\,\mathrm{m}$. The dotted areas are beyond the last closed flux surface.

with M being the effective magnification of the receiving side optics system. If the beam is not perfectly collimated its diameter at two different positions along the beam chord varies and so the effective magnification $M_1 \neq M$ and $M_2 \neq M$ for these two positions (in the case of perfect collimation it is $M = M_1 = M_2$). If the collimation error and the scattering position is not known the values for the M_i are unknown too. However, we can estimate theoretically the expected error. As measure for the error we define the relative length difference

$$\xi := \frac{d(l_2) - d(l_1)}{d(l_1)} = \frac{d(l_2)}{d(l_1)} - 1 \tag{4.18}$$

of two different beam diameters at position l_i along the optical axis e.g. the extreme case of a scattering volume at the last closed flux surface (LCFS) on the inboard and outboard side. We can parametrize the beam diameter

#	d_0 [mm]	d_3 [mm]	ξ [%]
1	40	80	4.3
2	30	90	6.4
3	20	30	2.6
4	20	40	4.3
5	50	60	1.2
6	100	110	0.6

Table 4.3: Values of ξ according to (4.20) as function of d_0 and d_3. The value $l_3 = 22\,\mathrm{m}$ is the optical path length between mirrors M1 and M6. The values of $l_1 = 10.9\,\mathrm{m}$ and $l_2 = 12.3\,\mathrm{m}$ correspond to a scattering volume at the LCFS on the inboard and outboard side, respectively.

$d(l)$ of a diverging geometrical beams as

$$d(l) = d_0 + \frac{l}{l_3}(d_3 - d_0) \tag{4.19}$$

for known beam diameter $d_i \coloneqq d(l_i)$ with $i = 0, 3$. Inserting in (4.18) yields

$$\xi = \frac{l_3 d_0 + l_2(d_3 - d_0)}{l_3 d_0 + l_1(d_3 - d_0)} - 1 \tag{4.20}$$

In Table 4.3 some values of ξ are shown as function of d_0 and d_3. The cases #1 and #2 are somehow extreme where the beam diameter on the transmitting side optics table is only a half (#1) or even a third (#2) of the diameter on the receiving side. We note, that for larger beams the absolute difference in diameter is less relevant (c.f. #2 and #6). This becomes also clear from (4.20): the terms $\propto (d_3 - d_0)$ become less important as d_0 increases. We note, that only in the extreme cases ξ exceeds the error $\Delta k_\alpha / k_\mathrm{m}$. In any practical case it should be well below 10%.

In reality a beam is never perfectly collimated due to its Gaussian beam profile. However, this effect is very small as we can see from the following considerations. The transversal beam profile of a Gaussian beam reads

$$d(l) = d_0 \sqrt{1 + \left(\frac{l}{l_R}\right)^2} \quad \text{with} \quad l_R = \frac{\pi d_o^2}{4\lambda_b} \tag{4.21}$$

where l is the distance from the beam waist where the beam has a diameter of d_0 ($1/e$ amplitude decrease or $1/e^2$ intensity decrease) and l_R is the Rayleigh

length. We find for ξ

$$\xi_g = \sqrt{1 + \left(\frac{l}{l_R}\right)^2}. \tag{4.22}$$

For ξ_g to be large $l_R \propto d_0^2$ has to be small. If we assume an unfavourable optics set up where the beam waist is located at one side of the plasma (instead of the center) the maximum distance to the beam waist for a scattering center is the plasma length of $l = 1.4\,\mathrm{m}$ and an unfavourable small beam diameter of $d_0 = 20\,\mathrm{mm}$ we find $\xi_g = 0.1\,\%$, thus much smaller than the above discussed effects.

Chapter 5

Study of Turbulence in the Wendelstein 7-X Stellarator

As discusses in Sec. 2.5 gradient driven turbulence in the ion scale is expected to play an important role in Wendelstein 7-X. In this chapter we analyse turbulence with focus on the PCI diagnostic on the example of a discharge for two different situations with modified gradients.

5.1 Discharge Overview

We consider the discharge shown in Fig. 5.1. The plasma is fuelled via gas puffing and heated by electron cyclotron resonance heating (ECRH). The magnetic field is set to be in standard configuration EJM with 2.52 T on axis. While the density is kept almost constant the ECRH power is reduced from approximately 5.0 MW down to approximately 2.5 MW in three steps. We expect thus to have modified temperature gradients within the same discharge which simplifies the comparison. For impurity studies a small amount of impurities is injected by the laser blow off (LBO) system. The injections can clearly be seen in the radiated power P_{rad} which peaks for each injection. However, in the following we are interested in the mean dynamic for the two different heating steps marked in Fig. 5.1. We average therefore all quantities over a time interval of 1 s. With this in mind, the perturbations caused by the LBO system takes place on a much shorter

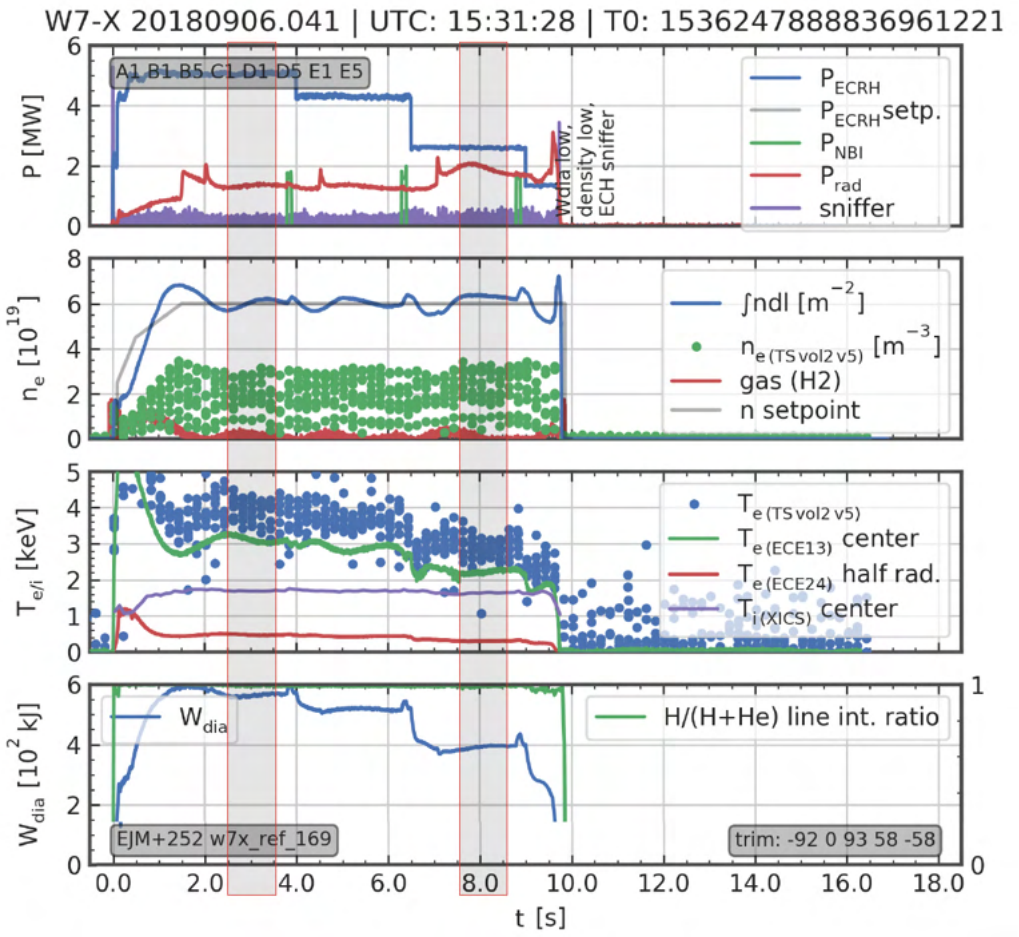

Figure 5.1: Overviewplot of the considered ECRH heated discharge. Courtesy A. von Stechow.

time scale and are outside of the considered time interval. Their influence is therefore considered to be negligible. For diagnostic purposes short blibs from the neutral beam injection (NBI) are added. These blibs can be recognised in the line integrated density signal, whereas the temperature is almost not affected. As for the LBO injections, the effect of the NBI blibs on the plasma is very limited and therefore negligible. Since the ECRH heats primarily the electrons we expect a direct correlation between injected heating power and electron temperature. Indeed we observe, that with reduced heating power the electron temperature decreases while the ion temperature is not much affected. Hence the drop in the plasma energy W_{dia} is mainly due to the drop in electron temperature. Note, that the temperatures shown in Fig. 5.1 are given only for a few locations and might not reflect possible changes in

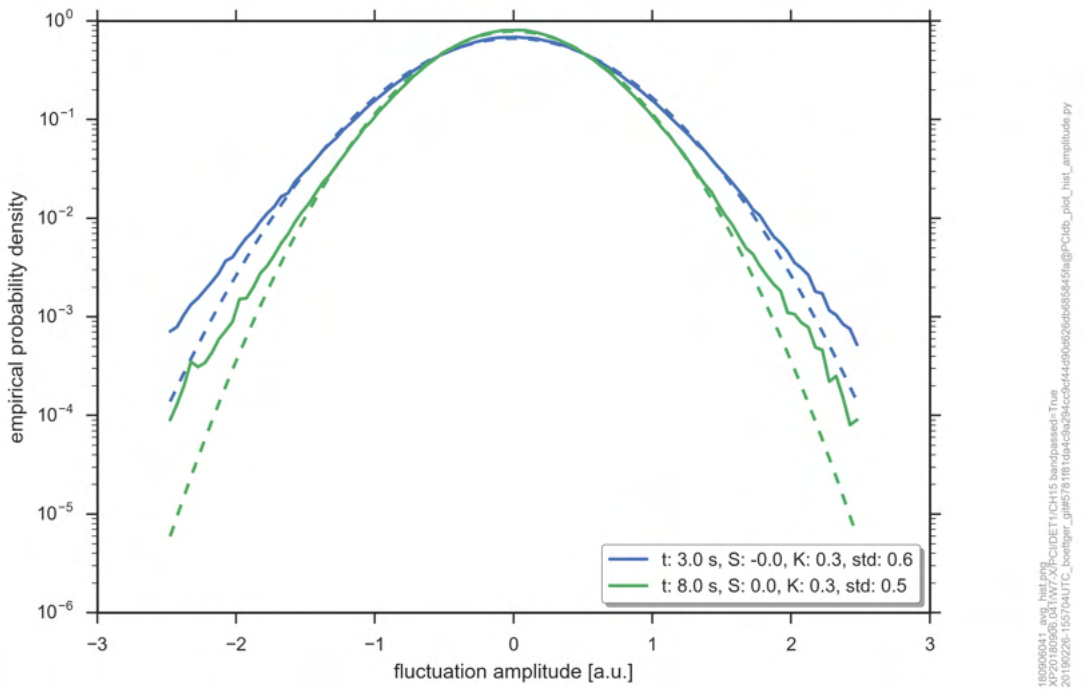

Figure 5.2: Histogram of one detector channel of the PCI diagnostic for the high ($t = 3\,\mathrm{s}$) and low ($t = 8\,\mathrm{s}$) ECR heating power step. The doted lines show a normal distribution with the same standard deviation as the data (solid lines).

the temperature gradients.

5.2 Statistical Analysis

According to the mixing length model in Sec. 2.2.5 turbulent eddies lead to density fluctuations in the presents of a density gradient. Furthermore, we have seen that these fluctuations can lead to transport through $E \times B$-advection. It is therefore from interest to study fluctuation amplitudes in more detail. Due to their stochastic nature a natural choice is an statistical approach in which we consider the distribution of the fluctuation amplitudes. For the two time intervals indicated in Fig. 5.1 at mean time 3 s and 8 s we center the raw signal of a certain channel to its mean value and normalize to the standard deviation. Furthermore a bandpass filter for frequencies between 20 kHz and 600 kHz is applied to mitigate effects from noise. Figure

5.2 shows the histogram of the fluctuation amplitudes for the two different ECR heating power levels. As reference, a normal distribution with zero mean and the same standard deviation as the data is shown. We observe a reduction of the standard deviation with reduced heating power. The distribution is symmetric in both cases which is quantified by the vanishing skewness S, a measure for the symmetry [120]. Furthermore we observe a systematic deviation of the distribution from the normal distribution with increased fluctuation amplitude. This deviation is small, as indicated by the small values of the excess kurtosis K. The excess kurtosis is a measure how the tails of a distribution compare to the normal distribution. Although small, the deviation from the normal distribution is statistical significant. To convince ourselves we can test on the normal distribution (e.g. with the Shapiro-Wilk or Jarque-Bera test) and find for the probability to find a normal distributed sample which is like the observed data or more extreme is less than $10^{-25} \approx 0$.

The reduction of the standard deviation with reduced heating power indicates a reduction of the fluctuation level as larger fluctuation amplitudes become less frequent. This is in agreement from what we expect if we assume that with reduced heating power the turbulent drive through temperature gradients becomes smaller which finally results in less fluctuations. Although small amplitude density fluctuations are nearly normal distributed, a significant deviation of large events is observed leading to a more bursty character of the fluctuations. This is in agreement with numerical simulations of ITG turbulence [121]. Considering the plasma as nearly incompressible, density fluctuations are generated by radial advection within a density gradient region. Due to the observed symmetry, we can conclude that the advection of higher plasma density and the associated local flattening of the density resulting in negative fluctuation amplitudes are well balanced.

5.3 Spectral Analysis

Figure 5.3 shows the spectrogram of the PCI signal for a single detector channel. More precisely, we divide the time series obtained from PCI measurements in chunks of 1 ms length and calculate for each one the spectrum. The time series of all spectra presents then the shown spectrogram for the fluctuation power. Generally, the spectrogram shows broadband fluctuations. The horizontal narrow banded lines are noise as well as the structures around

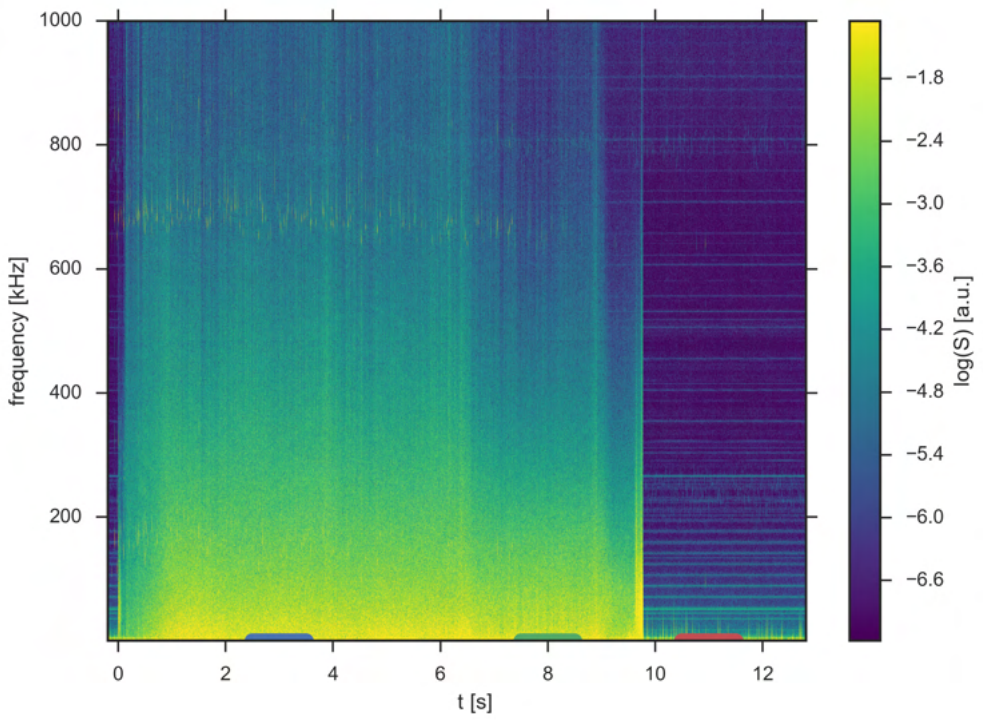

Figure 5.3: Spectrogram of one detector channel of the PCI diagnostic. The marked time intervals are analysed in more detail in Fig. 5.4.

700 kHz (both appear also if there is no plasma for $t < 0\,\mathrm{s}$). However, we can identify a reduction of the density fluctuation level with decreasing power (at ca. 4.0 s and ca. 6.5 s). For a more detailed analysis we take the time average of the spectrogram over a length of 1 s at the marked positions in Fig. 5.3. The first two intervals (in blue and green) mark the two heating steps whereas the third (red) is chosen to be at a time without plasma in order to quantify the noise level. The resulting spectrum is shown in Fig. 5.4 where the frequency and spectral power are given in logarithmic scale. The denoted time is the mean time of the averaged time interval e.g. 3 s indicates an average interval of $[2.5\,\mathrm{s}, 3.5\,\mathrm{s}]$. Above 600 kHz the noise level starts to become comparable to the signal. Thus, the peaks above 600 kHz can be attributed to the high noise/low signal level. The spectra for both time instances show a power-law behaviour $S \propto f^{-\alpha}$ as expected for turbulent fluctuations. Variation of the heating power, however, is only reflected in the higher frequency part ($> 200\,\mathrm{kHz}$) of the spectrum, whose spectral index α is significantly reduced for the low compared to the high heating power phase,

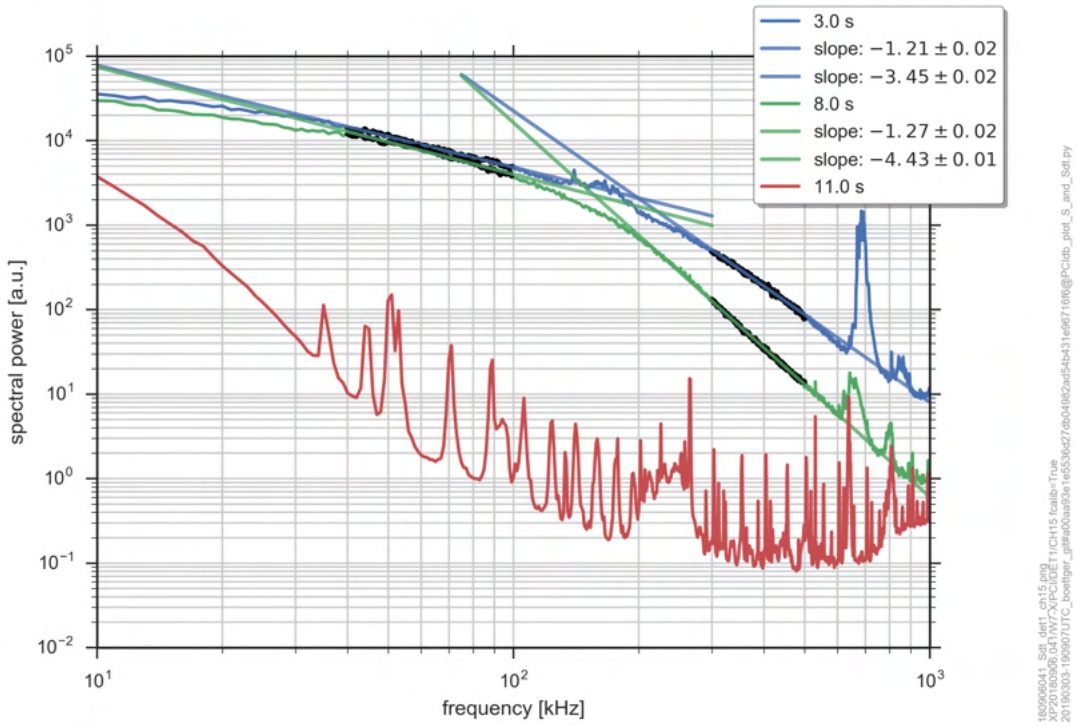

Figure 5.4: Spectral power of one detector channel. The respective time intervals are marked Fig. 5.3. The peaks above ca. 600 kHz cannot be trusted due to high noise level at these frequencies.

whereas the overall shape of the spectrum remains essentially unchanged. It must be noted that there is some not yet fully clarified variation of the spectral indices between channels. The given errors result from the linear fits on the dark coloured values and do not account for the aforementioned uncertainty. This must be taken into account for a quantitative comparison. However, the qualitative behaviour remains unchanged.

Furthermore, the analysis is done in the time domain and changes of the radial plasma profiles and the associated variation of the fluctuation phase velocities fold into this analysis. To get further insight into the fluctuation characteristics, the spatiotemporal capabilities of the diagnostics can reveal a wavenumber-resolved spectrum. This is shown in Fig. 5.5 for both heating steps. In addition to the temporal Fourier transform a spatial Fourier transform across all 32 channels was applied to the detector signal. The color in the main plot of Fig. 5.5 indicates the fluctuation power P_{kf} as function of

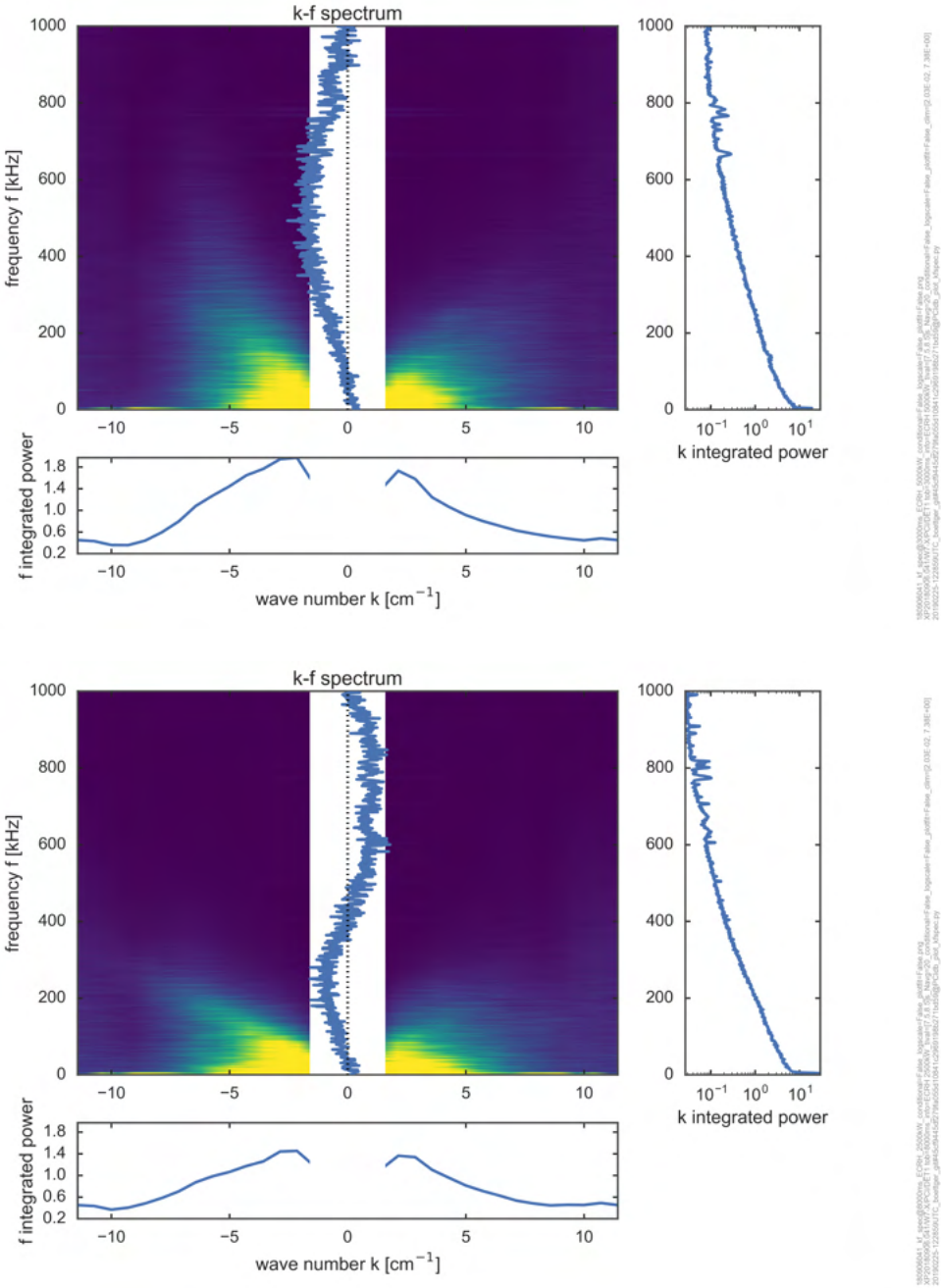

Figure 5.5: Wavenumber-frequency spectrum measured by the PCI diagnostic together with the power integrated over wavenumber and frequency, respectively. The top figure shows data obtained for the high ECR heating, the bottom figure for the low ECR heating case.

the wavenumber k and frequency f in linear scale. Positive wave numbers indicate a propagation direction parallel to the sound wave calibration source which is upwards or in positive z-direction (c.f. Fig. 4.1). This corresponds to a propagation on the low field side parallel to the poloidal direction and anti-parallel on the high field side. The graph on the right next to the main plot shows the power integrated over the wavenumbers. Similarly, the plot below shows the frequency-axis integrated power. The white area in the center of the main plot masks the lower k-limit due to the finite phase plate groove width as discussed in Sec. 4.5.1. Since the PCI signal is line integrated it picks up fluctuations on the inboard as well as on the outboard side. Thus, a fluctuation travelling around the plasma results in a dispersion relation with positive and negative phase velocity but the intensity might be different as e.g. the gradients can be different. From this perspective it might be fruitful to measure the symmetry of the observed power. This is done by the blue line drawn above the masked area, which indicates k_P defined as

$$k_P(f) \coloneqq \frac{\int k P_{kf}(f,k)\,\mathrm{d}k}{\int P_{kf}(f,k)\,\mathrm{d}k}\,. \tag{5.1}$$

We observe for both situations that most of the power is located at small wavenumbers and frequencies. The maximum wavenumber is symmetric at around $\pm 2.5\,\mathrm{cm}^{-1}$ resulting in $k_{\max}\rho_s \approx 0.3$, which is in the expected ion scale turbulence range. Note that the turbulent fluctuations are not of harmonic nature, thus we expect a broad banded (wavenumber) spectrum. The power is not symmetrically distributed for all frequencies. For the high power case a systematic deviation of k_P with increasing frequency towards negative wavenumbers is observed which inverts at about 500 kHz. This manifests also in the slightly increased frequency integrated power for negative wave numbers. For the low power case the inverse symmetry deviation is at about 250 kHz. Furthermore $k_P \approx 1\,\mathrm{cm}^{-1}$ between roughly 600 kHz and 900 kHz.

For both cases we can identify a correlation between wavenumber and frequency indicating a dispersion relation. As seen in the spectrum in Fig. 5.4 the fluctuations span over a wide range of power values. In order to reveal details in P_{kf} which might be not visible due to the finite colorbar resolution we normalise the value of P_{kf} for each frequency to its mean value averaged over all wavenumbers. The resulting normalised wavenumber-frequency spectrum $\tilde{P}_{kf}$ is shown in Fig. 5.6. The wavenumber-frequency correlation is much more pronounced compared to Fig. 5.5 and we can identify for negative wavenumbers a constant phase velocity up to approximately 200 kHz for both the low and high power case. For positive wavenumbers the relation between wave number and frequency seems linear as well, but the overall

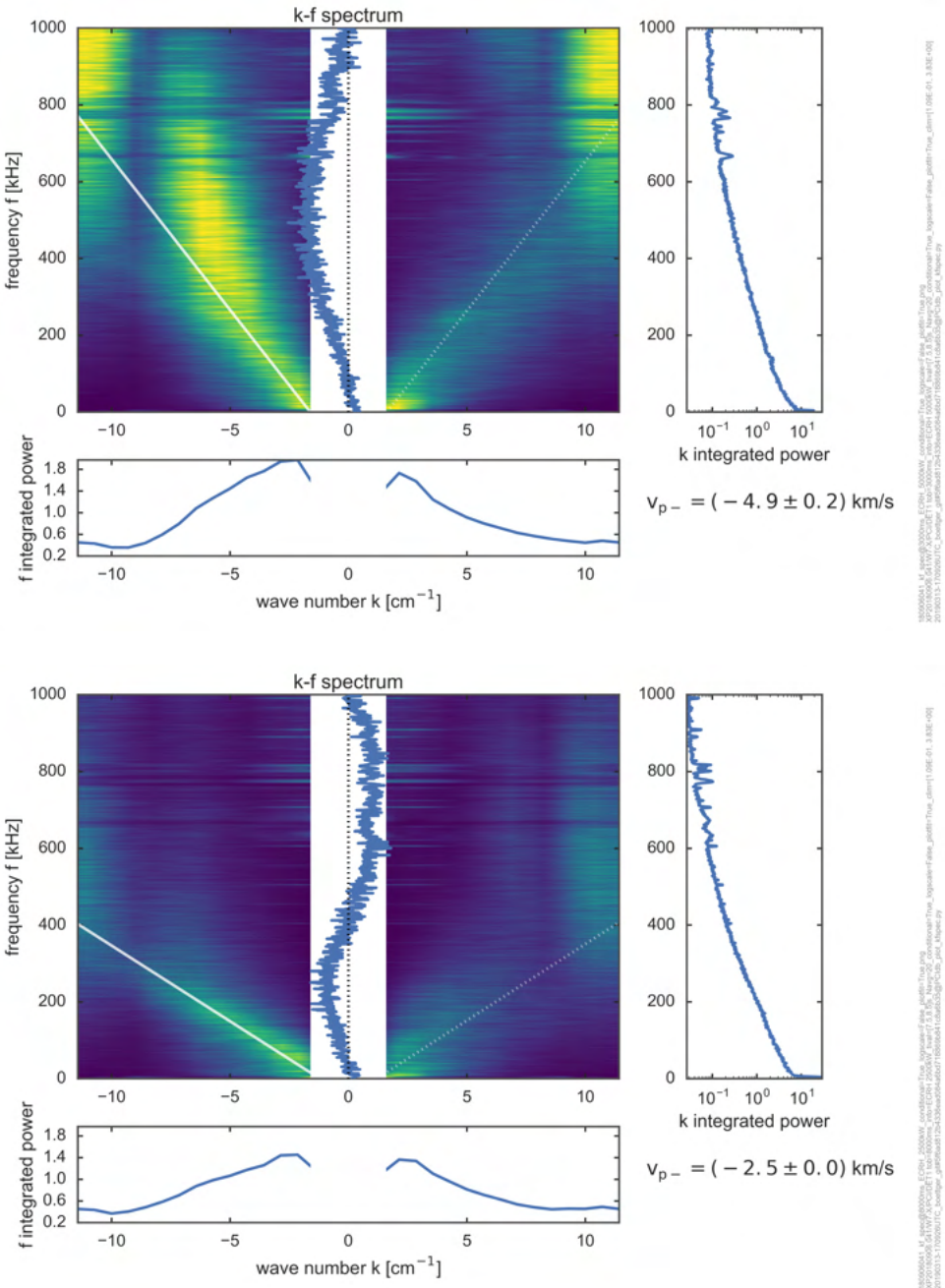

Figure 5.6: Normalised wavenumber-frequency spectrum measured by the PCI diagnostic. The top figure shows data obtained for the high ECR heating, the bottom figure for the low ECR heating case.

power is less. For frequencies above ca. 300 kHz vertical structures are visible and the negative k branch of the dispersion relation in the high power case becomes more curved. These vertical structures are artefacts of the PCI system. We can estimate the phase velocities of the fluctuations from the linear part below 300 kHz by fitting a linear dispersion relation

$$f(k) = \frac{1}{2\pi} v_{p\pm} k + f_0 \tag{5.2}$$

with $v_{p\pm}$ being the phase velocity. We have included here the non-physical constant f_0 in order to account for (unknown) systematic shifts which would otherwise bias the phase velocity estimate. The resulting linear curve as well as the estimated phase velocities for the negative wave number branches are show in Fig. 5.6. To compare for symmetry, the fitted branches are mirrored (dashed lines). The fits were done through the maxima of $\tilde{P}_{kf}$, thus the width of the branches were not taken into account. The given uncertainties are therefore only those obtained from the fit. As discuses in Sec. 4.5.2 the relative wavenumber error is about 10 % which we can take as estimate for the phase velocity uncertainty. However, as we can convince ourselves in Fig. 5.6 the fitted linear functions decently agree with the observed dispersion relation. The phase velocity roughly halves from the high ($v_{p-} = -4.9\,\mathrm{km/s}$) to the low ($v_{p-} = -2.5\,\mathrm{km/s}$) power case. Assuming an instability propagating around the plasma and contributing to the PCI signal on the inboard and outboard side we expect a symmetric spectrum. However, we observe less power ($k_P < 0$) and a slightly reduced phase velocity (at least in the high power case) in the positive wave number branch. These features might be related to the details of the magnetic geometry along the PCI line of sight. The spacing of the surfaces of constant magnetic flux on the outboard side is smaller when compared to the inboard side (c.f. Fig. 5.7). Taking the flux surfaces as surfaces of constant plasma pressure, this results in a larger plasma pressure gradient on the outboard side, thus a larger source of free energy for the observed fluctuations.

However, from a turbulence point of view a linear relation between wave number and frequency is not expected, as we have seen in Sec. 2.3 e.g. for the ITG dispersion relation (2.110). The observed constant phase velocity is rather a sign for a strong Doppler shift because of the rotating plasma. As discussed in Sec. 2.2.4 the ambipolarity condition for the neoclassical transport in a stellarator leads to a radial electric field causing an $E \times B$-rotation of the plasma. The Doppler shifted angular frequency ω_l in the

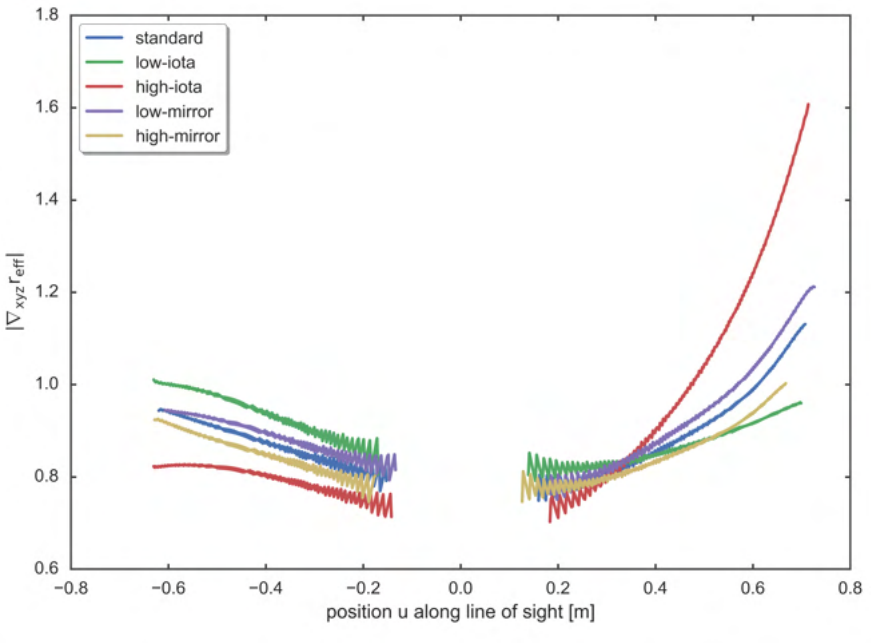

Figure 5.7: $|\nabla r_{\text{eff}}|$ as a measure for the flux surface density along the PCI line of sight for different magnetic field configurations. The oscillatory character is a numerical artefact.

laboratory frame reads

$$\omega_l(k) = \omega_r \left(1 + \frac{v_{E\times B}}{v(k)}\right) \tag{5.3}$$

with ω_r the angular frequency in the rotating frame, $v_{E\times B}$ the $E\times B$-velocity and $v(k)$ the phase velocity of the instability. The phase velocity is related to ω_l via $v(k) = \omega_r(k)/k$ hence we can write for ω_l

$$\omega_l(k) = k\left(v(k) + v_{E\times B}\right) . \tag{5.4}$$

Thus, in the case $|v(k)| \ll |v_{E\times B}|$ we find $\omega_l(k) \approx v_{E\times B}k$. We expect therefore the origin of the signals observed by the PCI to be strongly dominated by the $E\times B$-velocity. Figure 5.8 shows the radial $E\times B$-velocity profile for the considered situations. Positive values indicate a rotation counter-clockwise hence in positive poloidal direction. The dashed lines mark the observed phase velocities. Note that the sign of the measured phase velocities indicate the upwards/downwards direction whereas the sign of $v_{E\times B}$ defines the poloidal direction. They are note necessarily the same. For example, a fluctuation propagating in negative poloidal direction located on the inboard

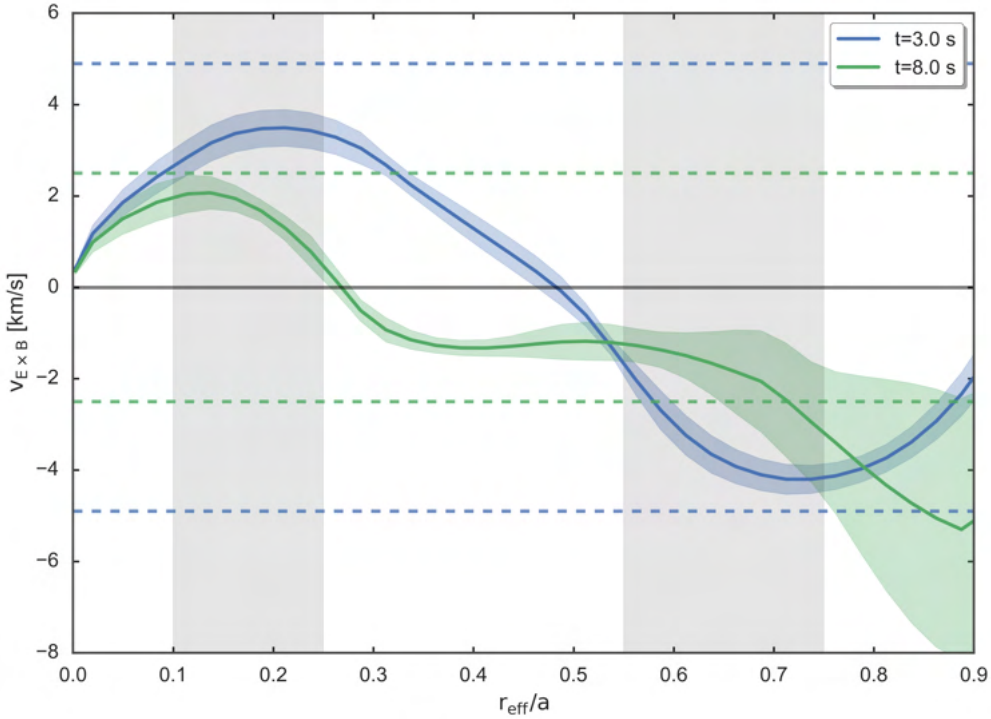

Figure 5.8: Radial velocity profile for the high ECRH case at 3 s and the low ECRH case at 8 s. Data: courtesy of [122].

side would appear as positive phase velocity in the PCI measurement. As we can see, the $E \times B$-velocity at $r_{\text{eff}}/a \approx 0.2$ and $r_{\text{eff}}/a \approx 0.6$ can explain to a large extent the observed variation, although not completely. However, the instability itself has a phase velocity v which is superimposed on $v_{E\times B}$, resulting in the measured signal $v_p = v + v_{E\times B}$. Since we observe $\omega \propto k$ we conclude from the above made considerations that $|v| \ll |v_{E\times B}|$ and the origin of the fluctuations must be therefore located close to the extrema in Fig. 5.8. Furthermore it is $|v_p| > |v_{E\times B}|$ for each power step. As a result v and $v_{E\times B}$ must have equal signs. This can be used to develop an expectation about the type of instability for each location, since the ion diamagnetic drift is parallel and the electron diamagnetic drift is anti parallel to the poloidal direction. Thus, an instability originating from the inner half at $r_{\text{eff}}/a \approx 0.2$ must propagate in the ion diamagnetic and an instability belonging to peaks in the outer half at $r_{\text{eff}}/a \approx 0.6$ in the electron diamagnetic drift direction. Considering the paradigmatic instabilities ITG, ITEM and TEM discussed in Chapter 2 we know that the ITG/ITEM modes propagate in the ion diamagnetic, while TEM modes propagate in the electron diamagnetic direction.

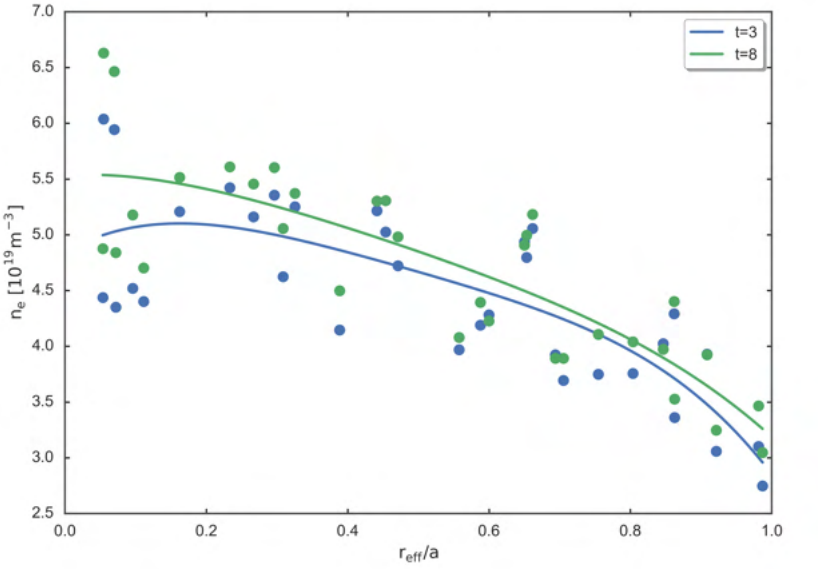

Figure 5.9: Density profile for the high ($t = 3\,\mathrm{s}$) and low ($t = 8\,\mathrm{s}$) power case. The dots represent measured values, the lines are spline interpolations. Data: courtesy of [123].

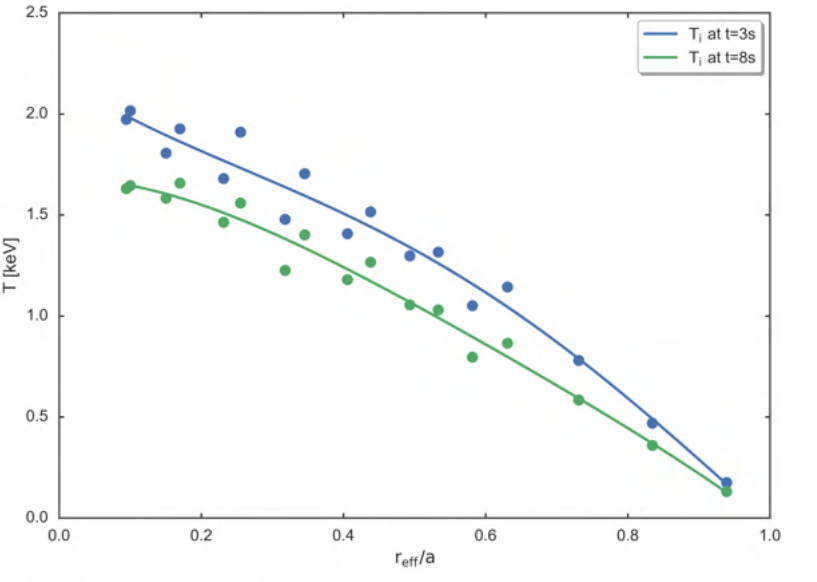

Figure 5.10: Ion temperature profile for the high ($t = 3\,\mathrm{s}$) and low ($t = 8\,\mathrm{s}$) power case. The dots represent measured values, the lines are spline interpolations. Data: courtesy of [123].

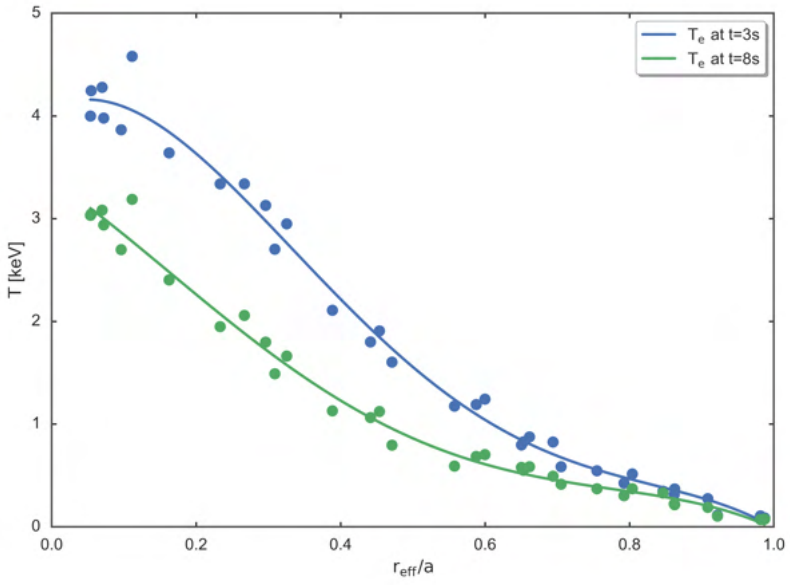

Figure 5.11: Electron temperature profile for the high ($t = 3\,\mathrm{s}$) and low ($t = 8\,\mathrm{s}$) power case. The dots represent measured values, the lines are spline interpolations. Data: courtesy of [123].

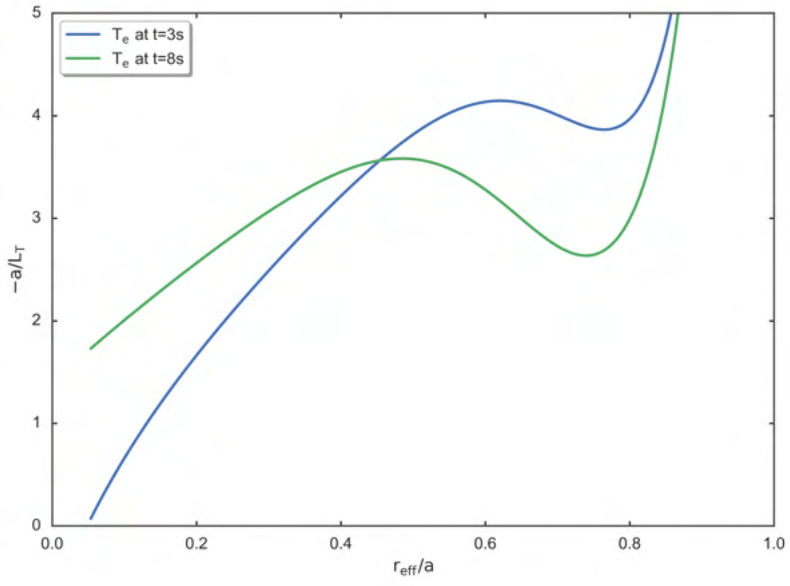

Figure 5.12: Inverse electron temperature gradient length for the high ($t = 3\,\mathrm{s}$) and low ($t = 8\,\mathrm{s}$) power case. Data: courtesy of [123].

From this we expect ITG/ITEM contributions from the inner half and TEM activity in the outer half. Further evidence can be found by considering the temperature and density profiles. The density profile (c.f. Fig. 5.9) shows only moderate changes between the heating steps, especially given the experimental uncertainty. The ion temperature profile shown in Fig. 5.10 reduces from about 2.0 keV to 1.6 keV in the core and is steeper in the edge region. In particular in the inner half where we would expect ITG/ITEM activity, the temperature gradient is small when compared to the edge. A significant difference between the heating steps is observed in the electron temperature profile which is expected since the ECRH heats primarily the electrons. For the low power case the temperature is reduced from approximately 4 keV down to approximately 3 keV in the core. The temperature profile exhibits a local maximum in the gradient at $r_{\text{eff}}/a \approx 0.6$ for the high power case and at $r_{\text{eff}}/a \approx 0.5$ for the low power case (c.f. Fig.5.12). This observation is in agreement with the expectation of TEM modes in the outer half, as they are destabilized by electron temperature gradients. Furthermore, the observed reduction in the fluctuation level could be attributed to a reduced TEM drive due to the smaller electron temperature gradient. Following the hypothesis that TEM modes cause the fluctuations measured by the PCI diagnostic, the strong signal observed for negative wave numbers originates from the outboard side. As mentioned above this is in agreement with the expectation of a stronger turbulent drive at this position due to the smaller flux surface spacing. A more quantitative discussion of the turbulent instabilities would involve numerical simulations. However, this is left for future investigations at this point.

Chapter 6

Summary and Conclusion

The advanced stellarator Wendelstein 7-X is the first fully neo-classical optimized device posing the question about the role of turbulence in optimized stellarators. Numerical simulations of turbulence in Wendelstein 7-X suggest the occurrence of microturbulence in the spatiotemporal range of ion scales such as the ITG and TEM instabilities. The phase contrast imaging (PCI) diagnostic allows for direct non-invasive measurements of line of sight integrated density fluctuations – where the plasma density presents the only plasma parameter determining the diagnostic response. It is the first diagnostic providing core density fluctuation measurements in optimized stellarator geometry. The specific situation at Wendelstein 7-X, in particular the cryostat, requires a diagnostic implementation with a more than 20 m long optical path. In contrast it is a crucial requirement to maintain alignment of the probe beam on the phase plate with sub-millimetre accuracy. Density fluctuations act as phase objects evading amplitude based detection mechanisms. However, the phase plate allows for conversion of the phase modulation into measurable amplitude variations. A comprehensive set of remotely steerable mirrors and cameras for beam diagnosis allow for corrections of alignment deviations during operation. Furthermore, a beam rotator ensures alignment of the one dimensional detector array with the predominately perpendicular to the magnetic field oriented fluctuations. The setup provides information on the poloidal scale length of fluctuations and, thus, allows for revealing the dispersion. The spatial scale length reference is given by a sound wave calibration system. The spanned wave number range of approximately $0.2 < k\rho_s < 1.5$ covers the range of the linear ITG and TEM spatial turbulence scales. In contrast to tokamaks, stellarators can exhibit

unfavourable curvature on the outboard and inboard side. In fact, most of the radial positions sampled by the PCI diagnostic, located close to the triangular plane, expose unfavourable magnetic curvature. Thus, ion scale turbulence under consideration is expected to be destabilized. However, flux surface compression on the outboard side when compared to the inboard side needs to be considered due to its effect on the thermodynamic quantities such as density and temperature. Here, the line integrated character of the measurement imposes a limitation on the interpretability of the data.

We discuss a paradigmatic electron cyclotron resonance heated discharge in Wendelstein 7-X. Due to the moderate density and the resulting weak electron-ion coupling we observe smaller ion temperatures when compared to electron temperatures. Radial density and temperature profiles are generally centrally peaked and role off towards the separatrix, but the shape remains essentially the same. In contrast, the radial $E \times B$-velocity profile shows significant differences. The spectral analysis reveals broadband fluctuations and a spectrum showing typical turbulent properties such as indications for self similar fluctuations resulting in a power law scaling of energy. The two found ranges exhibiting a power law scaling might be understood as signatures of a dominant two dimensional system, which we expect from the two dimensional $E \times B$-advection of the turbulent eddies.

The wavenumber-frequency spectrum reveals a dispersion of the fluctuations with constant phase velocity $v_p = \omega/k$, which indicates that the motion is mostly governed by the scale independent $E \times B$-Doppler shift in contrast to an expected dispersive contribution from an instability. Considering the radial $E \times B$-profile this finding suggests that the density fluctuations are restricted to small radial ranges. The deviations between the measured phase velocities and the $E \times B$-rotation can be attributed to instabilities propagating in the ion diamagnetic drift in the central core region whereas in the main gradient region the drift is in the electron diamagnetic direction. The central core region exhibits very shallow gradients from which a drive of ITG modes is not expected. In contrast, the outer region displays a significant electron temperature gradient being consistent with the expectation of TEM modes at this location. This interpretation is supported by the observed reduction of turbulent fluctuations with reduced heating power, which correlates with a reduction of the radial gradient of electron temperature while the density gradient stays almost unchanged. In summary PCI is indeed a valuable tool for ion scale turbulence measurements and the radial integration is not a sever drawback if profiles are taken into account. We cannot exclude that ITG modes play a role in different discharge scenarios which can be addressed

in further campaigns.

Appendices

Appendix A

Transmitting Side Components List

Table A.1: Transmitting side optics component list (c.f. Fig. 4.3).

nr.	type	description	comment
1	laser	CO_2 laser	Main laser.
2	shutter	shutter	Enables fast switching of IR laser.
3	fixed lens	optic: Thorlabs LA7270-G. FL=500	Adjust IR laser beam waist.
4	beam splitter	mount: Thorlabs LCP06/M, optic: Laser Research Optics L39200020-L3	Reduce laser power.
5	beam dump	Air cooled beam dump.	Dumps approx. 50 W.
6	laser	Secondary visible helper diode laser (635 nm).	Simplifies beam alignment up to beam combiner (19).
7	flippable mirror	flipper: Thorlabs MFF102/M, optic: Thorlabs PF1011-P01.	Flipper to combine the diode guiding laser (6) and the CO2 laser.
8	beam splitter	mount: Thorlabs KM200, optic: Laser Research Optics L39200020-L3.	Reduce and monitor power.
9	power meter	Thorlabs PM100USB with Thorlabs S314C power meter head.	Power meter receives up to 25 W.
10	fixed mirror	mount: Thorlabs KM200, optic: Thorlabs NB2-L01.	
11	fixed lens	optic: Thorlabs LA7228-G. FL=200 mm.	
12	movable lens	optic: Thorlabs LC7759-F. FL=-25.4 mm	
13	movable lens	optic: II-VI Infrared 892020. FL=190.5 mm	
14	telescope	CO2 telescope	
		...	

Table A.1 continued ...

nr.	type	description	comment
15	fixed mirror	mount: Thorlabs LCP06/M, optic: Thorlabs NB2-L01.	
16	steerable mirror	mount: Piezo motor mount, optic: Thorlabs NB2-L01	Steer IR beam together with (18)
17	fixed mirror	mount: Thorlabs LCP06/M, optic: Thorlabs NB2-L01.	
18	steerable mirror	mount: Piezo motor mount, optic: Thorlabs NB2-L01.	Steer IR beam together with (16)
19	beam combiner	mount: Thorlabs LCP06/M, optic: Laser Research Optics L19200020-B0	Beamcombiner, passing for CO2 laser, reflecting for HeNe laser.
20	flippable mirror	flipper: Thorlabs MFF101/M, mount: Thorlabs FMP2/M, optic: Thorlabs PF2011-P01.	Short throw flipper.
21	fixed mirror	mount: Thorlabs LCP06/M, optic: Thorlabs PF2011-P01.	
22	thermal plate	Thermal plate exposed to UV light.	Visualize CO2 laser for co-alignment.
23	camera	IP camera Digitus DN-16039	Observes thermal plate for co-alignment.
24	flippable mirror	flipper: Thorlabs MFF102/M, mount: Thorlabs FMP2/M, optic: Thorlabs PF2011-P01.	Long throw flipper.
25	fixed mirror	mount: Thorlabs LCP06/M, optic: Thorlabs PF2011-P01.	
26	fixed mirror	mount: Thorlabs LCP06/M, optic: Thorlabs PF2011-P01.	

...

Table A.1 continued ...

nr.	type	description	comment
27	steerable mirror	mount: Piezo motor mount, optic: Thorlabs NB2-L01.	Steers HeNe beam together with (47).
28	fixed mirror	mount: Thorlabs LCP60/M, optic: Thorlabs NB2-L01.	
29	OAP	F=9" OAP, mount: Thorlabs KS3, optic: Thorlabs MPD399-M01.	Make telescope with F=80" OAP with magnification 80/9.
30	camera	IP camera Digitus DN-16039	Observe beam position on small OAP (29)
31	fixed mirror	4" mirror, mount: Thorlabs KS4, optic: Thorlabs PF40-03-P01	Manually steerable.
32	OAP	F=80" OAP	
33	flippable screen	flipper: Thorlabs MFF102/M, screen: self-made	Increase reflectivity in plane of mirror (32).
34	camera	IP camera Digitus DN-16039	Observe beam position on mirror (32)
35	steerable mirror	piezo driven 9" plane mirror	
36	laser	HeNe laser, primary visible laser	
37	fixed lens	optic: Thorlabs LBF254-150-A	Make a pre-telescope with (40).
38	grey filter	grey filter	Reduces output power to $< 1\,\mathrm{mW}$.
39	fixed mirror	mount: Thorlabs KM200, optic: Thorlabs PF20-03-G01.	

...

Table A.1 continued ...

nr.	type	description	comment
40	fixed mirror	mount: Thorlabs KM200, optic: Thorlabs PF20-03-G01	
41	fixed lens	optic: Thorlabs LA1908-633	Make a pre-telescope with (36).
42	fixed mirror	mount: Thorlabs KM200, optic: Thorlabs PF20-03-G01	
43	fixed mirror	mount: Thorlabs KM200, optic: Thorlabs PF20-03-G01	
44	fixed lens	optic: Thorlabs LA1461-A. FL=250 mm	
45	movable lens	optic: Thorlabs LC1715-A. FL=-50 mm	
46	movable lens	optic: Thorlabs LA1301-A. FL=250 mm	
47	telescope	HeNe telescope	
48	steerable mirror	mount: Piezo motor mount, optic: Thorlabs PF20-03-G01.	Steers HeNe beam together with (27).
49	fixed mirror	mount: Thorlabs LCP06/M, optic: Thorlabs PF20-03-G01.	
50	flippable mirror	flipper: Thorlabs MFF102/M, mount: Thorlabs FMP2/M, optic: Thorlabs PF2011-P01.	Flipper to block the HeNe laser.
51	fixed mirror	mount: Thorlabs LCP06/M, optic: Thorlabs PF20-03-G01.	

Appendix B

Receiving Side Components List

Table B.1: Receiving side optics component list (c.f. Fig. 4.8).

nr.	type	description	comment
1	fixed mirror	9“ plane mirror	
2	camera	IP camera Digitus DN-16039	Observes sceen (3) in front of mirror (4).
3	flippable screen	flipper: Thorlabs MFF102/M, screen: self-made	
4	fixed mirror	9“ plane mirror	
5	camera	IP camera Digitus DN-16039	Observes screen (6) in front of OAP mirror (7).
6	flippable screen	flipper: Thorlabs MFF102/M, screen: self-made	
7	OAP mirror	FL=80”, 9“ OAP	Forms M=80/6 telescope with small OAP (17).
8	fixed mirror	4“ mirror, mount: Thorlabs KS4, optic: Thorlabs PF40-03-P01	Manually steerable.
9	camera	IP camera Digitus DN-16039	Observes phase plate (14).
10	beam rotator	self-made	
11	steerable mirror	Mount: glued on motor, Optic: Thorlabs PF1011-P01	Steers beam based on signal from quadrature detector (13).
12	beam splitter	Mount: Thorlabs FMP1/M, Optic: custom-made	1” Beamsplitter, specially designed to have 1% transmissivity for IR laser but full reflection for visible light.
13	detector	Quadrature detector for vibration compensation.	
		...	

Table A.1 continued ...

nr.	type	description	comment
14	phase plate	2" Phase plate, groove width 1.1 mm, Mount: Thorlabs KM200	
15	power meter	Thorlabs PM100USB with Thorlabs S314C power meter head.	
16	fixed mirror	Mount: Thorlabs FMP1/M, Optic: Thorlabs PF1011-P01	
17	OAP mirror	FL=6", small 90 degree gold OAP, Optic: MPD269-M01	Forms M=80/6 telescope with large OAP (8).
18	thermal plate	Thermal plate exposed to UV light.	
19	flippable mirror	Flipper: Thorlabs MFF102/M, Mount: Thorlabs FMP2/M, Optic: Thorlabs PF20-03-C01	Flipper to check co-alignment and beam shape. The location is roughly the 1st image plane created by the two OAPs.
20	camera	IP camera Digitus DN-16039	Observes thermal plate (18).
21	beam splitter	Mount: Thorlabs KM200, Optic: II-VI INSP 263, S/N 100-321205-1	50% Beamsplitter to separate the beam path for detector 1 and 2. Manually steerable.
22	fixed mirror	Mount: Thorlabs KM200, Optic: Thorlabs PF2011-P01	Manually steerable.
23x	fixed mirror	Mount: Thorlabs LCP06/M, Optic: Thorlabs PF2011-P01	
24x	steerable mirror	Mount: Piezo motor mount, Optic: Thorlabs PF2011-P01	

...

Table A.1 continued ...

nr.	type	description	comment
25x	fixed lens	FL=16”	Lens to create a 2nd focal plane for the spatial filter.
26x	camera	IP camera Digitus DN-16039	Observes spatial filter (27a).
27x	spatial filter	Rotation Stage: Newport URB100CC with Newport ESP301 controller, Mask: self-made	Rotating spatial filter.
28x	fixed mirror	Mount: Thorlabs LCP06/M, Optic: Thorlabs PF2011-P01	
29x	fixed mirror	Mount: Thorlabs LCP06/M, Optic: Thorlabs PF2011-P01	
30x	fixed lens	FL=16”	
31x	fixed mirror	Mount: Thorlabs LCP06/M, Optic: Thorlabs PF2011-P01	
32x	steerable mirror	Mount: Piezo motor mount, Optic: Thorlabs PF2011-P01	
33x	fixed lens	FL=5”, Diameter 2”, Mount: Thorlabs CXY2	
34x	movable lens	FL=8.75”, Diameter 2”, Mount: Thorlabs CXY2	
35x	movable lens	FL=16”, Diameter 2”, Mount: Thorlabs CXY2	
36a	detector	Infrared Systems Development MCT-16-32 detector	detector 1
36b	detector	Infrared Systems Development MCT-12-32 detector	detector 2
37	telescope	detector telescope	Adjust beam to detector size.

Bibliography

[1] J. Wesson and D. J. Campbell, *Tokamaks* (OUP Oxford, 2011).

[2] M. Kikuchi et al., *Fusion Physics* (International Atomic Energy Agency, Vienna, 2012), oCLC: 888126761.

[3] R. Aymar et al., *The ITER Design*, Plasma Physics and Controlled Fusion 44, 519 (2002).

[4] `https://www.iter.org`.

[5] M. Hirsch et al., *Major Results from the Stellarator Wendelstein 7-AS*, Plasma Physics and Controlled Fusion 50, 053001 (2008).

[6] T. S. Pedersen et al., *Confirmation of the Topology of the Wendelstein 7-X Magnetic Field to Better than 1:100,000*, Nature Communications 7, 13493 (2016).

[7] T. Klinger et al., *Towards assembly completion and preparation of experimental campaigns of Wendelstein 7-X in the perspective of a path to a stellarator fusion power plant*, Fusion Engineering and Design 88, 461 (2013).

[8] `https://commons.wikimedia.org/wiki/File:Laminar-turbulent_transition.jpg` (downloaded on 02.01.2019). License: Creative Commons Attribution-Share Alike 3.0 Unported `https://creativecommons.org/licenses/by-sa/3.0/deed.en`.

[9] O. Reynolds, *An experimental investigation of the circumstances which determine whether the motion of water shall be direct or sinuous, and of the law of resistance in parallel channels.*, Proceedings of the royal society of London 35, 84 (1883).

[10] A. J. Chorin and J. E. Marsden, *A mathematical introduction to fluid mechanics* (Springer, New York, 1993).

[11] T. Klinger, *(Plasma) Turbulence*, lecture notes, Max-Planck Institute for Plasma Physics/ University of Greifswald, Greifswald, Germany (2016).

[12] U. Stroth, *Plasmaphysik: Phänomene, Grundlagen und Anwendungen*, 2nd edition (Springer Spektrum, Berlin, 2018), oCLC: 1001288000.

[13] H. Pécseli, *Low Frequency Waves and Turbulence in Magnetized Laboratory Plasmas and in the Ionosphere* (IOP Publishing, 2016).

[14] U. Frisch and A. N. Kolmogorov, *Turbulence: The Legacy of A. N. Kolmogorov* (Cambridge University Press, 1995).

[15] A. N. Kolmogorov, *The Local Structure of Turbulence in Incompressible Viscous Fluid for Very Large Reynolds Numbers*, Dokl. Akad. Nauk SSSR 30, 299 (1941).

[16] A. N. Kolmogorov, *On Degeneration (Decay) of Isotropic Turbulence in an Incompressible Viscous Liquid*, Dokl. Akad. Nauk SSSR 31, 538 (1941).

[17] A. N. Kolmogorov, *Dissipation of Energy in Locally Isotropic Turbulence*, Dokl. Akad. Nauk SSSR 32, 16 (1941).

[18] A. N. Kolmogorov, *On the Logarithmic Normal Law of Particle Distribution during Breakup*, Dokl. Akad. Nauk SSSR 31, 99 (1941).

[19] L. F. Richardson, *Weather Prediction by Numerical Process* (Cambridge, University Press, 1922).

[20] H. L. Grant et al., *Turbulence Spectra from a Tidal Channel*, Journal of Fluid Mechanics 12, 241 (1962).

[21] J. Maurer et al., *Statistics of Turbulence between Two Counterrotating Disks in Low-Temperature Helium Gas*, Europhysics Letters (EPL) 26, 31 (1994).

[22] J. R. Chasnov, *Simulation of the Kolmogorov Inertial Subrange Using an Improved Subgrid Model*, Physics of Fluids A: Fluid Dynamics 3, 188 (1991).

[23] T. Gotoh et al., *Velocity Field Statistics in Homogeneous Steady Turbulence Obtained Using a High-Resolution Direct Numerical Simulation*, Physics of Fluids 14, 1065 (2002).

[24] Y. Kaneda et al., *Energy Dissipation Rate and Energy Spectrum in High Resolution Direct Numerical Simulations of Turbulence in a Periodic Box*, Physics of Fluids 15, L21 (2003).

[25] A. Yoshizawa et al., *Turbulence theories and modelling of fluids and plasmas*, Plasma Physics and Controlled Fusion 43, R1 (2001).

[26] R. H. Kraichnan, *Inertial Ranges in Two-Dimensional Turbulence*, The Physics of Fluids 10, 1417 (1967).

[27] A. Yoshizawa, *Nonequilibrium Effect of the Turbulent-Energy-Production Process on the Inertial-Range Energy Spectrum*, Physical Review E 49, 4065 (1994).

[28] U. Stroth et al., *Energy confinement scaling from the international stellarator database*, Nuclear Fusion 36, 1063 (1996).

[29] R. J. Goldston and P. H. Rutherford, *Introduction to Plasma Physics* (Institute of Physics Pub, Bristol, UK ; Philadelphia, 1995).

[30] U. Stroth, *Transport in Toroidal Plasmas*, in *Plasma Physics*, edited by P.-D. D. A. Dinklage et al., number 670 in Lecture Notes in Physics, 213–267 (Springer Berlin Heidelberg, 2005).

[31] H. Tennekes and J. L. Lumley, *A First Course in Turbulence* (The MIT Press, 1972).

[32] C. Brandt, *Active Control of Drift Wave Turbulence*, Ph.D. thesis, University of Greifswald (2009).

[33] A. Hasegawa and M. Wakatani, *Plasma Edge Turbulence*, Physical Review Letters 50, 682 (1983).

[34] A. Hasegawa and K. Mima, *Pseudo-three-dimensional turbulence in magnetized nonuniform plasma*, Physics of Fluids 21, 87 (1978).

[35] W. Horton and A. Hasegawa, *Quasi-two-dimensional Dynamics of Plasmas and Fluids*, Chaos: An Interdisciplinary Journal of Nonlinear Science 4, 227 (1994).

[36] A. Hasegawa et al., *Nonlinear Behavior and Turbulence Spectra of Drift Waves and Rossby Waves*, The Physics of Fluids 22, 2122 (1979).

[37] C. Connaughton et al., *Rossby and Drift Wave Turbulence and Zonal Flows: The Charney–Hasegawa–Mima Model and Its Extensions*, Physics Reports 604, 1 (2015).

[38] J. Weiland, *Stability and Transport in Magnetic Confinement Systems*, volume 71 of *Springer Series on Atomic, Optical, and Plasma Physics* (Springer New York, New York, NY, 2012).

[39] S. Brunner, *Waves and Instabilities in Inhomogeneous Plasmas*, lecture notes Ecole Polytechnique Fédérale de Lausanne (2014).

[40] L. I. Rudakov and R. Z. Sagdeev, *On the Instability of a Nonuniform Rarefied Plasma in a Strong Magnetic Field*, Soviet Physics Doklady (1961).

[41] T. Dannert and F. Jenko, *Gyrokinetic Simulation of Collisionless Trapped-Electron Mode Turbulence*, Physics of Plasmas 12, 072309 (2005).

[42] E. J. Doyle et al., *Chapter 2: Plasma Confinement and Transport*, Nuclear Fusion 47, S18 (2007).

[43] E. J. Doyle et al., *Progress towards Increased Understanding and Control of Internal Transport Barriers (ITBs) on DIII-D*, Technical Report IAEA-CSP–8/C, International Atomic Energy Agency (IAEA) (2000).

[44] J. Stober et al., *Effects of Triangularity on Confinement, Density Limit and Profile Stiffness of H-Modes on ASDEX Upgrade*, Plasma Physics and Controlled Fusion 42, A211 (2000).

[45] G. Tardini et al., *Comparison of Theory Based Transport Models with ASDEX Upgrade Data*, Nuclear Fusion 42, 258 (2002).

[46] D. R. Mikkelsen et al., *Stiff Temperature Profiles in JT-60U ELMy H-Mode Plasmas*, Nuclear Fusion 43, 30 (2002).

[47] W. Dorland and G. W. Hammett, *Gyrofluid Turbulence Models with Kinetic Effects*, Physics of Fluids B: Plasma Physics 5, 812 (1993).

[48] P. H. Diamond et al., *Zonal Flows in Plasma—a Review*, Plasma Physics and Controlled Fusion 47, R35 (2005).

[49] Z. Lin et al., *Turbulent Transport Reduction by Zonal Flows: Massively Parallel Simulations*, Science 281, 1835 (1998).

[50] G. W. Hammett et al., *Developments in the Gyrofluid Approach to Tokamak Turbulence Simulations*, Plasma Physics and Controlled Fusion 35, 973 (1993).

[51] R. E. Waltz et al., *Toroidal Gyro-Landau Fluid Model Turbulence Simulations in a Nonlinear Ballooning Mode Representation with Radial Modes*, Physics of Plasmas 1, 2229 (1994).

[52] A. M. Dimits et al., *Scalings of Ion-Temperature-Gradient-Driven Anomalous Transport in Tokamaks*, Physical Review Letters 77, 71 (1996).

[53] R. D. Sydora et al., *Fluctuation-Induced Heat Transport Results from a Large Global 3D Toroidal Particle Simulation Model*, Plasma Physics and Controlled Fusion 38, A281 (1996).

[54] M. A. Beer, *Gyrofluid Models of Turbulent Transport in Tokamaks*, PhD Thesis, Princeton University (1995).

[55] A. M. Dimits et al., *Comparisons and Physics Basis of Tokamak Transport Models and Turbulence Simulations*, Physics of Plasmas 7, 969 (2000).

[56] A. Fujisawa, *A Review of Zonal Flow Experiments*, Nuclear Fusion 49, 013001 (2008).

[57] F. Wagner et al., *Regime of Improved Confinement and High Beta in Neutral-Beam-Heated Divertor Discharges of the ASDEX Tokamak*, Physical Review Letters 49, 1408 (1982).

[58] A. E. Hubbard, *Physics and Scaling of the H-Mode Pedestal*, Plasma Physics and Controlled Fusion 42, A15 (2000).

[59] A. Team, *The H-Mode of ASDEX*, Nuclear Fusion 29, 1959 (1989).

[60] F. Wagner, *A Quarter-Century of H-Mode Studies*, Plasma Physics and Controlled Fusion 49, B1 (2007).

[61] R. C. Wolf, *Internal Transport Barriers in Tokamak Plasmas**, Plasma Physics and Controlled Fusion 45, R1 (2003).

[62] F. Jenko et al., *Electron Temperature Gradient Driven Turbulence*, Physics of Plasmas 7, 1904 (2000).

[63] W. Dorland et al., *Electron Temperature Gradient Turbulence*, Physical Review Letters 85, 5579 (2000).

[64] F. Jenko and W. Dorland, *Prediction of Significant Tokamak Turbulence at Electron Gyroradius Scales*, Physical Review Letters 89 (2002).

[65] J. H. E. Proll et al., *TEM Turbulence Optimisation in Stellarators*, Plasma Physics and Controlled Fusion 58, 014006 (2016).

[66] `https://www.genecode.org`.

[67] V. Kornilov et al., *Gyrokinetic Global Three-Dimensional Simulations of Linear Ion-Temperature-Gradient Modes in Wendelstein 7-X*, Physics of Plasmas 11, 3196 (2004).

[68] V. Kornilov et al., *Gyrokinetic Global Electrostatic Ion-Temperature-Gradient Modes in Finite β Equilibria of Wendelstein 7-X*, Nuclear Fusion 45, 238 (2005).

[69] A. Kendl, *Gyrokinetic Analysis of Microinstabilities in a Stellarator Reactor*, Plasma Physics and Controlled Fusion 43, 1559 (2001).

[70] T.-H. Watanabe et al., *Reduction of Turbulent Transport with Zonal Flows Enhanced in Helical Systems*, Physical Review Letters 100 (2008).

[71] P. Helander et al., *Stellarator and Tokamak Plasmas: A Comparison*, Plasma Physics and Controlled Fusion 54, 124009 (2012).

[72] P. Helander et al., *Collisionless Microinstabilities in Stellarators. I. Analytical Theory of Trapped-Particle Modes*, Physics of Plasmas 20, 122505 (2013).

[73] J. H. E. Proll et al., *Collisionless Microinstabilities in Stellarators. II. Numerical Simulations*, Physics of Plasmas 20, 122506 (2013).

[74] G. G. Plunk et al., *Collisionless Microinstabilities in Stellarators. III. The Ion-Temperature-Gradient Mode*, Physics of Plasmas 21, 032112 (2014).

[75] G. G. Plunk et al., *Collisionless Microinstabilities in Stellarators. Part 4. The Ion-Driven Trapped-Electron Mode*, Journal of Plasma Physics 83 (2017).

[76] P. Xanthopoulos et al., *Controlling Turbulence in Present and Future Stellarators*, Physical Review Letters 113 (2014).

[77] P. Helander et al., *Advances in Stellarator Gyrokinetics*, Nuclear Fusion 55, 053030 (2015).

[78] J. H. E. Proll et al., *Resilience of Quasi-Isodynamic Stellarators against Trapped-Particle Instabilities*, Physical Review Letters 108, 245002 (2012).

[79] J. Nührenberg, *Development of Quasi-Isodynamic Stellarators*, Plasma Physics and Controlled Fusion 52, 124003 (2010).

[80] J. R. Cary and S. G. Shasharina, *Omnigenity and Quasihelicity in Helical Plasma Confinement Systems*, Physics of Plasmas 4, 3323 (1997).

[81] L.-G. Böttger, *Phase Contrast Imaging Diagnostic for the Wendelstein 7-X Stellarator*, Master Thesis, Greifswald University, Greisfwald, Germany (2015).

[82] G. S. Settles, *Schlieren and Shadowgraph Techniques* (Springer, Berlin, Heidelberg, 2001).

[83] R. O. Wayne, *Light and Video Microscopy* (Academic Press, 2013).

[84] F. Zernike, *How I Discovered Phase Contrast*, Science 121, pp. 345 (1955).

[85] F. Zernike, *Phase contrast, a new method for the microscopic observation of transparent objects*, Physica 9, 686 (1942).

[86] U. Bonse and M. Hart, *An X-Ray Interferometer*, Applied Physics Letters 6, 155 (1965).

[87] H. M. Presby and D. Finkelstein, *Plasma Phasography*, Review of Scientific Instruments 38, 1563 (1967).

[88] H. Weisen, *The phase-contrast technique as an imaging diagnostic for plasma density fluctuations*, Infrared Physics 25, 543 (1985).

[89] H. Weisen et al., *Observation of long wavelength turbulence in the TCA Tokamak*, Plasma Physics and Controlled Fusion 28, 1161 (1986).

[90] H. Weisen, *Imaging methods for the observation of plasma density fluctuations*, Plasma Physics and Controlled Fusion 28, 1147 (1986).

[91] H. Weisen, *The phase contrast method as an imaging diagnostic for plasma density fluctuations (invited)*, Review of Scientific Instruments 59, 1544 (1988).

[92] H. Weisen et al., *Turbulent density fluctuations in the TCA Tokamak*, Plasma Physics and Controlled Fusion 30, 293 (1988).

[93] S. Coda et al., *A phase contrast interferometer on DIII-D*, Review of Scientific Instruments 63, 4974 (1992).

[94] S. Coda and M. Porkolab, *Edge fluctuation measurements by phase contrast imaging on DIII-D*, Review of Scientific Instruments 66, 454 (1995).

[95] K. Tanaka et al., *Applicability of Laser Phase Contrast Method for the Measurements of Electron Density Fluctuations in High-Temperature Plasmas*, Japanese Journal of Applied Physics 31, 2260 (1992).

[96] K. Tanaka et al., *Characteristics of Electron Density Fluctuations in Heliotron E Measured Using a Wide Beam Laser Phase Contrast Method*, Journal of the Physical Society of Japan 62, 3092 (1993).

[97] R. Chatterjee et al., *Phase contrast imaging system for TEXT-U*, Review of Scientific Instruments 66, 457 (1995).

[98] R. Chatterjee and G. A. Hallock, *First results from the phase contrast imaging system on TEXT-U*, Review of Scientific Instruments 68, 676 (1997).

[99] E. Lo et al., *Calibration and test of the tangential phase contrast imaging diagnostic on CDX-U*, Review of Scientific Instruments 68, 1206 (1997).

[100] A. Mazurenko et al., *New Results from the Phase Contrast Imaging on Alcator C-Mod*, in *American Physical Society, 41st Annual Meeting of the Division of Plasma Physics* (1999).

[101] A. Mazurenko, *Phase Contrast Imaging on the Alcator C-Mod Tokamak*, Ph.D. thesis, Massachusetts Institute of Technology (2001).

[102] K. Tanaka et al., *Phase contrast imaging interferometer for edge density fluctuation measurements on LHD*, Review of Scientific Instruments 74, 1633 (2003).

[103] I. H. Hutchinson, *Principles of plasma diagnostics*, 2nd edition (Cambridge University Press, New York, 2005).

[104] T. H. Stix and T. H. Stix, *Waves in plasmas* (American Institute of Physics, New York, 1992).

[105] C. V. Raman and N. S. N. Nathe, *The diffraction of light by high frequency sound waves: Part I.*, Proceedings of the Indian Academy of Sciences - Section A 2, 406 (1935).

[106] J. R. Dorris, *Phase Contrast Imaging Measurements and Modeling of Short Wavelength Turbulence in the DIII–D Tokamak*, Ph.D. thesis, Massachusetts Institute of Technology (2010).

[107] E. Hecht, *Optik*, 5th edition (Oldenbourg, München, 2009).

[108] G. E. Andrews et al., *Special Functions* (Cambridge University Press, 1999).

[109] E. Zeidler (editor), *Springer-Handbuch der Mathematik I* (Springer, Wiesbaden, 2013).

[110] M. Born et al., *Principles of Optics*, 7th edition (Cambridge University Press, 1999).

[111] C. V. Raman and N. S. N. Nathe, *The diffraction of light by high frequency sound waves: Part II.*, Proceedings of the Indian Academy of Sciences - Section A 2, 413 (1935).

[112] K. Matsuo et al., *Development of Laser Imaging Method for Measurements of Electron Density Fluctuations in Plasmas*, Japanese Journal of Applied Physics 30, 1102 (1991).

[113] L. Bergmann and C. Schaefer, *Lehrbuch der Experimentalphysik. Bd. 3.*, 10th edition (de Gruyter, Berlin, 2004).

[114] W. Klein and B. Cook, *Unified Approach to Ultrasonic Light Diffraction*, IEEE Transactions on Sonics and Ultrasonics 14, 123 (1967).

[115] M. G. Moharam and L. Young, *Criterion for Bragg and Raman-Nath diffraction regimes*, Applied Optics 17, 1757 (1978).

[116] C. V. Raman and N. N. Nath, *The diffraction of light by high frequency sound waves: Part III*, in *Proceedings of the Indian Academy of Sciences-Section A*, volume 3, 75–84 (Springer, 1936).

[117] C. V. Raman and N. S. Nagendra Nath, *The diffraction of light by high frequency sound waves. Part IV.*, in *Proceedings of the Indian Academy of Sciences, Section A*, volume 3, 119–125 (Indian Academy of Sciences, 1936).

[118] N. S. N. Nath, *The diffraction of light by high frequency sound waves: generalised theory. The asymmetry of the diffraction phenomena at oblique incidence*, Proceedings of the Indian Academy Of Science, Section A 4, 222 (1936).

[119] S. Coda, *An Experimental Study of Turbulence by Phase-Contrast Imaging in the DIII-D Tokamak*, Ph.D. thesis, Massachusetts Institute of Technology (1997).

[120] T. Haslwanter, *An Introduction to Statistics with Python*, Statistics and Computing (Springer International Publishing, Cham, 2016).

[121] J. Anderson and P. Xanthopoulos, *Signature of a Universal Statistical Description for Drift-Wave Plasma Turbulence*, Physics of Plasmas (1994-present) 17, 110702 (2010).

[122] XICS diagnostic team: N. Pablant, A. Langenberg, M. Beurskens, K. Ewert, A. Langenberg, P. Traverso, P. Valson.

[123] Thomson diagnostic team: E. A. Pasch, M. Beurskens, S. Bozhenkov, H. Damm, G. Fuchert, B. Hor, B. Kursinski, K. Lehmann, J. Meineke, P. Nelde, E. Scott.